A STUDY OF POLYIMIDE FILMS MODIFIED WITH GOLD

by

Dennis Gerard Madeleine

Dissertation submitted to the graduate faculty of
Virginia Polytechnic Institute and State University
in partial fulfillment
of the requirements for the degree of

Doctor of Philosophy

in

Chemistry

Approved:

L.T. Taylor, Co-chairman

T.C. Ward, Co-chairman

J.E. McGrath

G.L. Wilkes

H.W. Gibson

August, 1988

Blacksburg, Virginia

A STUDY OF POLYIMIDE FILMS MODIFIED WITH GOLD

by

Dennis Gerard Madeleine

(ABSTRACT)

Virginia Polytechnic Institute and State University laboratories have produced a wide variety of polyimide films which have been modified by the incorporation of metal compounds. These polymer/metal composites have potential use as coatings in aerospace applications where enhanced electrical conductivity and thermal stability are desirable. Generally, these materials are produced by heating a polyamic acid solution which contains a soluble metal salt. While the electrical and thermal properties of some of these films have been studied in great detail, little is known about the factors which control the ultimate distribution of metal in the polymer matrix. In this work, the segregation of components in polyimide modified with the gold salt, $HAuCl_4 \cdot H_2O$, is described.

Thermal treatment usually promoted three changes in the film: (1) conversion of an initially present polyamic acid to the thermally stable polyimide, (2) reduction of chloroauric acid to metallic gold and (3) redistribution of the metal into gold domains either in the bulk or at a surface of the film. The third event listed above has been termed metalization. Most of the gold modified polyimide

films exhibited bulk metalization as evidenced by the dispersion of very small gold particles through out the film. However, the gold aggregates which comprised the metalized surface layer possessed several different morphologies which indicated that a diffusion limited aggregation processes controlled the aggregate growth. The appearance of these aggregates was central to developing a model of phase separation in these metal modified films.

ACKNOWLEDGEMENTS

I would like to thank my research advisors and for there kindness, patience and support during my graduate career. They gave me enough of a free reign to pursue some of the more esoteric aspects of this research without allowing me to stray too far afield. The suggestions and guidance of the remainder of my committee, are also very much appreciated.

I am also very much indebted to the "sixth man" of my graduate committee, of Sandia National Laboratories, Albuquerque, NM. His collaboration and cooperation were essential in understanding the fractal aspects of this work. The financial support of the National Aeronautics and Space Adminstration, Langley Research Center, is also appreciated.

Helpful advice was also provided by of group, and of group.

The highly competent assistance and friendship of is also acknowledged.

One of the most important aspects of graduate school is the friends I made, who helped make the rough times easier and the good times possible. For this reason, I would like to especially thank

Lastly, I would like to thank my wife my combined advisor, assistant and friend; who pushed me along when I asked for it, calmed me down when I needed it, and has loved me through all of it.

DEDICATION

This dissertation is dedicated to my parents

for their love, support and encouragement.

TABLE OF CONTENTS

LIST OF FIGURES

TABLE CAPTIONS

CHAPTER 1

INTRODUCTION

The word "composite" in materials science can have several different meanings. A very general definition of this class of materials was offered by Javits, who defined composites as "...any material that is not a pure substance and contains more than one component" [1]. While this definition is essentially correct, it is not particularly useful, as it describes almost every industrial material in any physical state. A more useful definition was used by Piatti who described composites as having "at least two chemically distinct phases with well defined separation (sic) interfaces and have characteristic properties which are not found in the individual components" [2]. While this definition suffers a bit in the translation into English, it does contain an essential feature of composite materials; that is, the observance of new material properties not inherent in any of the substituents. Borrowing a term from the social sciences, composites could be called "gestalt" materials; that is, the properties of the "whole" are not equal to a sum of the parts.

Two classes of composite materials can be delineated, depending on the way in which the multi-component structure

is generated. The first class of composites is formed by the compounding or blending of components. The second class of structures is formed by the in-situ growth of a dispersed phase within a continuous matrix phase.

The compounded composites are usually comprised of a polymeric matrix and an inorganic filler. In the past, thermosets predominated as the matrix resins, but in recent years there has been a trend towards the use of thermoplastics, due to their processibility. The filler used depends on the ultimate properties desired. If cost is the "property" of consequence, then fillers such as clay or cellulose may be used. In this way, expensive resins can be "diluted" with a cheap filler with minimal loss of ultimate properties. On the other hand, reinforced plastics are compounded by the incorporation of carbon fibers, glass beads and other materials into the polymer matrix. These composites may exhibit enhanced stiffness, heat resistance, electrical and thermal conductivity, abrasion resistance, impact strength or lubricity [3].

The second class of composites has a phase grown "in-situ" as in the case of the solidification of an eutectic alloy. Under ordinary conditions, solidification of these materials produces a two phase structure with the dispersed phase being randomly oriented in the continuous phase. However, if heat is extracted in a preferred direction,

then the two phase system will exhibit orientation. In the case of metal alloys, the unidirectional solidification technique can greatly enhance the mechanical properties of the composite.

The polymer films modified with metals discussed in this work are similar in some respects to both types of composites. They resemble compounded composites in that the ultimate material consists of a metal "filler" in a polyimide matrix. However, the fabrication of these films more closely resembles the in-situ generated composites. In their initial state, the films are thought to be homogeneous, solid state solutions of a metal compound and polymer. Thermal decomposition of the metallic "dopant" promotes phase separation into metal and polymer domains.

The research effort described here examined the structure- property relationships of polyimide films which have been modified by the incorporation of metal containing compounds. Ideally, these materials would retain the strength, flexibility, and thermal stability of the polyimide while exhibiting the enhanced electrical conductivity and reflectivity characteristic of the metal. These films are commonly synthesized by thermal imidization of a polyamic acid solution which contains a soluble metal salt. Alternatively, the metal may be added to a solution of a soluble polyimide and heated by the same thermal

profile used during imidization. In some cases the resulting films have metal concentrated on the surface which may lead to enhanced conductivity and reflectivity. For instance, the incorporation of a palladium complex into a polyimide resulted in a metallic surface with a film surface conductivity increased ten orders of magnitude over that of an unmodified polyimide film [4]. Reflective films exhibiting metal-oxide surfaces were also prepared from copper [5] and tin [6] additives, which exhibited increased surface conductivity by five orders of magnitude. Other additives, such as gold [7] and silver [8] salts produced films with highly reflective surfaces, but no substantial increase in room-temperature conductivity was observed.

While the electrical and thermal properties of some of these materials have been studied in great detail, little is known about the factors which control the ultimate distribution of metal in the film. The bulk of this dissertation is concerned with the description of phase separation that occurs in polyimide films modified with chloroauric acid, $HAuCl_4 \cdot H_2O$. In Chapter 3, the modified films are characterized by X-ray photoelectron spectroscopy(XPS) and Fourier transform infrared spectroscopy (FTIR). Chapter 4 describes the nucleation and growth of gold domains on a film surface and relates this phenomenon to concurrent changes in the polymer

chemistry. In the last chapter the mechanism of phase separation is explored and compared to computer simulations of growth processes which have been reported in the recent literature. The goal of these investigations was to better understand the chemistry and physics which underlie phase separation in metal modified polyimide films.

CHAPTER 2

EXPERIMENTAL

2.1 Materials

2.1.1 Solvent

N-methyl pyrollidone (NMP) was dried over calcium hydride, vacuum distilled and stored under nitrogen prior to use.

2.1.2 Monomers

The various diamines and dianhydrides used in the synthesis of the model compounds and polyamic acids are shown in Figure 1. The aromatic diamine, 4,4'-bis(aminophenyl)ether, (ODA) was obtained from Aldrich Chemicals, recrystallized from an ethanol-water mixture and sublimed twice. Alternatively, zone refined ODA was used as received from Aldrich Chemicals. 4,4'-bis(aminophenyl) sulfide, (DDS) was generously supplied by Mitsui Toatsu Chemical and used as received. 5(6)-amino-1-(4'-aminophenyl)-1,3,3-trimethyl-indane (DAPI), was grudgingly made available to us by Ciba-Geigy and was used as received.

All of the polymers discussed were derived from the same dianhydride, BTDA, 3,3'4,4' -benzophenonetetracarboxylic dianhydride, which was obtained from Criskev Chemicals and used as received. Aniline was vacuum

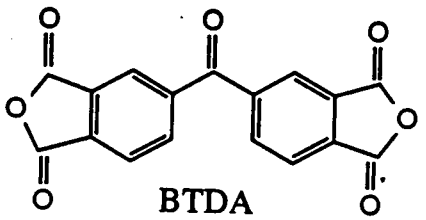

BTDA

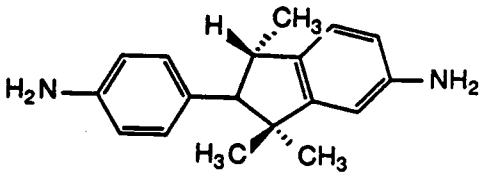

DAPI

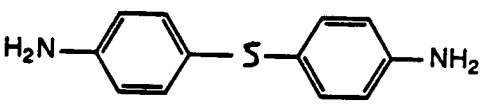

DDS

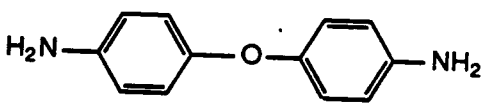

ODA

Figure 1. Dianhydride and diamines used in monomer synthesis.

distilled and phthalic anhydride was used as received from Aldrich Chemicals.

2.1.3 Dopant

Hydrogen tetrachloroaurate hydrate, $HAuCl_4 \cdot H_2O$, was obtained in high purity from Aldrich Chemicals and used as received.

2.1.4 XU 218

The soluble polyimide XU 218 was obtained from Ciba Geigy and heated 2 hours at 120° C under vacuum prior to use. The structure of this polymer is shown in Figure 2.

2.2 Model compound synthesis

Three model imide compounds (Figure 3) were prepared by the method of Dine-Hart and Wright [9]. Model compound I was prepared by refluxing 0.02 mol of aniline with 0.01 mol of BTDA, in 45 g of NMP for 2.5 h at 180°C. The precipitate was recrystallized from dimethylformamide (DMF). Model compound II was prepared by reacting 0.01 mol of ODA and 0.02 mol of phthalic anhydride in the same manner as model compound I. The product was recrystallized from a mixture of 25% DMF and 75% ethanol. Similarly, model compound III was formed by the reaction of 0.01 mol of DAPI, with 0.02 mol of phthalic anhydride. The product was precipitated in water, then recrystallized from a 10% water and 90% methanol mixture.

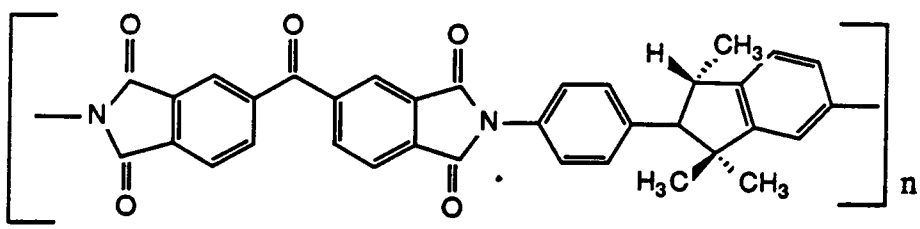

Figure 2. Ciba Geigy XU 218.

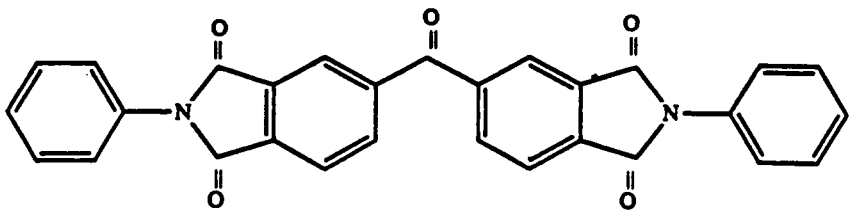

MC I

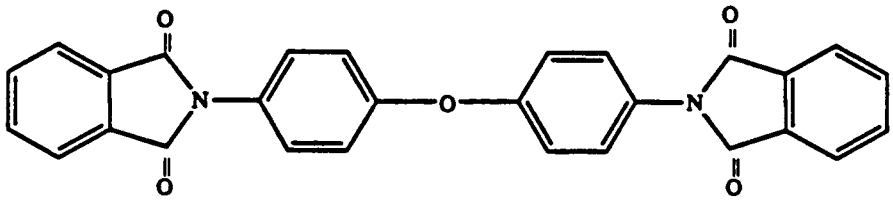

MC II

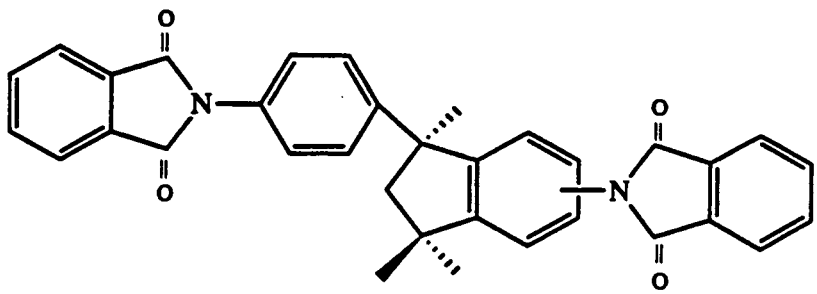

MC III

Figure 3. Model Imide Compounds.

2.3 Preparation of XU 218 solution

The dried XU 218 was added to the NMP (14.1% w/w) and stirred until the polymer dissolved, approximately two hours. The solution was stored at -20° C in a vacuum desiccator until used.

2.4 Preparation of the polyamic acid solutions

Solutions of the polyamic acids (14.1% w/w) were formed by reacting one of the three diamines in equimolar quantities with the dianhydride BTDA in NMP under a nitrogen atmosphere at room temperature. These solutions were usually prepared in 50 gram batches and stirred for twelve hours, subdivided, and stored in a vacuum desiccator at -20° C prior to thermal imidization.

2.5 Modification of the polymer solutions

The XU 218 polyimide and the polyamic acids were modified by adding $HAuCl_4 \cdot H_2O$ in the ratio of 0.5 millimole chloroauric acid to every millimole polymer repeat unit. Due to the hygroscopic and corrosive nature of the gold compound, the addition was carried out in a glove bag under a nitrogen atmosphere using a glass spatula.

2.6 Film preparation

Polymer solutions were spread onto either 15 cm. x 15

cm. untreated borosilicate glass plates or 2.5 cm. x 2.5 cm. glass microscope cover slides (Fisher) at a thickness of 0.61 mm. or 0.23 mm., respectively. Heating in an atmosphere-controlled oven (Blue-M) under nitrogen for 0.5 hour at 80°C and one hour at 100°C produced transparent films. The films cast on microscope slides were used in optical microscopy as described below. The larger films were heated an additional one hour at 200°C and one hour at 300°C. Unless otherwise noted, all films remained in contact with the glass casting plate throughout the thermal treatment. To produce solvent-free unmodified polyamic acid for thermogravimetric analysis (TGA) the material was precipitated in water according to a procedure outlined by Numata, Fujisaki and Kinjo [10].

2.7 Instrumentation

2.7.1 Thermal Analysis

A Polymer Labs dynamic mechanical thermal analyzer (DMTA) was used to obtain the thermo-mechanical results. The BTDA-ODA polyamic acid sample was mounted in the analyzer head using a single cantilever geometry. Thermal gravimetric analysis (TGA) of the films was obtained using a Perkin-Elmer TGS-2.

2.7.2 Microscopy

A Zeiss triocular microscope fitted with a 35 mm.

camera and Leitz 350 hot stage made it possible to visually record the metalization process as a function of time and temperature. The films cast on microscope cover slides and heat-treated at 100°C were inserted into the sample chamber of the hot stage and observed with transmitted light. A nitrogen purge was used to sweep the hot stage chamber and emulate the conditions used in the Blue-M oven. The changes which occurred in the samples at constant temperatures (160°C, 175°C, 200°C) were recorded as a function of time by microphotography.

Electron photomicrographs were obtained using a Phillips 420-T electron microscope, either in the SEM (scanning electron microscope) or STEM (scanning-transmission electron microscope) mode. Electron microscopy was performed by personnel in the Department of Materials Science and Engineering at Virginia Polytechnic Institute and State University. Cross sections were prepared by personnel in the Virginia-Maryland College of Veterinarian Medicine at Virginia Polytechnic Institute and State University, by embedding the films in an epoxy resin and sectioning the resulting block with an ultramicrotome. Cross sections were typically 80-100 nm thick.

2.7.3 X-ray techniques

XPS spectra were collected using a Perkin-Elmer Phi 530 x-ray photoelectron spectrometer under high vacuum (< 5

X 10^{-8} Torr). A magnesium anode operating at 250 W was used in the production of achromatic x-rays centered at 1253.6 eV. The model compounds were pressed onto indium foil prior to mounting on a piece of double-stick tape. No attempt was made to correct for charging by use of a flood gun, except as noted, and the binding energies cited have been referenced to the aromatic carbon signal at 285 eV. XPS data were acquired and stored by a Perkin-Elmer 7500 computer. Perkin-Elmer software was used in the curve fitting routine and calculation of the atomic concentration of elements present on the surface. The values reported for the binding energy and atomic concentration are accurate to within ± 0.2 eV and ± 0.5 atomic percent, respectively.

A Siemens small angle X-ray spectrometer with a Kratsky collimator was used. A rotating anode with a copper target and a nickel/graphite filter was used to produce monochromatic X-rays. The data were slit smeared and a hot stage sample holder was used to heat the sample during analysis. All SAXS data were obtained by personnel at Sandia National Laboratories, Sandia, New Mexico.

CHAPTER 3

CHARACTERIZATION OF POLYIMIDE FILMS MODIFIED WITH GOLD

3.1 Introduction

As a result of the interest by the microelectronics industry in the adhesion of metal to polymer surfaces, several articles have appeared in the literature which deal with the surface analysis of unmodified and metal-coated polyimide films. Leary and Campbell [11] observed the nonstoichiometric nature of polyimide surfaces and identified a "partially oxidized" carbon component in the x-ray photoelectron spectroscopy (XPS) spectra of polyimides. By the study of model compounds, Buchwalter and Baise [12] suggested that the "partially oxidized" carbon component arose from the phenyl ring carbons in the polyimide to which three or four carbonyl groups were attached. Calculation of core binding energies in model compounds by Silverman [13] confirmed these assignments. One important conclusion of these authors is that the binding energy of phenyl ring carbons in imides and polyimides depends on the number of carbonyl groups attached to the phenyl rings. The binding energy is increased over that of the unsubstituted ring by 0.5 eV for two carbonyl groups [13], 0.8 eV for three carbonyl groups

[14], and 1 eV for four carbonyl groups [12]. In addition, Ho and co-workers employed both XPS and ultraviolet photoelectron spectroscopy (UPS) to study the interaction of vapor deposited metals on polyimides and were able to identify specific interactions between the metal and organic substrate [15].

In the first section of this chapter, XPS was used to investigate the surface properties of model compounds, unmodified polyimide films and gold containing films prepared by the methods outlined in Chapter 2. The polyimides studied were the soluble polyimide Ciba-Geigy, XU 218, and the condensation polyimide BTDA-ODA.

While XPS is a powerful analytical technique in the characterization of polymers, it is limited to the study of surface chemistry. Information was also desired concerning the bulk properties of the film during thermal treatment; therefore, infrared spectroscopy was used to examine the effect of modification on the bulk composition of the polymer. This technique has been applied quite successfully to a study of the kinetics of imidization [16]. There are three peaks that can be used to follow the disappearance of the polyamic acid functionality during thermal treatment: the carbonyl stretch (coupled) at 1720 cm^{-1}, a peak at 1669 cm^{-1} and the imide stretching vibration at 1370 cm^{-1}. Alternatively, the formation of the imide structure can be

followed by the growth of the imide carbonyl stretch at 1780 cm^{-1} and 725 cm^{-1}. Both techniques provide greater insight to the nature of the modified films.

3.2 Results and Discussions

3.2.1 Model Compounds

Good agreement between the expected distribution of carbon, nitrogen, and oxygen as obtained via classical elemental analysis and the atomic concentration as determined by XPS was found for model compounds (Table 1). The atomic distributions shown in this table are based on carbon, nitrogen and oxygen only. The results indicate that the sensitivity factors used in the calculation of atomic concentrations are reasonable, and that the surface concentration of the imide models is similar to the expected bulk stoichiometry. The values obtained for model compound I are also comparable to values previously obtained by others for the same compound [12].

As mentioned previously, the C1s photoelectron spectra of imides and polyimides are quite complex owing to the difficulty in estimating the number of component peaks which comprise the spectrum. For instance, Silverman [14] calculated and fitted the C1s spectrum of model compound I to five peaks, not including the shake-up signal. Added to the difficulty of curve fitting are variables such as peak

Table 1. Atomic Concentration and Percent Carbonyl/ Aromatic Carbon Found in Model Compounds. Values in parentheses taken from Ref. 12.

	OXYGEN	NITROGEN	CARBON	CARBONYL	AROMATIC
MC-I					
Theoretical	13.9	5.6	80.6	17.2	82.8
Found-Elem. Anal.	15.3(16.0)	5.6(4.9)	79.1(79.2)	----	----
Found-XPS	13 (14)	6 (5)	81 (81)	13 (16)	87 (84)
MC-II					
Theoretical	14.3	5.7	80.0	14.3	85.7
Found-Elem.Anal.	14.5	5.6	80.0	----	----
Found-XPS	16	6	78	11	89
MC-III					
Theoretical	10.0	5.0	85.0	12.5	87.5
Found-Elem.Anal.	9.8	5.0	85.2	----	----
Found-XPS	10	5	85	9	91

position, intensity, width, and shape (degree of Gaussian versus Lorentzian). Due to the subjective manner of curve fitting, the C1s spectra in this report were fitted to only two peaks (Figure 4) centered at the following energies: 288.8 eV for the carbonyl carbons and 285.5 eV for the remaining carbons. The peak centered at 292.2 eV is due to the carbon shake up. Table 1 lists the percentage of carbonyl and aromatic carbon signal expected and found for the three model compounds. It should be noted that in all cases, the amount of carbonyl found is less and consequently, the amount of aromatic is more than expected, as discussed in the next section.

3.2.2 Unmodified Films

Table 2 lists the elemental distribution of carbon, nitrogen, and oxygen as determined by XPS for unmodified polyimide films. It was found that the concentration of these elements is invariant as a function of take-off angle (TOA), which suggests that the polyimides investigated are elementally homogeneous within the sampling depth of XPS. However, the observed distribution of these elements was not always the same as the expected (theoretical) distribution. For example, it was found that the surface concentration of oxygen in the BTDA-ODA film was greater than the amount anticipated based on polymer stoichiometry.

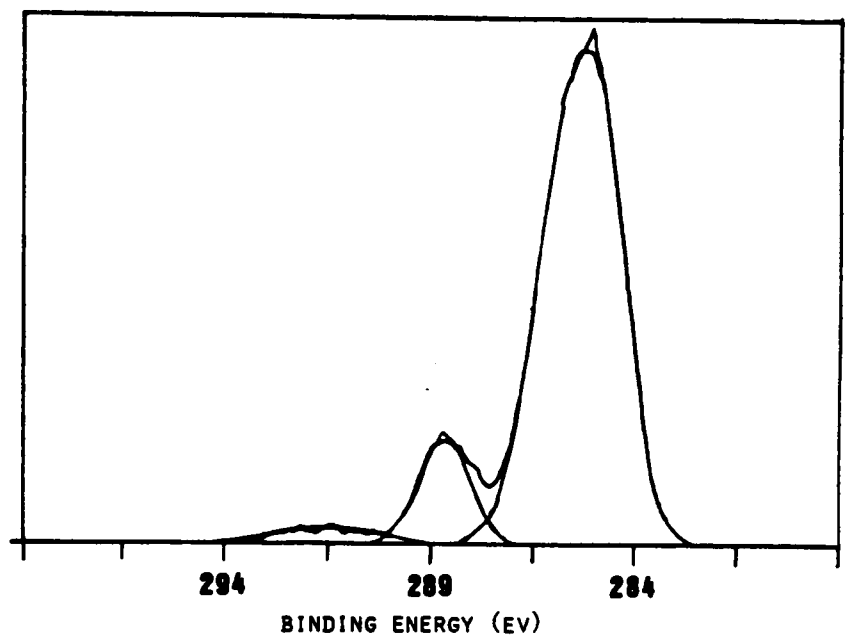

Figure 4. C1s XPS spectrum typical of XU 218 and air-side surface of BTDA-ODA.

Table 2. Atomic Concentration and Percent Carbonyl/ Aromatic Carbon Found in Unmodified Films.

	Oxygen	Nitrogen	Carbon	Carbonyl	Aromatic
BTDA-ODA					
Theor.	16.2	5.4	78	17.2	82.8
TOA = 15°	21	4	75	7	93
= 30°	20	4	75	8	92
= 90°	20	5	74	7	92
XU 218/					
Theor.	11.9	4.8	83.3	14.3	85.7
TOA = 15°	14	4	83	6	94
= 30°	14	4	84	4	96
= 90°	14	4	83	3	97

The surface enrichment of oxygen in the cured BTDA-ODA film could arise by several different mechanisms. First, it is possible that not all of the amic acid moieties in the polymer were converted to imide during thermal curing, or that imide groups originally formed were hydrolyzed to amide and acid functionalities. It is also possible that water, adsorbed on the surface, is responsible for the excess oxygen content. However, the increased oxygen concentration was only observed in the BTDA-ODA film and not the XU 218 film. The commercial thermoplastic polyimide is quite probably end capped with phthalic anhydride or a similar monofunctional unit, which would not enrich the surface in oxygen groups. As was the case with the model compounds, the C1s photoelectron spectra of the two unmodified polyimides were curved fitted and the areas corresponding to the carbonyl and the aromatic region were determined (Table 2). The experimentally determined carbonyl carbon percentage for each film is much lower than the expected value. Similar but less dramatic results were observed with the model compounds (Table 1). The observation and extent of the reduced carbonyl signal is consistent with the investigation of commercially available and laboratory synthesized BTDA-ODA by Leary and Campbell [11]. They concluded that side reactions, polymer fragments, trapped solvent, and paracrystalline formation

could all be responsible for the carbonyl nonstoichiometry observed at the polymer surface.

3.2.3 Modified XU 218

Incorporation of the metal additive into XU 218, resulted in an opaque film that was dark brown after the full thermal treatment. Both surfaces of the film appeared similar and did not possess a metallic luster when prepared by the method outlined in Chapter 2. However, earlier preparations of this film yielded metallic glass side surfaces. These differences were undoubtedly due to some change in the processing conditions (such as solvent, type of oven used, treatment of casting surface, cure atmosphere, etc.) which currently cannot be reproduced. In any case, all of the films discussed in this work were synthesized under the carefully controlled conditions outlined in Chapter 2. As a result, reproducible quality was maintained.

XPS results for the air and glass side surfaces of the modified XU 218 films are listed in Table 3. As was the case for the unmodified films, the elemental distribution of polymer elements is homogeneous within the sampling depth of XPS. The gold also appears to be distributed homogeneously, as indicated by the invariance of the gold signal as a function of TOA. A surprising feature of these

Table 3. Atomic Concentration and Percent Carbonyl/ Aromatic for the Air and Glass (in Parentheses) Surfaces of XU 218.

	GOLD	OXYGEN	NITROGEN	CARBON	CARBONYL	AROMATIC
XU 218/AU						
Theoretical	----	11.9	4.9	83.3	14.3	85.7
TOA= 15°	<.1(<.1)	13 (14)	4 (4)	83 (82)	6 (4)	94 (96)
TOA= 30°	<.1(<.1)	12 (13)	4 (4)	84 (83)	4 (4)	96 (96)
TOA= 90°	<.1(<.1)	12 (12)	4 (4)	84 (84)	3 (3)	97 (97)

results is that gold was detected in very small quantities (<0.1%). If all the gold was distributed uniformly throughout the film, then an atomic concentration of 1.2% gold would be expected. This suggests that the surface of the film (ca. 60Å) is enriched with polymer.

A C1s spectrum typical of both the air and glass side surface of a modified XU 218 film is quite similar to the spectrum shown in Figure 4. Figure 5 shows the gold $4f_{5/2,7/2}$ photopeaks at 88.7 and 85.1 eV. The value typically reported for the $4f_{7/2}$ metallic gold photopeak is 83.8 eV [17]. These results indicate that the gold on the air side is shifted 1.3 eV to higher binding energy. If gold exists as the uncombined metal, the question of why the gold photopeak is shifted becomes pertinent.

As will be shown in the next chapter gold is dispersed into very small domains within the polymer matrix of the XU 218 film. The discontinuity of the surface gold particles within the insulative polyimide matrix provides no mechanism for charge neutralization during the XPS experiment. Hence, the metallic gold particles charge and give rise to a higher binding energy than the value expected for elemental gold. Consequently, the shift in the gold photopeaks is probably due to a physical effect and not a chemical effect.

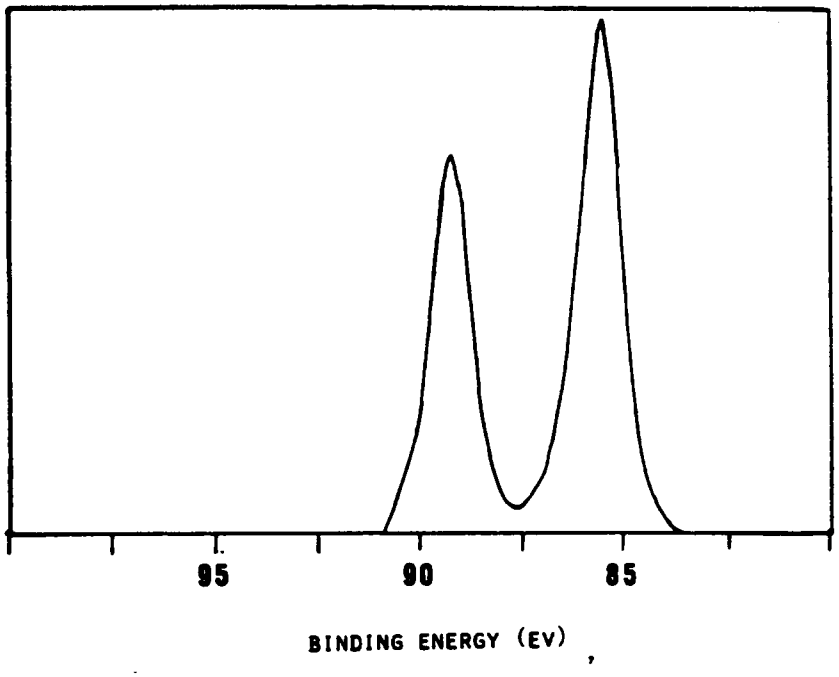

Figure 5. Au4f$_{5/2,7/2}$ XPS spectrum for air-side surface of XU 218.

3.2.4. Modified BTDA-ODA

In contrast to XU 218, the fully cured BTDA-ODA film is anisotropic in appearance. The air side surface looks much like the surfaces of the XU 218 film; however, the glass side surface is a bronze gold color and appeared to be a continuous layer of metal. As will be shown in the next chapter, the metallic glass side surface layer is actually comprised of gold aggregates ca. 30-100μm in diameter.

While the amount of gold detected on both surfaces was small, it increased with increasing depth, as shown in Table 4. This observation suggests that the outermost surfaces are virtually all polyimide which decreases in concentration as sampling depth increases. This effect was not observed on the surfaces of the modified XU 218 film, where a homogeneous distribution of gold throughout the XPS sampling depth was seen. Taken together these data suggest that the surfaces of both films are comprised almost totally of polyimide. Therefore, the gold metallic layer characteristic of the glass side surface of a modified BTDA-ODA film lies just beneath a very thin polyimide overlayer.

The typical C1s spectrum of the glass side surface of the BTDA-ODA film is shown in Figure 6, which is much different than the spectrum characteristic of the air side surface (Figure 4). Due to difficulties in sample

Table 4. Atomic Concentration and Percent Carbonyl/ Aromatic Carbon for the Air-Side Surface of BTDA-ODA.

	GOLD	OXYGEN	NITROGEN	CARBON	CARBONYL	AROMATIC
BTDA-ODA/Au						
Theoretical	---	16.2	5.4	78	---	---
TOA = 15°	0.2 (0.2)	21	4	75	7	93
= 30°	0.4 (0.5)	20	4	75	8	92
= 90°	1.0 (1.5)	20	5	74	7	92

Due to sample charging, only the gold signal from the glass-side surface (in parentheses) could be quantified.

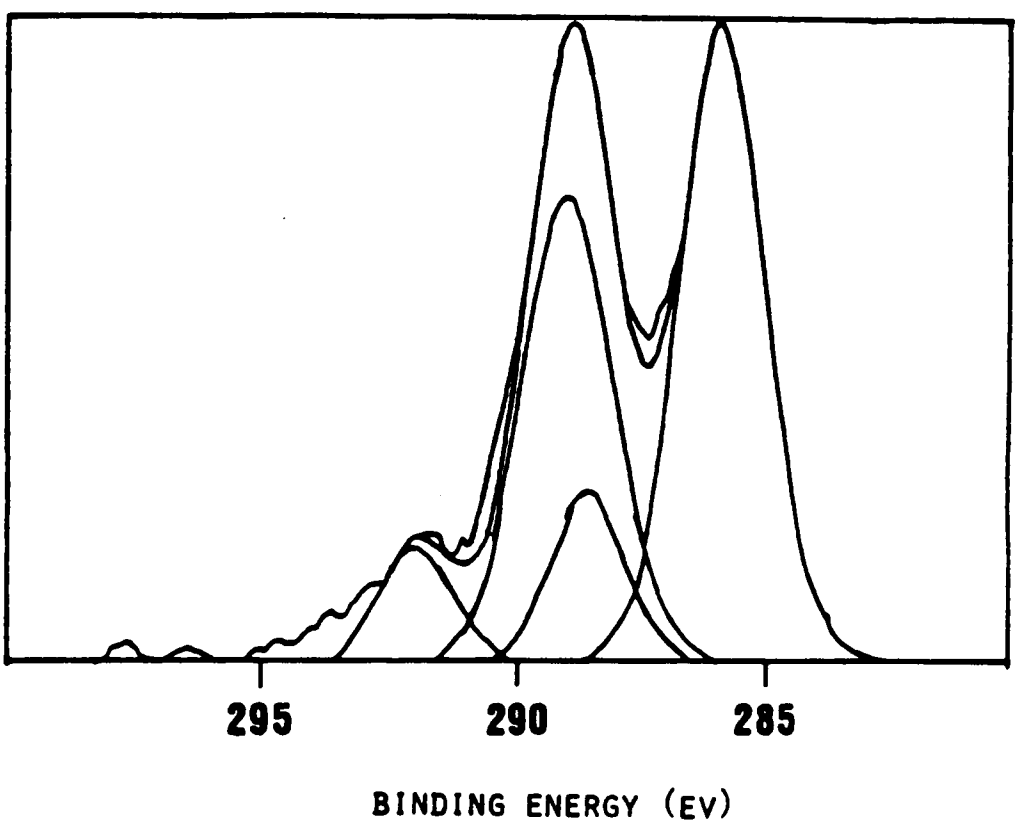

Figure 6. C1s XPS spectrum of glass-side surface of BTDA-ODA.

charging, discussed below, the polymer elemental concentration on the glass side surface could not be accurately quantified. The glass side C1s spectrum was pairwise fitted into two distinct polyimide signals(i.e., carbonyl and aromatic carbon). The difference in binding energy(within a set) between the carbonyl and aromatic photopeaks is the same binding energy difference observed in unmodified films. The two sets of C1s photopeaks are believed to be due to differential polyimide charging. A double set of peaks was also observed in the nitrogen and oxygen XPS signals. It is interesting to note, however, that only one set of $4f_{5/2,7/2}$ photopeaks was seen for gold on the glass side surface.

These distorted XPS spectra were investigated further and provided additional information concerning the glass side surface structure of the BTDA-ODA film. The double photopeaks associated with the polymer may be a result of the process by which the large gold particles formed and grew on the glass side surface of the film during thermal cure. This growth process is discussed in detail in the next two chapters. It is thought that the gold salt is homogeneously distributed throughout the bulk of the film prior to high-temperature(>200°C) thermal treatment. During the 200°C isotherm the dispersed metal diffuses to nucleation sites on the glass side surface of the film.

Migration of metal to these growing centers results in zones of metal depletion around the large surface aggregates. Indeed, these depletion zones can be seen as halos around the large particles when the film is observed with transmitted light optical microscopy. Therefore, two distinct regions of the polymer matrix are formed; the depletion zones and the regions which still contain metal dispersed in the polymer matrix. A schematic diagram of these films is show in Figure 7. It is believed that these two regions give rise to the double set of photopeaks observed in the photoelectron spectra of the polymer glass side surface. The lower binding energy photopeaks may result from photoelectrons ejected from the depletion zones. The higher binding energy photopeaks arise from the polymer matrix which still has gold dispersed in it. Upon x-ray excitation, the dispersed metal assumes a positive charge relative to the surrounding polymer matrix. The net effect of this dispersed positive charge is to retard the escape of photoelectrons from this region, which manifests itself as a second photoelectron peak at higher binding energy. Therefore, the double set of photopeaks associated with the polymer on the glass side surface of the film is a result of segregation of the metal into zones which contain distinctly different amounts of metal. The air side surface of BTDA-ODA and both surfaces of XU 218 contain no

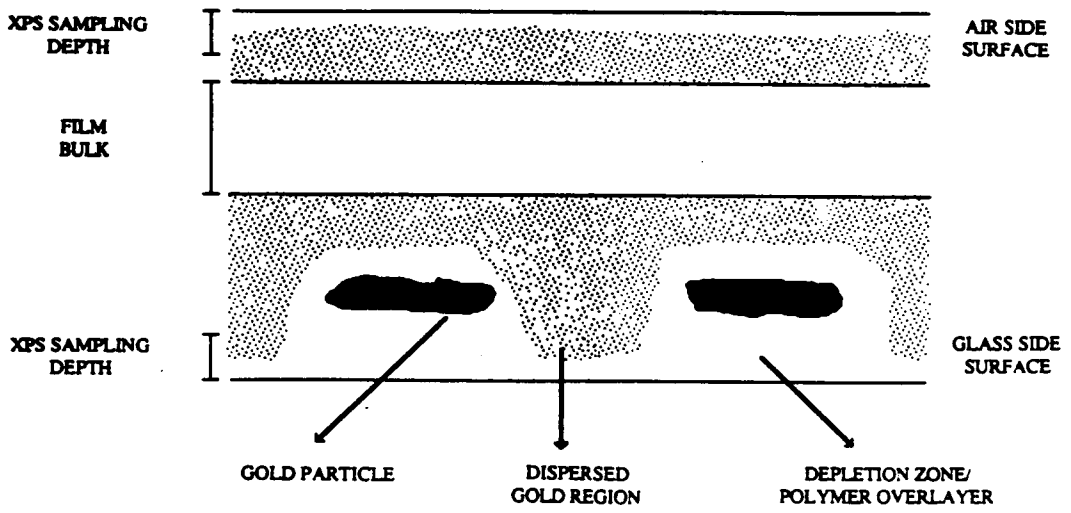

Figure 7. Schematic of near surface regions of modified BTDA-ODA based on XPS results.

large particles and segregation of the metal does not occur. Therefore, only one set of photopeaks is observed on the air side surface and photoelectron spectra typical of an unmodified film are observed.

The charging observed on the glass side surface was investigated further by evaporating a small amount of gold onto the polymer surface. The photopeaks of the glass side appeared unchanged from that of the uncoated sample except for one important difference. Two sets of gold peaks were now observed. This result would only occur if the gold deposited on the surface is at a different potential than the dispersed "native" gold particles. The two gold signals may come about as a result of the fact that the evaporated gold is electrically isolated from the native gold by the polymer overlayer. This result substantiates the model of a definite polymer overlayer on the glass side surface. It was also noted that the difference in binding energy between the two curve-fit signals is 2.6 eV, which is exactly equal to the difference in binding energy between the two sets of polyimide signals recorded in the C1s spectrum of Figure 4. That both sets of gold and polyimide photopeaks are offset by the same potential suggests that the depletion zones and the deposited gold are at one potential, while the polyimide with the dispersed gold is separated by a 2.6 eV potential. These

observations lend credence to the suggestion that the two sets of signals characteristic of the glass side surface arise from the distribution of gold in the insulative polymer matrix.

It was then suggested that if the double signal observed in Figure 6 was a result of differential charging between the depletion zones and the polymer containing dispersed gold, then charge neutralization by means of an electron flood gun may influence the observed spectrum. As the XPS used in this study was not equipped with a flood gun, the samples were analyzed on a spectrometer which had this option. However, this older spectrometer had lower resolution so that the identical sample produced somewhat different spectra (Figure 6 vs. Figure 8A). In any case, application of the flood gun produced two changes in the XPS spectrum of the glass side surface. First, the entire spectrum moved to lower binding energy due to charge neutralization by the electron gun. Second, and most important, the two peaks observed in the charged spectrum (Figure 8A) collapsed into one broad photopeak upon neutralization as is depicted in Figure 8B. This result would be expected if the electrons provided by the flood gun moderated the potential difference between the different regions of polyimide at the surface.

Discussion of the XPS results may be concluded by

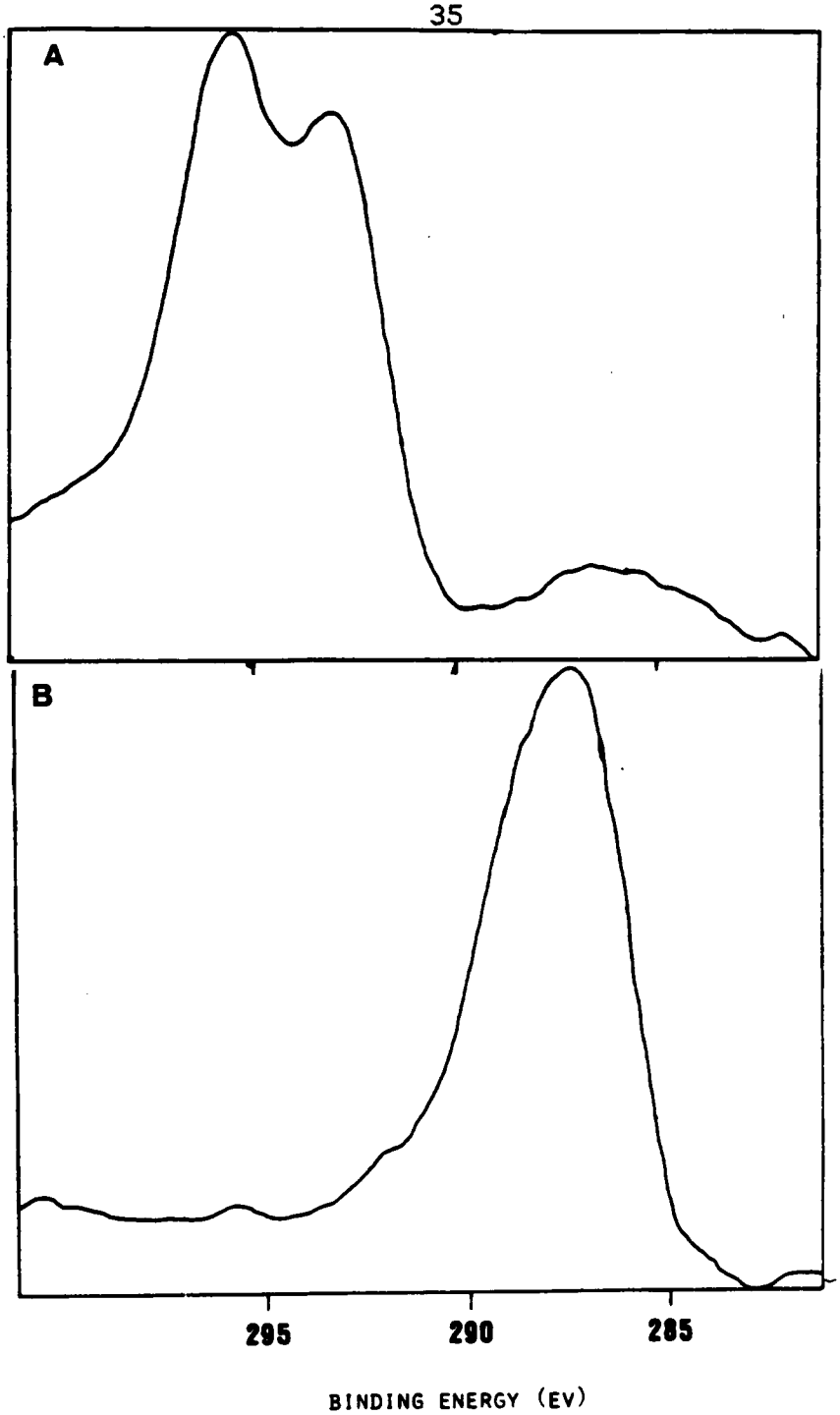

Figure 8. C1s spectra of glass-side surface of modified BTDA-ODA. A) Before charge neutralization; B) After charge neutralization.

noting that modification of polyimide films with chloroauric acid does not significantly enhance the concentration of metal at the film surface. Rather, the metal seems to lie just beneath a polyimide overlayer. The insulating nature of the polymer film complicates the photoelectron spectra, but does yield important information concerning the distribution of gold in the surface regions of these films.

3.2.5 Infrared Spectroscopy of Polyimide Films

The preceding XPS results showed that the polymer was essentially unaffected by the modification process and the thermal treatment. However, XPS only provides information concerning the surface regions of the film. Also, it is not particularly sensitive to subtle chemical modifications. For these reasons, infrared spectroscopy was used to evaluate the effect of modification and thermal treatment on the bulk chemical properties of the films.

Both the dopant and polymer were examined independently of one another and then combined in a modified film. The unmodified and modified solutions of polymers were prepared by the method outlined in the preceding chapter. The solutions were cast onto KBr salts plates and then heated 0.5 h. at 80° C and 1.0 h. at 100° C. The resulting films were analyzed in IR transmission mode, heated an additional

hour at 200° and 300° C, and reanalyzed. In this way, the condensation polymers could be analyzed in both the polyamic acid and the fully imidized state. The soluble polyimide is fully imidized and was only analyzed after the 300° C thermal treatment.

A concentrated solution of $HAuCl_4 \cdot H_2O$ in NMP was dried on a salt plate by heating the sample 0.5 h. at 80° C and one h. at 100° C. It appeared visually as if most of the dopant was reduced by this process. The spectrum was essentially featureless in the region from 4000 to 500 cm^{-1}. Reanalysis of this same sample after exposure to the high temperature thermal treatment (through 300° C), revealed the same featureless spectrum. Therefore, the metal additive is not IR active in the region of interest, which should facilitate the interpretation of the IR spectra of the modified polyimides.

The IR spectra of fully cured, unmodified and modified XU 218 films are shown in Figure 9. The three peaks characteristic of the polyimide structure were identified at 1780, 1380 and 725 cm^{-1}. The nearly exact location and relative intensities of the peaks suggested that gold incorporation did not affect the chemical nature of the soluble polyimide.

The effect of metal incorporation on the condensation polyimide BTDA-ODA was also studied. In addition, two

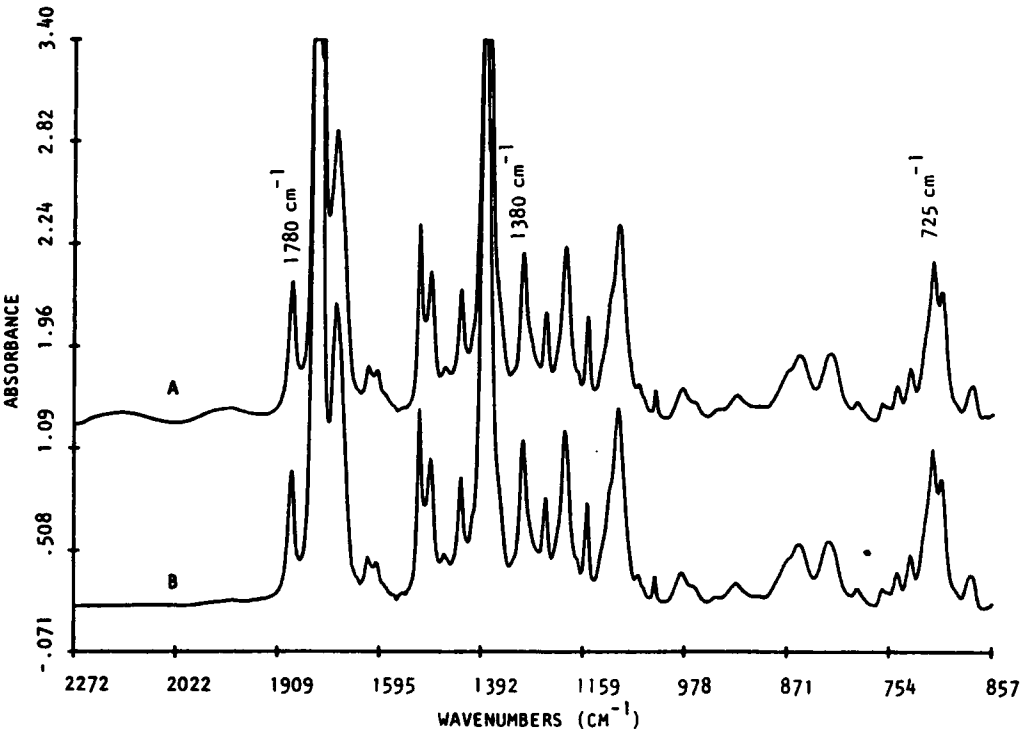

Figure 9. Infrared spectra of XU 218 after the 300°C cure. A) Unmodified; B) Modified.

other condensation polyimides, BTDA-DAPI and BTDA-DDS were evaluated. The BTDA-DAPI film was included as it represented the polyamic acid version of XU 218; that is, thermal treatment should produce the same material as XU-218. The low temperature unmodified film spectra are shown in Figure 10. The 100° C thermal treatment does not appreciably promote the imidization reaction as evidenced by the very small absorbance at wavenumbers characteristic of the polyimide. Furthermore, there are three bands present at 1722, 1664 and 1543 cm^{-1} which indicate that the polyamic acid is the predominate form.

The IR spectra of the modified versions of these three polyamic acids, exposed to the same low temperature treatment as the previous samples, are shown in Figure 11. As expected, the three peaks characteristic of polyamic acid were observed in each of the spectra. However, it was also noted that the three peaks representative of the polyimide were also present. Apparently, addition of the metal additive to the polyamic acid partially promoted the imidization of the polymer such that a mixture of both polyamic acid and polyimide is formed. The hygroscopic nature of the dopant seemed to partially dehydrate the polyamic acid.

The preceding samples were then placed back in the oven and exposed to the high temperature thermal treatment.

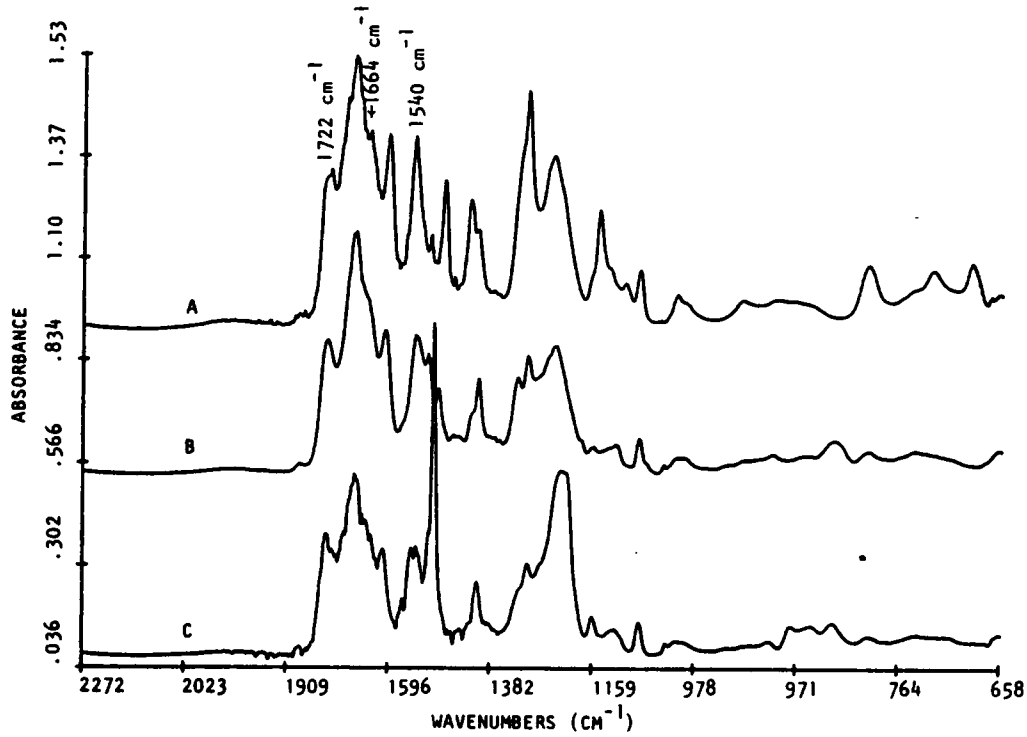

Figure 10. Infrared spectra of unmodified, 100°C cured films. A) BTDA-DDS; B) BTDA-DAPI; C) BTDA-ODA.

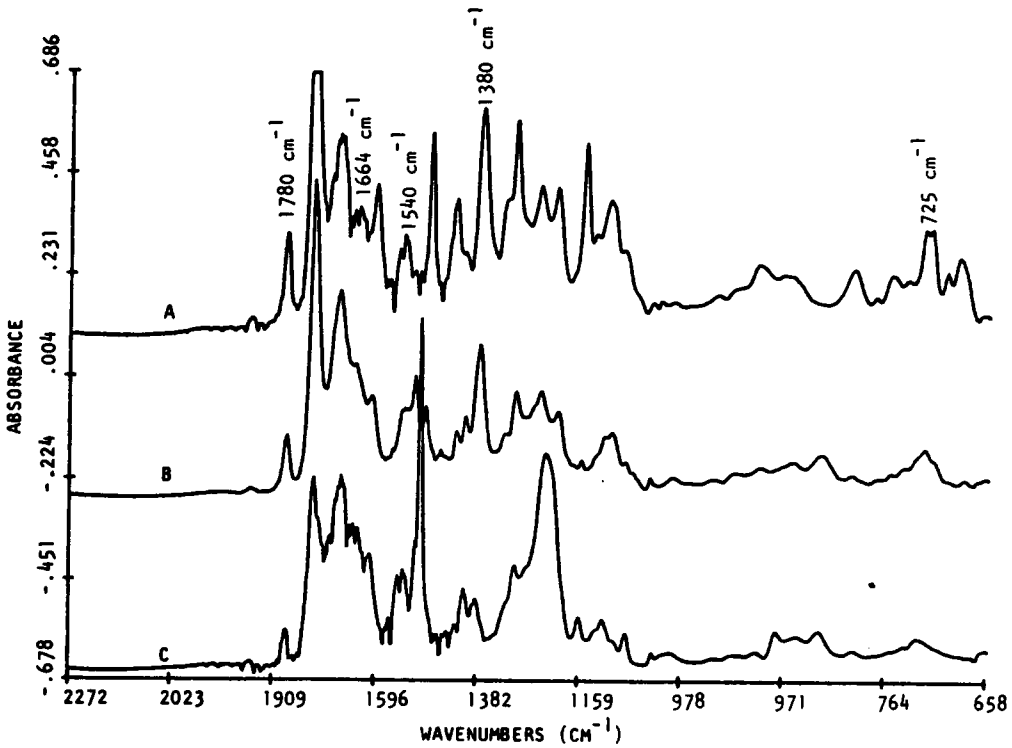

Figure 11. Infrared spectra of modified, 100°C cured films. A) BTDA-DDS; B) BTDA-DAPI; C) BTDA-ODA.

Figure 12 displays the spectra of the unmodified films. All of the spectra indicate that the polymers are in their fully imidized state. In this case, the three polyimide bands are fully developed. The polyamic acid bands located at 1543 and 1722 cm^{-1} are no longer observed. There is a band still present at 1670 cm^{-1}; however, the absorption is not due to the polyamic acid groups and probably represents an overtone or combination band.

The spectra of the modified films are shown in Figure 13. Comparison of these spectra with the unmodified films (Figure 12) indicated that all three modified films are chemically identical to the unmodified films. Therefore, modification does not alter the chemistry of the polymer, as observed in the three condensation polyimides and the soluble polyimide. The only effect attributed to the modification process was the promotion of the imidization reaction.

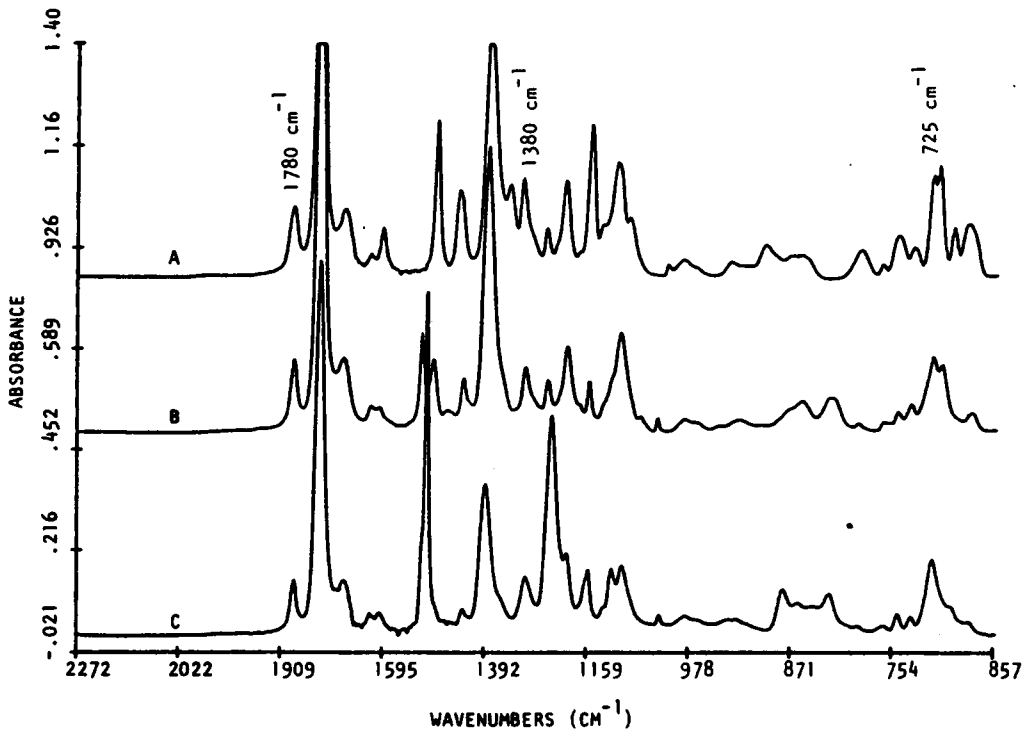

Figure 12. Infrared spectra of unmodified films, 300°C cure. A) BTDA-DDS; B) BTDA-DAPI; C) BTDA-ODA.

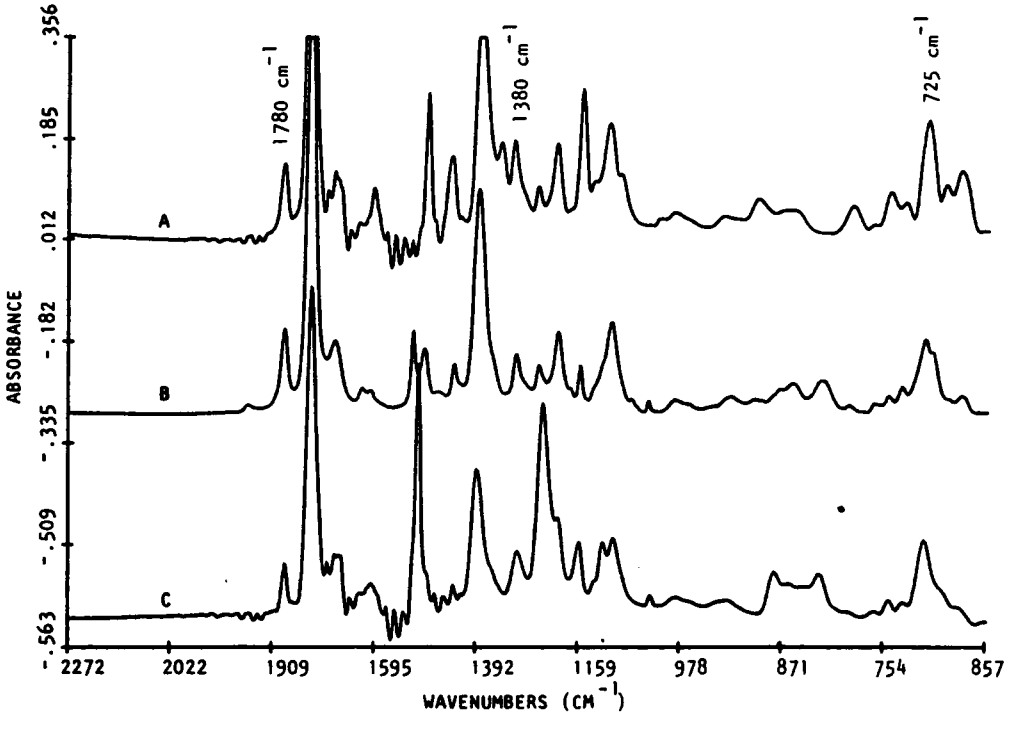

Figure 13. Infrared spectra of modified films, 300°C. A) BTDA-DDS; B) BTDA-DAPI; C) BTDA-ODA.

CHAPTER 4

NUCLEATION AND GROWTH OF GOLD DOMAINS IN POLYIMIDE FILMS DURING THERMAL TREATMENT

4.1 INTRODUCTION

During the thermal treatment of gold modified polyimide films, the metal can either disperse into discrete particles throughout the polymer matrix, or aggregate at the surface or near-surface of the film. The former distribution has been labeled bulk metalization, whereas the latter is termed surface metalization. The mechanics of phase separation and aggregation in the gold modified polyimide films will be discussed in some detail. The intent of this chapter is to quantitatively describe the nucleation and growth of the gold domains during thermal treatment.

The first section of this chapter will present some detailed information concerning the spatial distribution of gold in the polymer. Optical microscopy was used in the second section to study phase separation. As the term is used here, phase separation is the process by which an initially homogeneous modified film segregates into a gold phase and a matrix phase during thermal treatment. In the third section of this chapter, the formation of colloidal gold was examined by ultra-violet/visible spectroscopy.

The three preceding sections deal primarily with the

gold domains in the polymer film. In the fourth section, the influence of the imidization reaction on the surface metalization process was examined.

Before outlining the experimental results, the phenomena of phase separation will be discussed briefly. The theories presented here are central to the thermodynamics of phase separation, and will be related to the experimental observations. Nucleation and growth represents one mechanism by which phase transformation may occur. As discussed by Mullins [18], the boundary between the two resulting phases is said to possess a composition gradient which is large in degree and infinitesimal in spatial extent (a very sharp change in composition at the phase boundary). An example would be an infinitesimal droplet with properties approaching those of the bulk supercooled phase. On the other hand, spinodal decomposition produces phase separation which is infinitesimal in degree and large in extent (a slowly changing gradient in composition). In this case, the resulting phases exhibit a continuous change in composition.

As defined by Turkevich, nucleation is "the process whereby a discrete particle of a new phase forms in a previous single phase system" [19]. Two distinct types of nucleation are recognized. Homogeneous nucleation, which occurs spontaneously in a supercooled solution, and is

probably the type of nucleation Turkevich had in mind in the above definition. Heterogeneous nucleation usually occurs on the surface of a small foreign particle in the system; these particles may be intentionally added, as in the case of nucleating agents, or nucleation sites may be present due to dirt or other sample heterogeneities.

The thermodynamics of homogeneous nucleation will now be considered. The overall excess free energy ΔG, between the condensed phase, (an incipient nuclei) and the supercooled solution is equal to the sum of the surface excess free energy ΔG_s and the volume excess free energy ΔG_v:

$$\Delta G = \Delta G_s + \Delta G_v \qquad 4\text{-}1$$

where the value of ΔG is calculated relative to the standard state value of a flat surface. The term ΔG_s is a positive quantity as energy must be used to create the surface of the nucleus. However, ΔG_v is negative in the supercooled liquid. If spherical nuclei are assumed, then ΔG_s will increase with the square of the radius while ΔG_v decreases with the cube. Equation 4-1 can be rewritten for a spherical particle as

$$\Delta G = 4\pi r^2\gamma + 4\pi r^3\Delta G_v/3 \qquad 4\text{-}2$$

The two terms on the right hand side of equation 4-2 are plotted as a function of radius as is shown in Figure 14 [20].

The sum of the two curves ΔG, goes through a maximum at r^*. The change in free energy needed to create the critical nucleus r^*, is denoted ΔG^*. When $r > r^*$, growth of the nucleus is favored; however, particles of a radius $r < r^*$, will dissolve back into solution.

The value of ΔG^* is a maximum and can be found by setting $d\Delta G/dr = 0$. Using equation 4-2

$$d\Delta G/dr = 0 = 8\pi r\gamma + 4\pi r^2\Delta G_v \qquad 4\text{-}3$$

and therefore,

$$r^* = -2\gamma/\Delta G_v \qquad 4\text{-}4$$

By combining Equation 4-4 and 4-2, it can be shown that the change in free energy needed to form r^* is

$$\Delta G^* = 4\pi\gamma r^{*2}/3 \qquad 4\text{-}5$$

Equation 4-5 describes the "energy barrier" that must be surmounted in order to create a stable nucleus.

The free energy necessary to form the critical nucleus

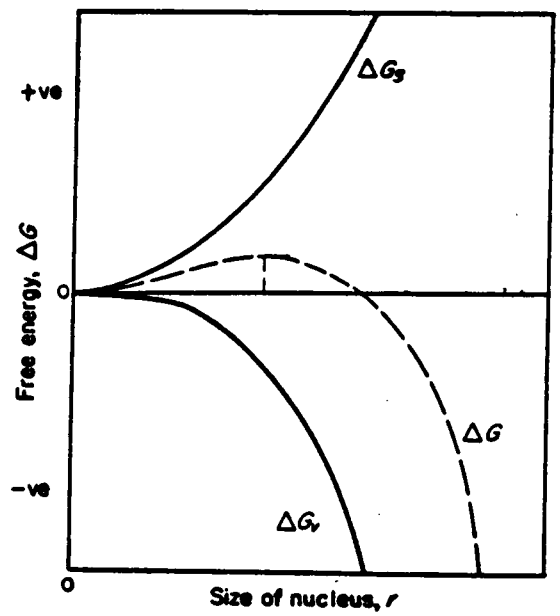

Figure 14. Free energy ΔG, as a function of radius. The ΔG cure is the sum of the ΔG_m and ΔG_v curves (from Reference 20).

ΔG^*, can arise from the statistical nature of a large assembly of atoms. In some regions of space, a sufficient number of atoms will possess enough energy to form a thermodynamically stable nucleus of radius r^*. Once formed, these nuclei can lower their free energy by growth.

The previous model, known as fluctuation theory, is necessary to postulate the formation of a critical nucleus in the initial step of phase transformations. A further assumption is that a sharp interface exists between the nucleus and liquid phase. Concentration fluctuations are also implicit in phase separation by spinodal decomposition. In this case though, no assumptions are involved concerning the interface between the two phases; indeed, a diffuse interface may exist.

Figure 15A shows the free energy diagram of a two component system [20]. If an initially homogeneous, one phase mixture has a composition of 0.5B, then small fluctuations in concentration, 0.5B + dC and 0.5B - dC, will decrease the free energy of the system. Indeed, all compositions which exist in the region where d^2G/dX_B^2 is negative (concave down) will spontaneously separate into two phases. The compositions at which $d^2G/dX_B^2 = 0$ (the inflection points) define the spinodal composition, and are traced out in the phase diagram as a function of temperature in Figure 15B. Within the spinodal region, any fluctuation

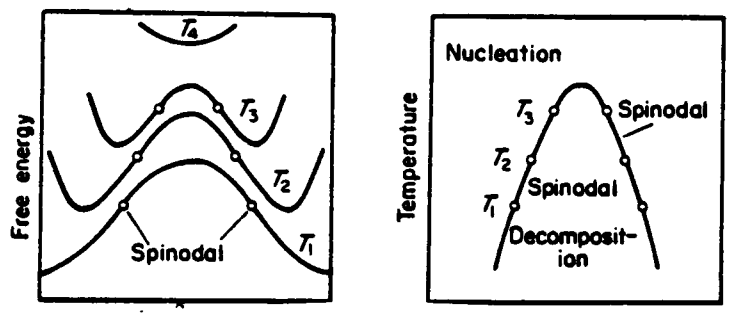

Figure 15. Thermodynamics of spinoidal decomposition. A) Free energy diagram as a function of alloy composition at four different temperatures. B) Phase diagram showing the spinoidal region (from Reference 20).

in concentration is "critical" and phase separation will occur without nucleation. Outside the spinodal region, phase separation may occur by nucleation.

In order to visualize the mechanism of spinodal decomposition, it is useful to consider the diagram in Figure 16 [21]. The value C_o represents the average composition in a two component, one phase system prior to phase separation. If this two component system is cooled down into the spinodal region of Figure 15B, then phase separation will proceed by fluctuation. In this case, fluctuations in composition are represented by a sine wave. These fluctuations occur spontaneously and decrease the energy of the system. The gradient in concentration (amplitude of the sine wave) will increase with time until the system divides into regions of the equilibrium composition indicated by the phase diagram.

There are two important features of spinodal decomposition that should be noted. First, diffusion occurs spontaneously "up" the concentration gradient. This seemingly anomalous behavior is allowed since the system free energy is lowered by this process. Secondly, spinodal decomposition gives rise to a periodic structure, with a characteristic wavelength. An example of phase separation by spinodal decomposition is the G-P (Guinier-Preston) zones observed in a variety of quenched cooled alloys [20]. The

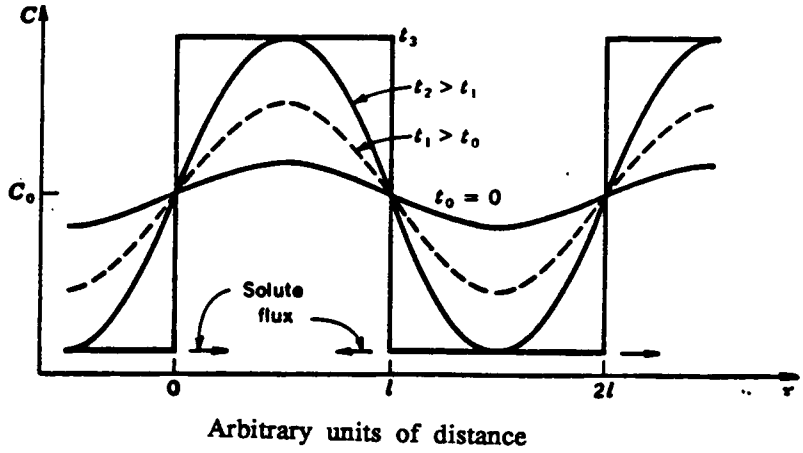

Figure 16. Compositional fluctuation as a function of distance in phase transformation by spinoidal decomposition. The composition gradient increases with time as indicated by the amplitude of the sine wave (from Reference 21).

G-P zones are approximately 2-4 nm in diameter and give rise to a scattering maxima in small angle X-ray scattering spectroscopy (SAXS). The relationship between phase separation, spinodal decomposition and SAXS will be discussed further in Chapter 5. At this point though, it is useful to consider a topic of great importance to these films; that is, the nucleation and growth of the colloidal phase of gold in aqueous sols.

The following discussion of the nucleation and growth of gold sols describes "classic" experiments performed by Turkevich [19]. In general, colloidal gold can be made in a variety of ways. However, most sols are produced by reacting an appropriate reducing agent with a boiling aqueous solution of chloroauric acid, $HAuCl_4$. Typical reducing agents include acetylene, phosphorous and citric acid. It was also noted by Thiessen that UV light produced colloidal gold in solution[22]. Turkevich found that sodium citrate produced colloidal nuclei with an average diameter of 20 nm. After approximately five minutes of reaction time, the solution turned a "wine red" color, which is indicative of light absorbtion in the uncoagulated sol.

In order to study the nucleation rate, Turkevich removed aliquots of the reaction mixture and placed them into a hydroxylamine- chloroauric acid "developer" solution [23]. This solution grew the nuclei to a size that could be

studied by the electron microscopes of the day, without causing any further nucleation. The nucleation curve obtained by this method is shown in Figure 17 [19]. In general, the shape of this curve is characteristic of an autocatalytic reaction. This curve was broken down into four regions. The first region corresponded to the induction period where no colloidal gold was formed. The second region showed a rapid increase in the formation of nuclei, which gave way to the linear portion of the third region. The fourth region was characterized by the decay and final exhaustion of nucleation. The overall shape of the curve is characteristic of the kinetics followed by an autocatalytic reaction.

Examination of the induction period indicated that the duration of this time increased with decreasing temperature. From the calculated induction time at four different temperatures, an activation energy of about ten kcal/mole was estimated. Further studies showed that the induction period was the time necessary to form acetone dicarboxylate from the citrate ion. If the sol is formed directly from acetone dicarboxylate rather than citrate, then no induction time is observed and nucleation commences immediately.

In region II, it was noted that the second derivative of the curve d^2N/dt^2, increased with increasing temperature. That is, the autocatalytic nature of the reaction was more

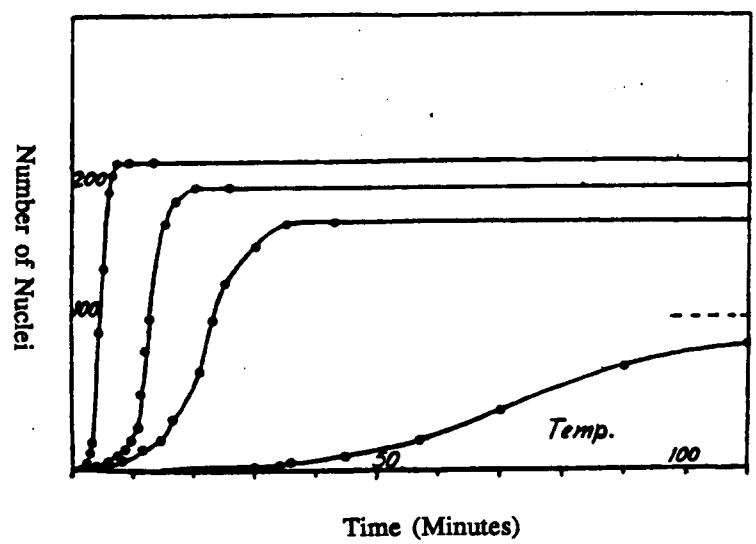

$T_1 < T_2 < T_3 < T_4$

Figure 17. Nucleation rate as a function of time at three different temperatures in aqueous gold sols (from Reference 19).

pronounced at higher temperatures.

In Region III, the linear portion of the nucleation rate curve was fit to the equation:

$$N_t = N_\infty (1-e^{-kt}) \qquad 4-6$$

where N_t and N_∞ are the number of nuclei present at time t and infinity, respectively. The data from the linear region of Figure 17 were graphed in terms of Equation 4-6, and was found to be linear. Turkevich concluded that the rate determining step for nucleation was the unimolecular decomposition of a gold-acetone dicarboxylate complex.

Region IV showed a cessation of nucleation, even though 95% of the chloroauric acid was unreacted at the end of the nucleation process. Apparently, acetone dicarboxylate was no longer able to produce the gold nuclei. It was suggested that this material was either decomposed, or adsorbed onto the surface of the nuclei and was used as a reducing agent in particle growth.

Turkevich proposed the following mechanism of nucleation in the citrate sol. Nuclei were not thought to form by fluctuations in the density of gold atoms, which give rise to the critical size needed for a stable nucleus. Rather, a polymerization occurred between the difunctional acetone dicarboxylate and gold ions. When the degree of

polymerization is sufficiently large, decomposition occurs and forms the stable gold nucleus ($r > r^*$).

The growth of the nuclei depended on the concentration of chloroauric acid in solution. By inoculating the developer solution with gold nuclei, Turkevich derived the following growth equation:

$$D_f = D_n[(Au + Au_s)/Au_n]^{1/3} \qquad 4\text{-}7$$

where D_f is the final diameter of a growing particle, D_n is the diameter of the added nuclei, Au_n is the weight of the gold nuclei and Au_s is the weight of gold in solution.

Using Equation 4.7, Turkevich was able to grow a series of monodisperse sols of varying size. These sols were then used to verify the calculations of Mie, who related the optical absorbance of colloidal gold to particle size [24]. Maxima in the visible spectrum ranged from 520 nm to 630 nm as the particle size ranged from 20 nm to 160 nm [25]. In the next section, the nucleation and growth of gold in the polymer matrix was studied.

4.2 RESULTS AND DISCUSSIONS

4.2.1 Gold Distribution

The fully cured (through 300°C) XU 218 modified film synthesized by the procedure outlined in the introduction of

this chapter had surface features that were quite similar; that is, the atmosphere and glass side surfaces both appeared dark brown. Scanning electron microscopy (SEM) of the surfaces of the fully cured XU 218 films are shown in Figure 18A-D. The use of energy dispersion analysis of x-rays(EDAX) indicated that the particles are gold and do not contain chlorine. Figure 18A and B show the secondary image and the back scattered electron image, respectively, of the atmosphere side surface of the same region at 6400X. The secondary electrons arise from the top 10nm of the specimen, whereas the back scattered electrons are more representative of the bulk (1-2μm). The gold particles are ca. 1-5μm in diameter and seem to be embedded in the polymer matrix. Photomicrographs obtained from the glass side surface at 25,000X (Figure 18C and D) show particles of much smaller dimensions. The secondary electron image indicated that particles ca. 0.1-0.2μm populated the outermost surface. The backscattered electron image showed particles of even smaller dimensions that seemed to be embedded quite deeply in the polymer matrix. The discontinuous nature of the gold particles accounts for the dull surface and poor electrical conductivity of these films.

In order to relate the surface photomicrographs to the distribution of gold in the bulk of the film, small samples were embedded in epoxy and then cross-sectioned using an

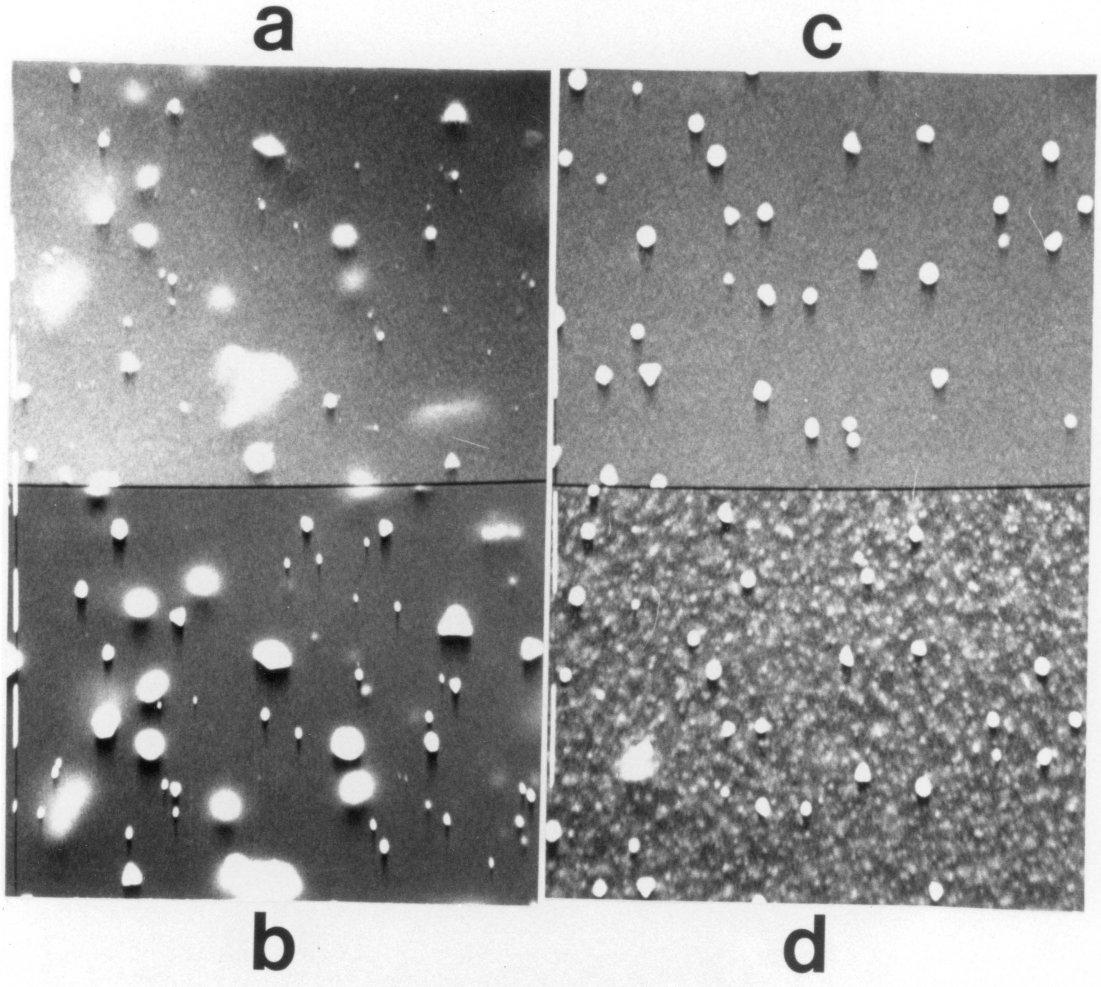

Figure 18. SEM of XU 218 film. A-B) Atmosphere side surface at 1600X. C-D) Glass side surface at 25,000X. A and C were collected with the secondary electron detector; B-D were collected with the backscattered electron detector.

ultramicrotome. The samples were then mounted on copper grids and examined by scanning transmission electron microscopy (STEM). Figure 19A and B show the entire cross section of the preceding film, which was ca. 30 μm thick. However, these particles are not random in their spatial distribution. A greater particle density was observed nearer the glass side surface than the atmosphere side surface of the film.

A fully cured BTDA-ODA film (heated through 300°) has surfaces markedly different from the bulk metalized film. The atmosphere side surface looks dark brown in color and is somewhat lustrous. The glass side surface appears metallic and looks bronze-gold in color. Optical and electron microscopy were useful in understanding how the gold distribution gave rise to the visual appearance of these surfaces. Figure 20 shows a 25,000X split screen SEM photomicrograph of the atmosphere side surface of a fully-cured BTDA-ODA film modified with gold. Two types of particles were characteristic of this surface: polyhedrons with an average diameter of 0.16 um and larger, trigonal planar shaped particles. Our previous investigations showed that the gold located on the atmosphere-side surface of these films was in the metallic state. Further, the morphology of these particles is quite similar to shapes observed by Turkevich [26] in aqueous gold colloids; this

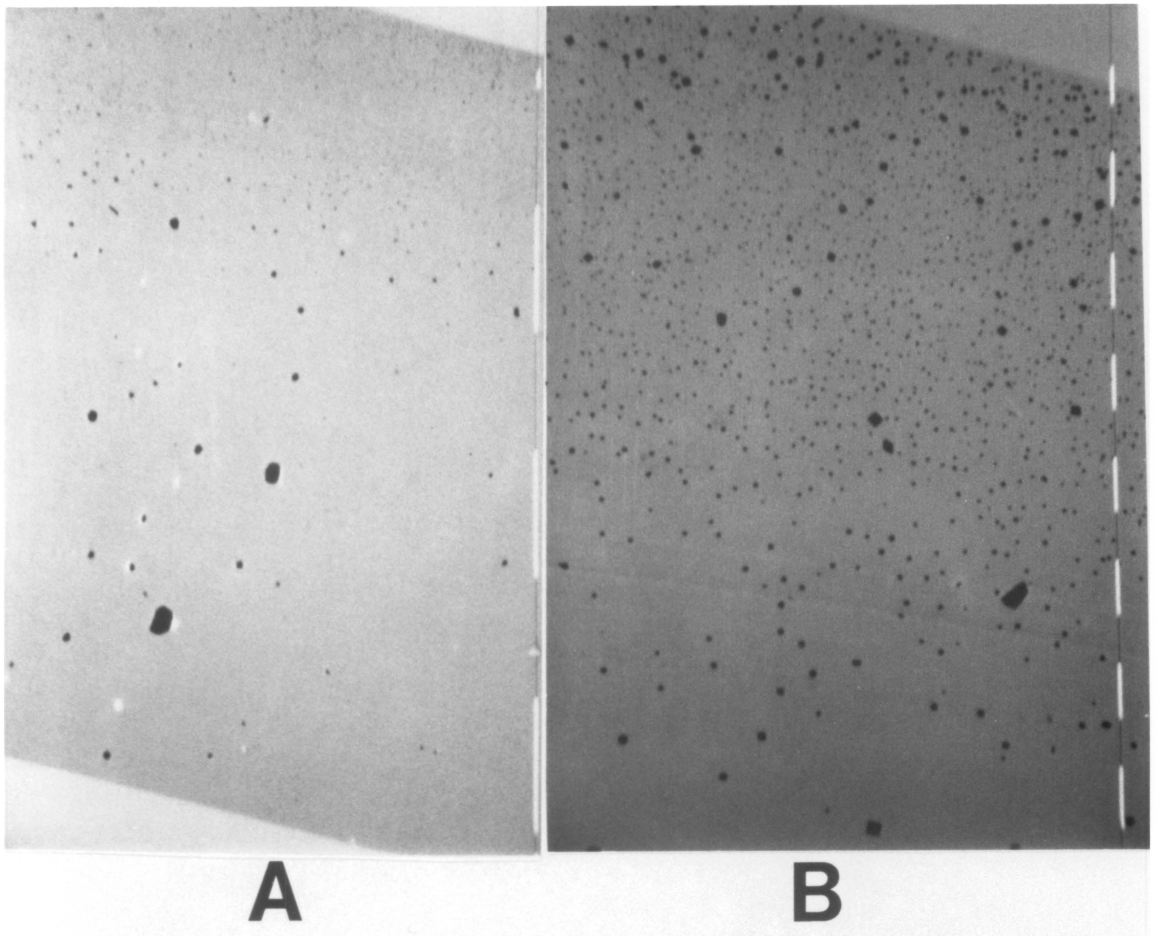

Figure 19. STEM analysis of a cross-section of a modified XU 218 film. A) Entire cross-section at 1600X. B) High magnification of glass-side surface at 25,000X.

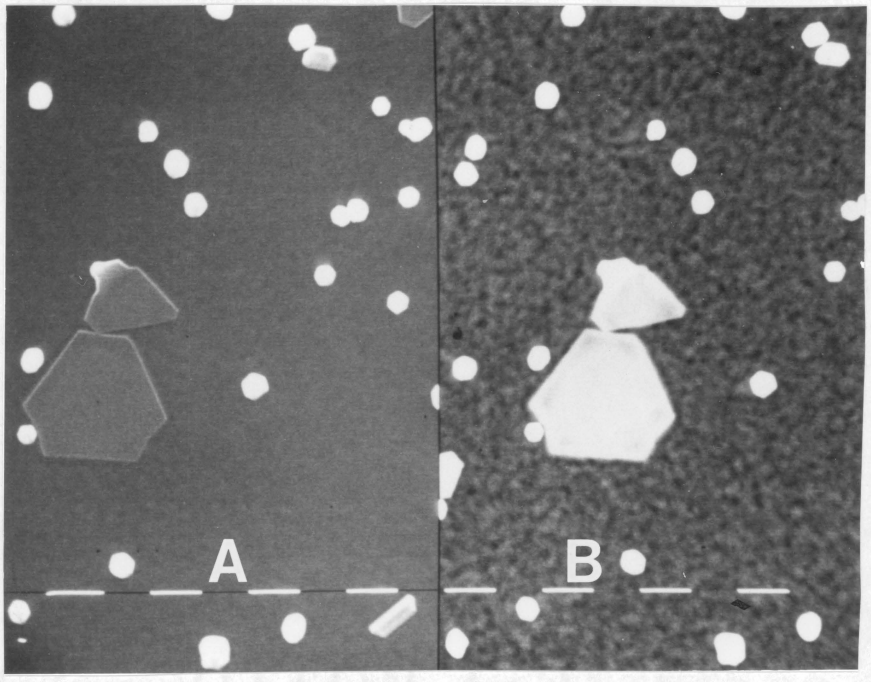

Figure 20. Air-side surface of a modified BTDA-ODA film at 25,000X. A) Secondary electron image; B) Backscattered electron image.

strongly suggests that colloidal gold was formed in this particular polyimide during thermal treatment. Turkevich attributed the triangular forms to "repressed" growth during colloid formation. Indeed, our SEM results are consistent with this observation. Figure 20 shows the backscattered electron image and the secondary electron image, respectively, of the same region of film. Backscattered electrons give a sharper image of the planar forms than the secondary electron image. Consequently, the planar forms seem to be embedded in the polyimide matrix, whereas the polyhedral particles are located much closer to the film surface. This seems reasonable since repressed growth of colloid particles would be more likely to occur in the polymer matrix than at the film surface.

The glass side surface of this same BTDA-ODA film is much different from the air side surface, as is shown by the reflected light photomicrograph (125X) in Figure 21. In general, the surface is comprised of metallic gold aggregates which are described by a bimodal size distribution. These features have been classified according to their shape. A Class I aggregate is the large (75-100 um diameter) structure which is slightly branched at the particle periphery. Class II particles are smaller (10-30 um diameter), more compact and the most abundant shapes observed on the glass side surface. Class III particles are

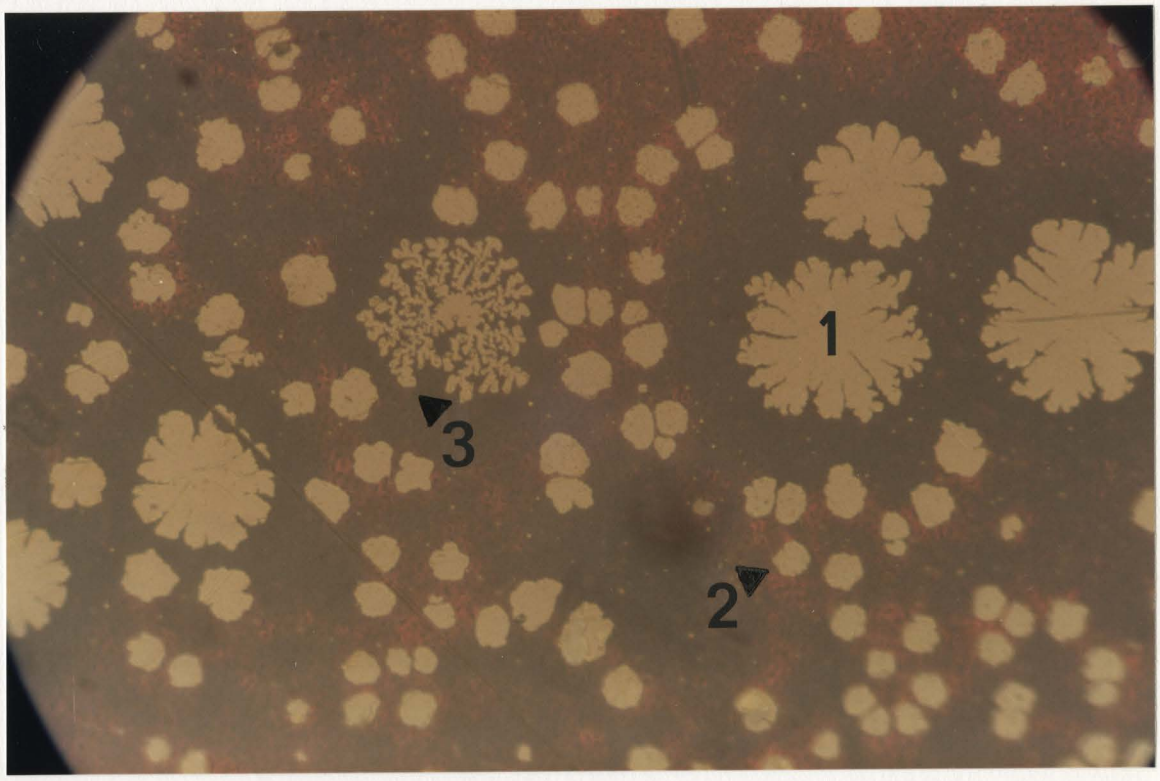

Figure 21. Glass-side surface of BTDA-ODA film at 125X by reflected light optical microscopy.

highly ramified and have a compact center with dendritic arms emanating from a central core. In some cases, a Class III type structure which lacks the central core has been observed; that is, the arms seem to emanate from a central point. All of these features have been shown to be gold in the metallic state. The distributions of particle sizes and shapes is thought to be influenced by the imidization reaction as will be discussed in a later section.

In addition to the film surfaces, the bulk distribution of metal was evaluated using STEM, by preparing ultramicrotome cross sections of a fully cured modified film. The photomicrograph of Figure 22A shows the entire cross section (30 um) of the film. The black band (ca. 1 um thick) across the bottom is actually a cross-section of one of the large glass side surface aggregates. Figure 22B is high magnification of the air side surface, which shows that the colloidal particles are restricted to a narrow region approximately 0.5 μm in depth. It is interesting to note that the interior of the film is almost devoid of particles, except for a few aggregates approximately 1 um in diameter. Most of the gold is, therefore, concentrated in the surface regions, either as colloidal particles at the atmosphere side surface or as very large, flat aggregates at the glass side surface.

The distribution of gold can be greatly affected by

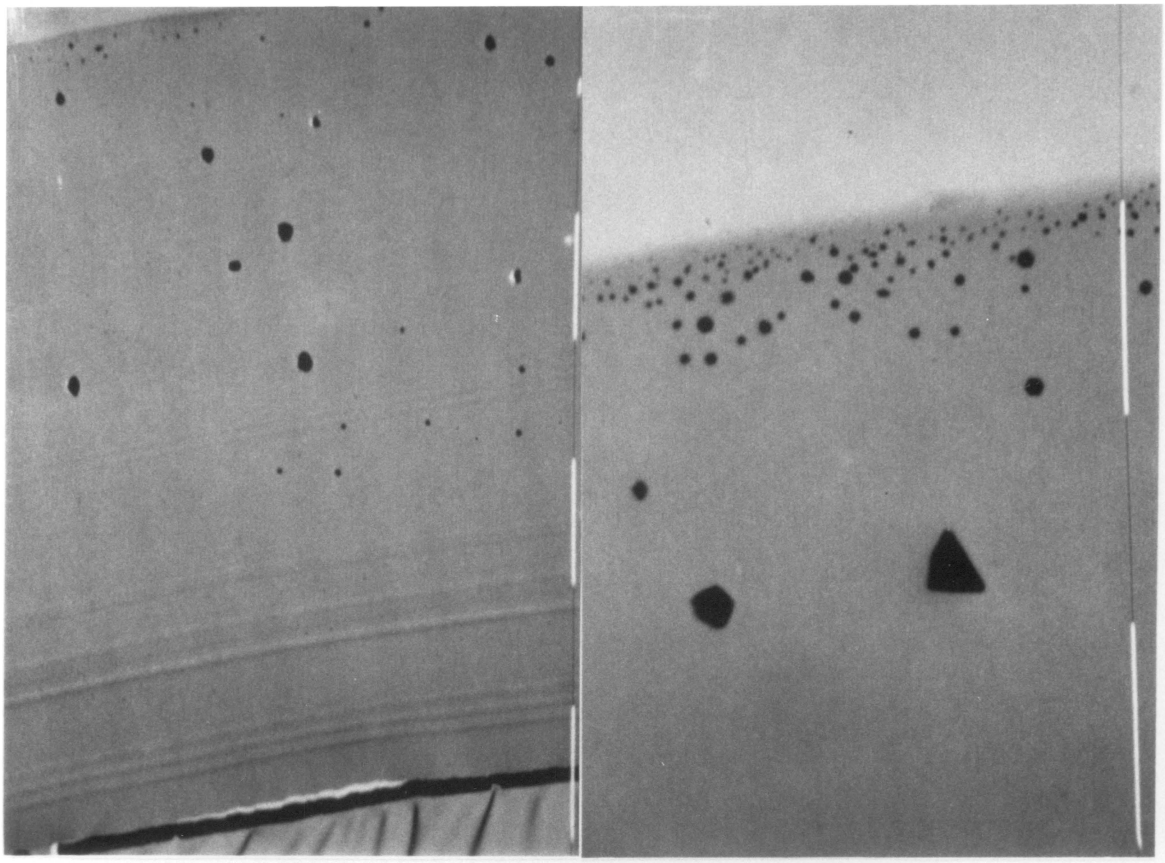

Figure 22. STEM analysis of a cross-section of a modified BTDA-ODA film. A) Entire cross-section at 1600X. B) High magnification of air-side surface at 25,000X.

changing the casting substrate during the thermal cure, as is illustrated by the following experiments. If the modified BTDA-ODA film is not in intimate contact with the glass casting plate during thermal curing, the large ramified features shown in Figure 21 did not form. This phenomenon was investigated by altering the casting surface in two different ways. In the first case, a film heated to 100°C was removed from the glass casting plate and suspended in the oven so that there were two "atmosphere" sides to the film during the rest of the cure cycle. In the second case, the surface of the glass plate was altered by coating a portion of the plate with MS136 (Miller Stephenson), a tetrafluoroethylene mold release. The doped solution was cast onto the plate so that one-half of the film coated glass and the other half coated the mold release. Since the mold release was present, the film was only exposed to a final temperature of 250°C for one hour. While the sample obtained in the second case was not exposed to the full thermal cure, glass side surface metalization will occur at this time and temperature.

The results suggest that the presence of the glass surface is necessary for the formation of gold aggregates in BTDA-ODA. In the first case cited above, the resulting film looked dark brown on both surfaces, which was similar in appearance to the atmosphere side surface of the film

prepared in the usual manner. STEM cross section of this film (Figure 23) showed a distribution of metal much different from the film cured on the glass casting plate in the usual manner (Figure 22). It is obvious that the large aggregates did not form at the surface and the bulk of the film is populated with small colloidal gold particles. The particles appear to be of many different sizes, but the majority are approximately 0.1 um in diameter and smaller. It should also be noted that the distribution of particles is also more uniform than in XU 218. However, both films appeared visually to be the same, and are classified as bulk metalizing films.

In the second case studied, the presence of the mold release clearly inhibited the formation of the glass side surface gold aggregates. Cross section analysis of a region of this film cast on the mold release showed no surface aggregates and a uniform distribution of gold particles in the bulk of the film. Conversely, the portion of the film cast on glass where no mold release was present had a gold-bronze glass side surface. The presence of the "glass" side aggregates and a lack of substantial colloidal gold in the bulk of the film was observed.

Since it was observed that the lack of a glass surface prevented large aggregate formation, it was of interest to attempt to induce the surface growth. Two experiments were

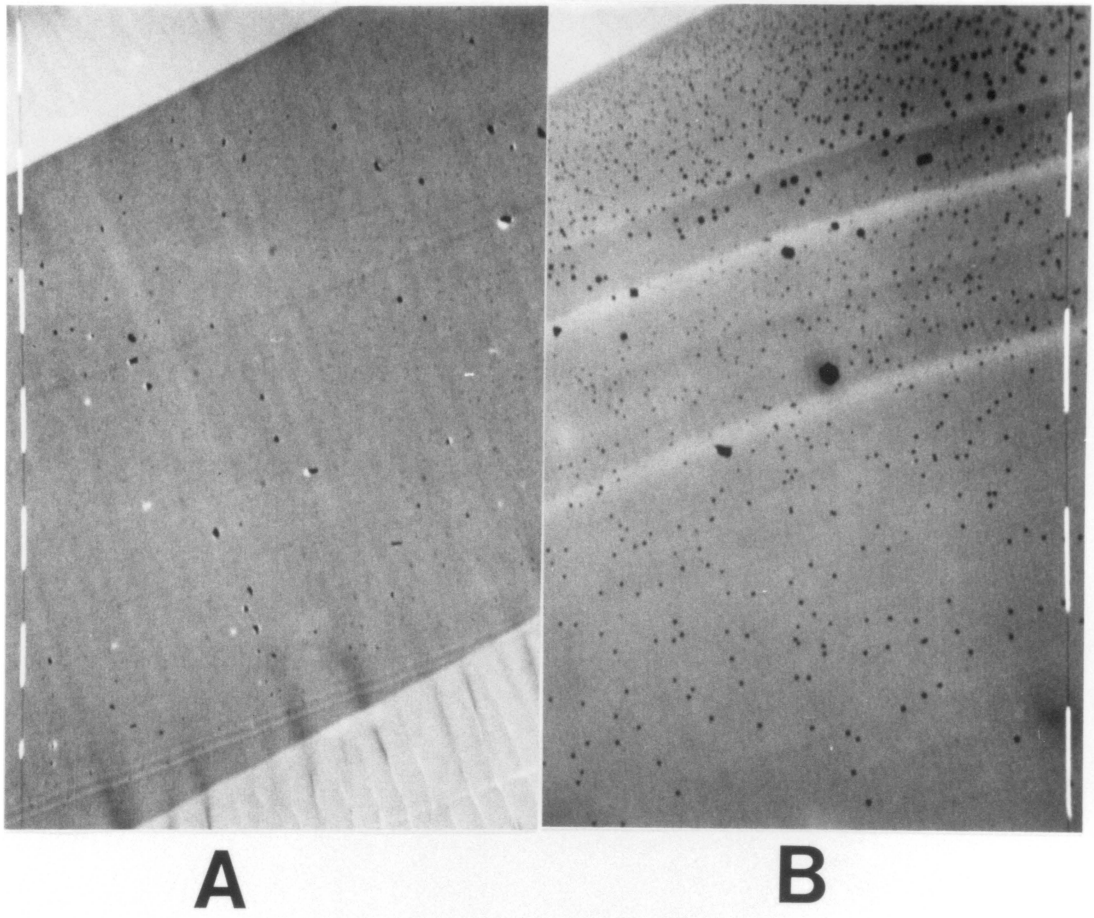

Figure 23. STEM analysis of a cross section of a modified BTDA-ODA film removed from casting plate prior to high temperature cure. A) Entire cross section at 1600X; B) High magnification of surface at 25,000X.

performed wherein new glass surfaces were introduced to the film. A 100°C heat-treated film was removed from the casting plate, sandwiched between two glass microscope slides, secured with tape, and heated through the full cure cycle. During the cure, the film adhered deferentially to the glass plates; that is, certain regions of the film adhered to one plate and other regions to the opposing plate, as is shown schematically in Figure 24. It was observed visually that only those surfaces of the film which stuck to the plates displayed the characteristic gold surface. Optical microscopy with reflected light verified that large aggregate formation occurred only at the glass/polymer interface. The regions devoid of aggregates on either surface of the film were "free standing" between the glass plates.

The growth process could also be promoted in the BTDA-ODA film by seeding the metal-containing solution with a small amount of Hi-Sil T-600 (PPG) glass beads. Electron microscopy indicated that the beads have an average diameter of 21 nm [27]. When modified BTDA-ODA polyamic acid solutions containing half the usual amount of dopant and glass beads were cast onto glass plates and cured, it was noted that the number of large Class I aggregates on the glass side surface was greater in a unit area than in a corresponding unseeded film. Taken together, the preceding

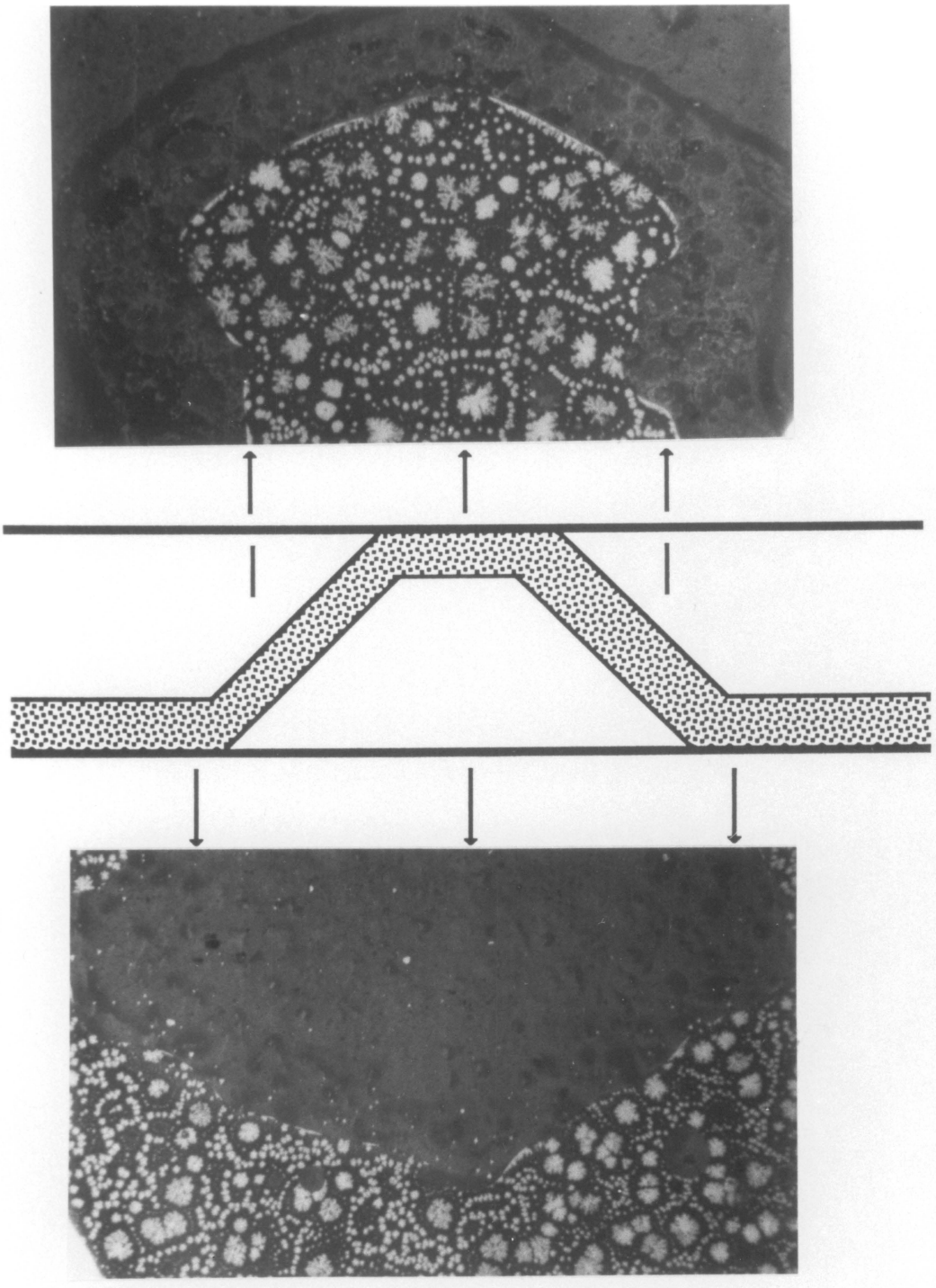

Figure 24. Schematic of modified BTDA-ODA film cured between glass plates. Reflected light stereomicroscopy examined same region of film from either side, 60X.

results indicate that the presence of glass is necessary for the formation of the large surface aggregates. The glass may either provide nucleation sites for the growth of the gold aggregates or specific surface chemistry which is necessary for surface metalization. Absence of the glass plate results in films that exhibit bulk metalization and a more uniform distribution of particles throughout the film.

4.2.2 Nucleation and Growth

Hot stage optical microscopy provided a means to emulate the thermal treatment while monitoring the nucleation and growth of the gold domains. The heating profile, atmosphere and casting surface used in the fabrication of larger films can be duplicated in the hot stage chamber. Further, the metalization process can be recorded by photomicrography via a 35 mm camera or closed circuit television.

However, there are some limitations to this technique. It was not possible to measure the nucleation and growth of the bulk metalizing films, because of the small size of the gold domains. However, some general trends were noted in these films. Also, it was not possible to study the full thermal treatment in either type of film, since they usually became opaque to transmitted light above 200°C.

Isothermal heating of a modified XU 218 100°C thermally

treated film in the chamber of the hot stage microscope at 200°C resulted in a chemical change in the film as evidenced by a color change. The initially transparent yellow film turned a wine red color over the course of ca. 1.0 hr. During this time a large number of small (about 2-5 μm in diameter) gold particles was observed to form in the film. The evolution of a modified film at 200°C is shown in Figure 25. The presence of the wine red color in the heated film is probably a manifestation of the formation of colloidal gold.

In addition to studying the metalization process in XU 218, two other polymers were studied: the polyamic acids BTDA-DDS and BTDA-DAPI. Both films were prepared in the same manner as the 100°C thermally treated XU 218 film. The two different forms of the BTDA-DAPI film (soluble polyimide and polyamic acid) allowed for the evaluation of the imidization reaction on the overall metalization process. However, it was noted that full thermal treatment produced dark brown films, all of which appeared visually to be quite similar to the XU 218 film. Not surprisingly, these films exhibited the same metalization process as XU 218 when observed by hot stage optical microscopy. Heating isothermally at 200°C promoted the formation of the 5 μm bulk particles and the colored background.

In conclusion, bulk metalization appeared to be

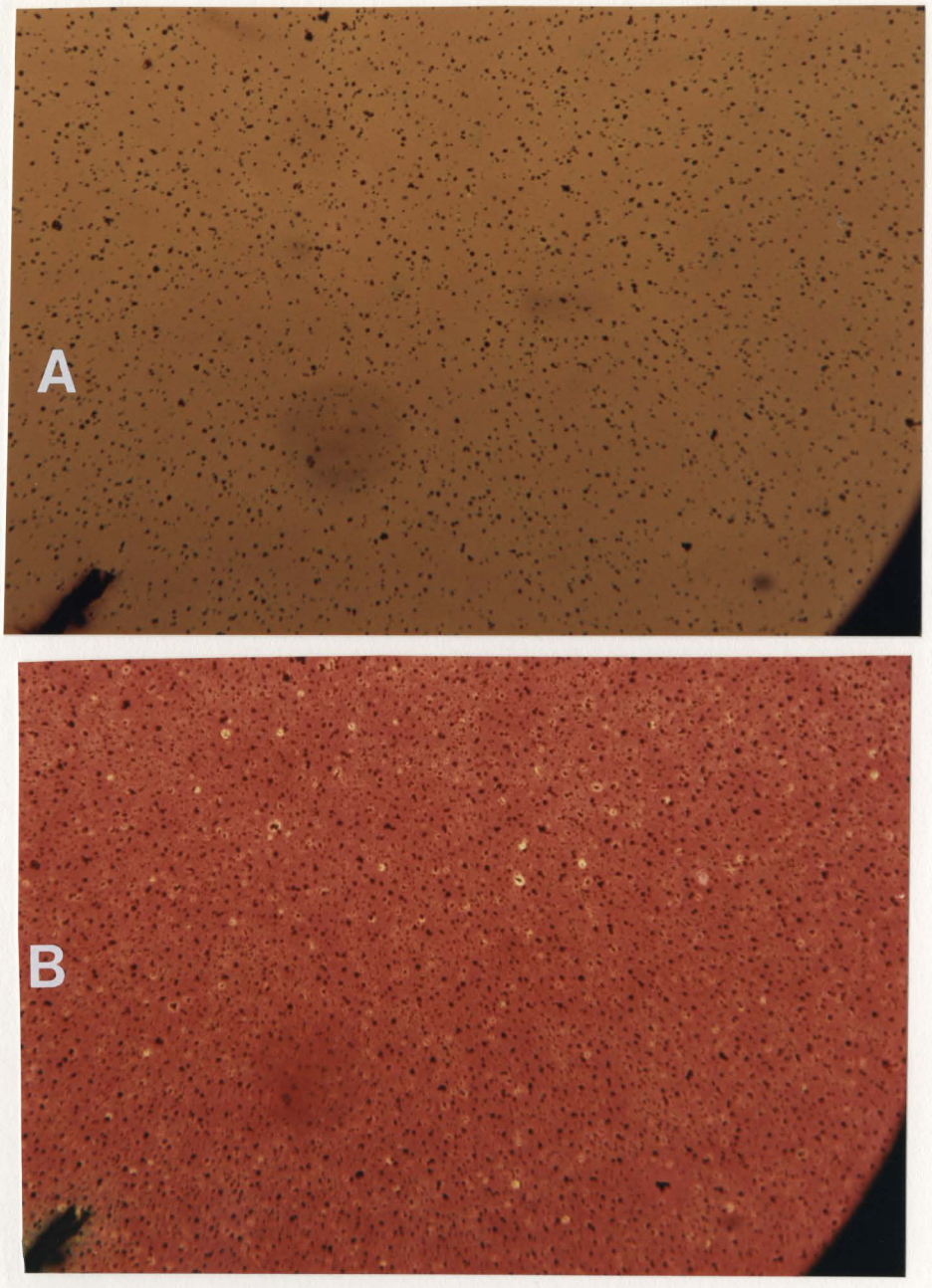

Figure 25. Hot stage optical microscopy of modified XU 218 film as a function of time at 200°C. A) 22 minutes; B) 35 minutes.

accompanied by two distinct events; the formation of a colloidal gold "background" and the appearance of much larger (2-5 μm) bulk particles. Evidence for the formation of colloid was also suggested by the very small particles (10-50 nm) located in the bulk of the film. Further, bulk metalization did not seem to depend on the chemical or physical state of the polymer. Variation of the chemical composition (XU 218 versus BTDA-DAPI) did not seem to alter the phase separation. However, the polyimide discussed in the next section exhibited unique behavior. Instead of forming only small bulk particles, large metallic gold aggregates were formed on the glass side surface of the film.

The glass side surface metalization process was evaluated further by studying the nucleation and growth of the Class I and II aggregates. The nucleation rate was measured by placing a 100°C modified BTDA-ODA film in the optical microscope hot stage chamber, ramping the temperature to a given isotherm, and photographing the changes which occurred as a function of time, as shown in Figure 26. Because of the scarcity of the Class III aggregates in films prepared in this manner, it was not possible to record their nucleation and growth rate. The graph shown in Figure 27 summarized the nucleation rate at 160°, 175° and 200°C by indicating the total number of

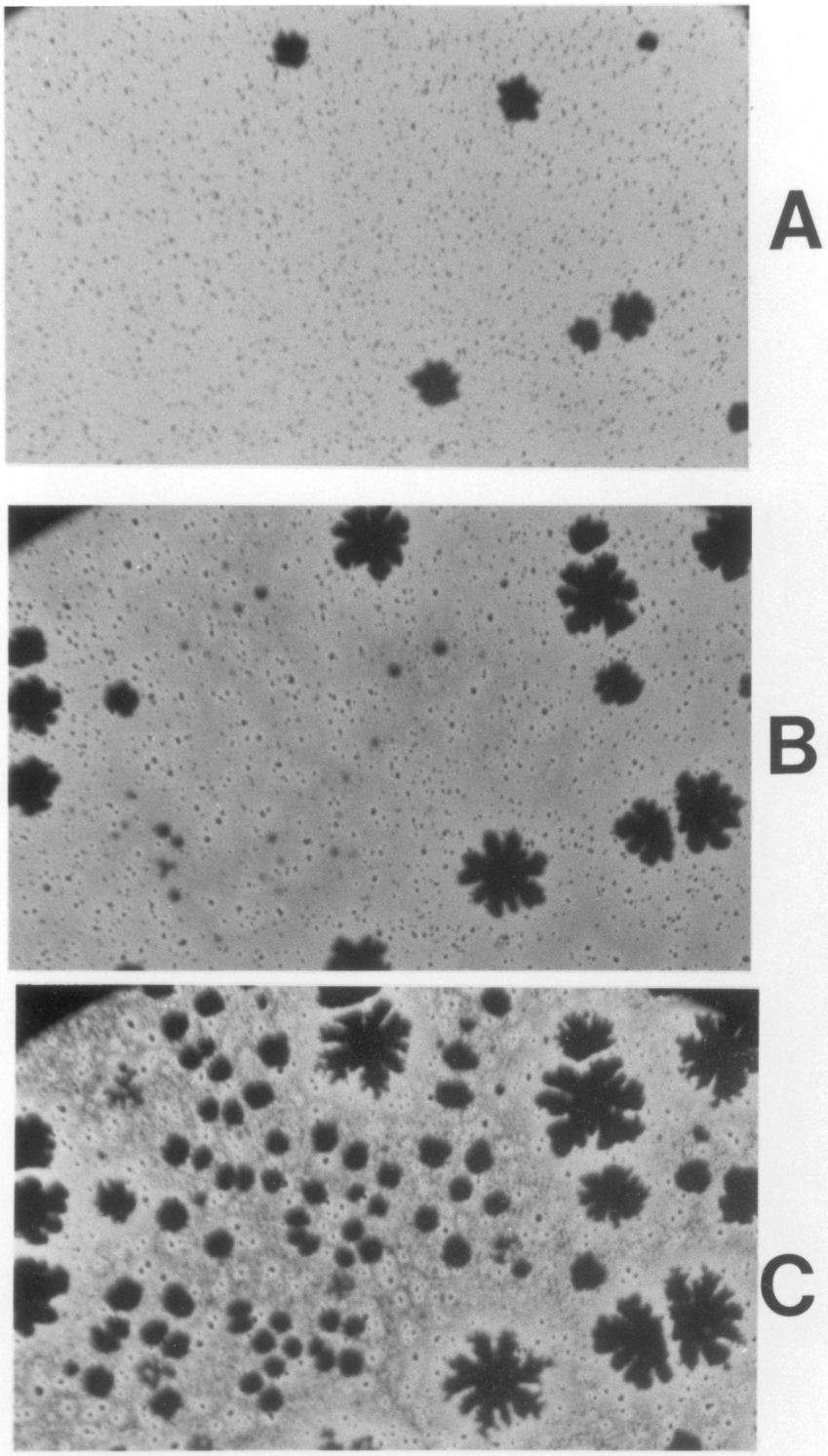

Figure 26. Hot stage optical microscopy of modified BTDA-ODA film as a function of time at 175° C. A) 23 minutes; B) 40 minutes; C) 73 minutes.

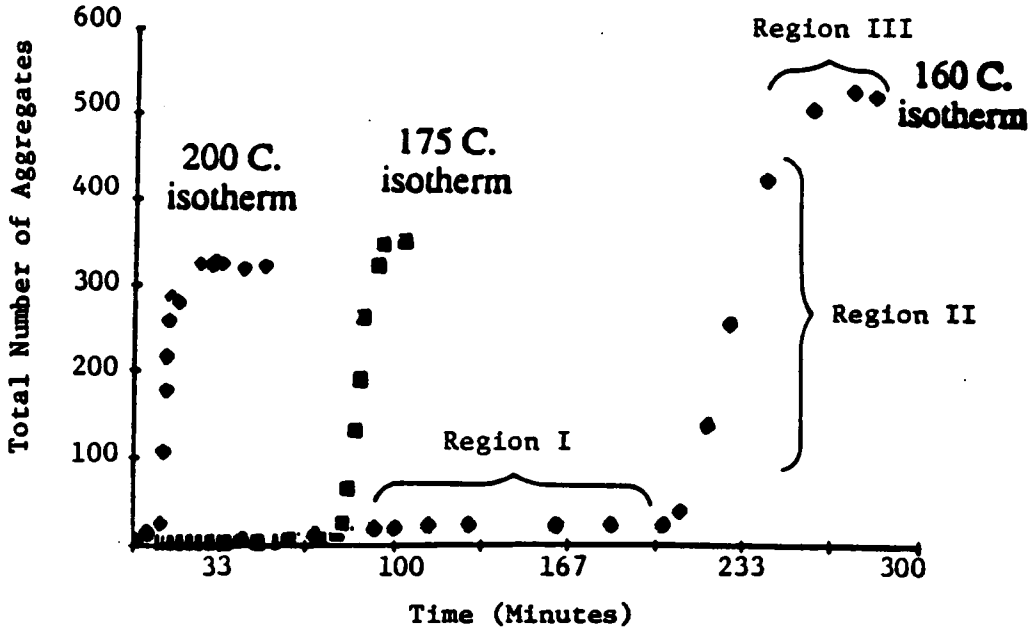

Figure 27. Total number of nuclei observed as a function of time at the indicated isotherms.

aggregates observed as a function of time. Regardless of temperature, the process of nucleation followed the same general pattern as can be seen by the similarity of the nucleation rate curves. Three distinct regions can be assigned in these curves. Region I corresponds to initial formation where a slow nucleation rate was observed. Region II is characterized by a sharp increase in rate as numerous new nuclei formed in a relatively short period of time. Region III is the zero slope plateau where nucleation ceased.

The shape of the nucleation rate curves can be correlated to the type of aggregates formed. In Region I, after an initial induction time, small particles appeared at a slow rate of nucleation and eventually grew into the large structures labeled as Class I aggregates in Figure 21. After these large particles substantially slowed in growth, many new small particles quickly formed, as is indicated by the large increase in nucleation rate in Region II. It was also noted at this time that the film appeared to darken. The point at which the nucleation rate increased dramatically and the background darkened is called the crossover point and will be discussed in detail in Chapter 5. The type of particles which were ultimately formed by this tremendous increase in nucleation rate were the Class II aggregates. In Region III, no new particles formed at

the indicated isothermal temperature.

The term, nucleation, as used here, refers to the observation of a gold "nucleus", as seen visually at 125X with a light microscope. Turkevich previously theorized that the gold particles comprising a citrate sol were formed from nuclei 40 nm or smaller in diameter. Nevertheless, he studied the process of nucleation by developing the incipient nuclei to a size that could easily be studied by the electron microscopes of the day. Therefore, the particles observed by light microscopy in this present study are not nuclei in the sense that they formed directly from a phase transition in the gold/polymer film. Rather, the term applies to the observance of a gold particle which has grown to a size that can readily be studied (ca. 5 um in diameter).

It was observed that there is an induction time for the formation of both the Class I and II aggregates. The Class I particle induction time is simply the elapsed time from the beginning of the isotherm until the first nucleus was observed in the otherwise transparent film. The induction time for the Class II particle nucleation was found by extrapolating the linear region (Region II) of the nucleation rate curves across the time axis. The intercept defines the Class II induction time. These induction times are summarized in Table 5.

Table 5

Isothermal Temperature (°C)	Induction Time for Class I Aggregates (Minutes)	Induction Time for Class II Aggregates (Minutes)
160°	25.0	203
175°	11.7	74.7
200°	*	10.2

*Several nuclei were observed prior to obtaining the isothermal temperature.

As would be expected, the induction time decreases as the temperature increases. The presence of induction times for both types of particles and the accompanying temperature dependence is similar to the results observed by Turkevich for the nucleation of gold citrate sols.

The growth rate of individual Class I particles was obtained by measuring the radius of the aggregate as a function of time. The results are shown in Figure 28, which indicates that the aggregates grew linearly in proportion to the square of the radius. Only the linear region of growth is shown. At long times, a plateau is observed indicating the growth has ceased. It was also observed that the rate of growth increased as the isothermal temperature increased. It was not possible to accurately measure the growth rate of

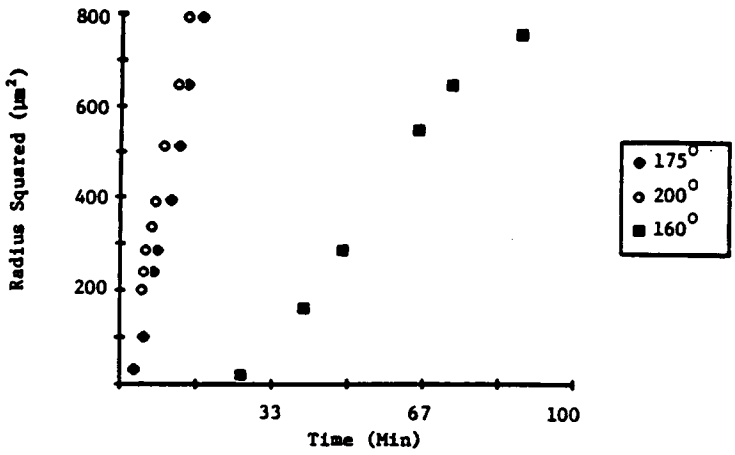

Figure 28. Growth rate of Class I aggregates as a function of time at the given isothermal temperature.

individual Class II particles because of their smaller size and the rapidity with which they grew. The growth rate of all three aggregates is currently under investigation, using video microscopy and signal digitalization.

The nucleation curves of the gold surface aggregates bear a strong resemblance to the results obtained by Turkevich. In both cases, an induction period was observed prior to the onset of nucleation. The gold aggregates exhibited two inductions times: a short one, for the Class I aggregates and a much longer one for the Class II aggregates. Turkevich related the induction time to the conversion of the reducing agent sodium citrate to acetone dicarboxylate. However, an analog to this reaction in these films cannot be suggested at this time.

The sigmoidal shaped nucleation curve shown in Figure 27 is also quite similar to the results of Turkevich. The sharp increase in nucleation rate at the crossover point was similar to the autocatalytic nature of gold nucleation described by Turkevich. In addition, a linear region in the curve was observed and the data could be fitted to a straight line by Equation 4-6. Unfortunately, the tremendous nucleation rate resulted in only 3 to 4 data points in the linear region, not enough to conclude that a unimolecular event was involved in the nucleation process.

4.2.3 COLLOID FORMATION

The size of some of the gold particles shown in Section 4.2.1 and the shape of the nucleation curve in Section 4.2.2 suggested that colloidal gold formed during the thermal treatment. The evolution of gold colloid during thermal treatment was investigated by UV/Vis spectroscopy. The UV/Vis experiment was performed by placing modified gold films in the sample side and unmodified films in the reference side of a Perkin-Elmer 330 dual beam UV/Vis spectrometer. Therefore, spectral events observed were due to the chloroauric acid or its reaction products. Initial results indicated that the gold concentration typically used in these films was too high to get adequate energy throughput. Therefore, considerably less concentrated films (1.0×10^{-3} g $HAuCl_4 \cdot H_2O$/g of polymer repeat unit) were used. Obviously, the difference in concentration between the films typically studied, and the specimens used in the UV/Vis experiment must be considered. The polymer films were thermally treated for 0.5 hr at 80°C, and results obtained for individual films heated an additional hour at 100°C, 100 and 200°C and 100, 200 and 300°C.

Figure 29 summarizes the formation of colloidal gold in XU 218. The flat baseline of the 100°C cured film indicated that no colloid was formed at this time and temperature. Additional heating at 200°C and 300°C promoted the formation

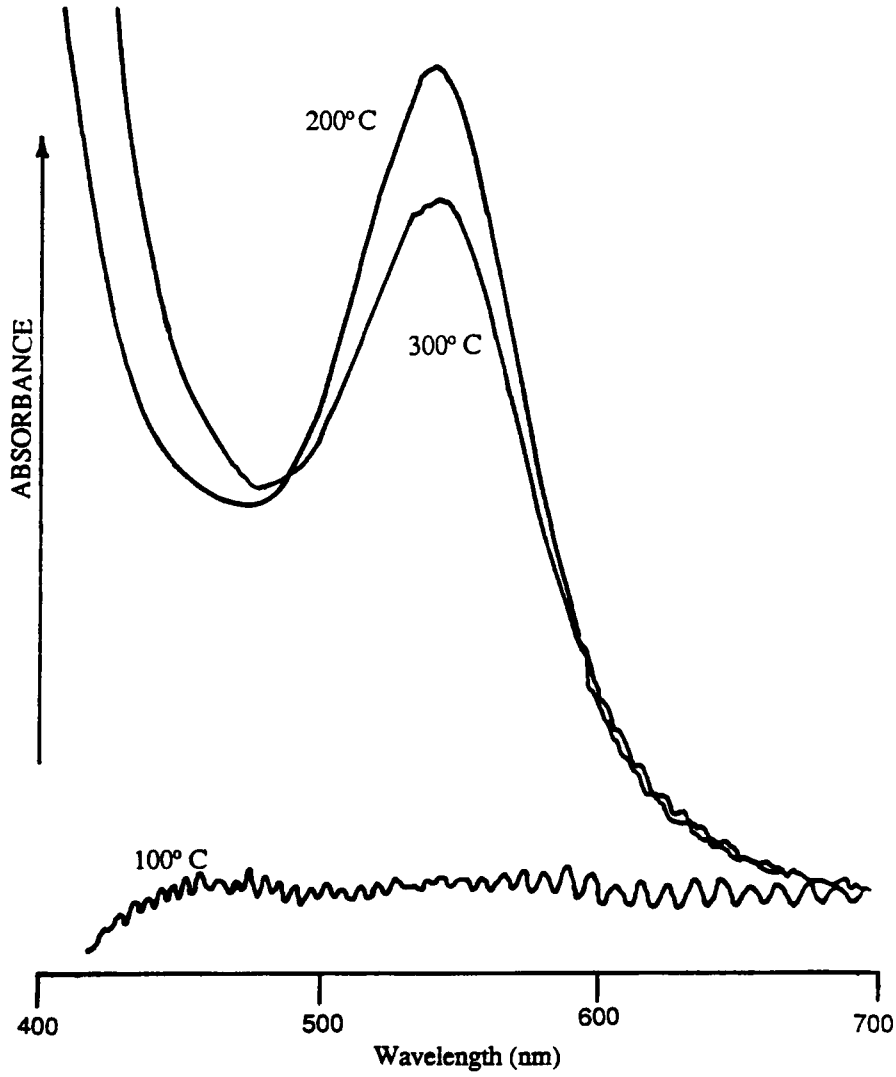

Figure 29. Visible spectra of modified XU 218 film subjected to different thermal treatments.

of colloid as indicated by the maximum at 550 nm.

In the case of the BTDA-ODA metalizing film, colloidal gold was indicated by maxima at 560 nm in the 200°C film and 575nm in the 300°C film (Figure 30). However, there is also evidence that colloidal gold was formed in the 100°C film, as indicated by the maximum at 530 nm. At this point, it is unclear whether the observance of colloid at lower temperatures can be related to surface metalization. The waveform observed in some of the spectra is believed to be due to an interference pattern set-up between the surfaces of the film. The appearance of maxima in the absorbtion spectra indicated that colloidal gold was formed during thermal treatment. Therefore, the appropriate chemistry is present in the modified polymer film to produce colloidal gold.

Extrapolation of these results to polyimide films modified at the typical concentrations must be done with care. It should be noted that the colloid particles observed by SEM and STEM, were obtained from samples modified at the level of one-half millimole of gold per millimole of polymer repeat unit. The UV/Vis samples were approximately 1,000 times less concentrated in chloroauric acid.

As discussed in the Introduction, the average particle size depended upon the concentration of the growth medium by

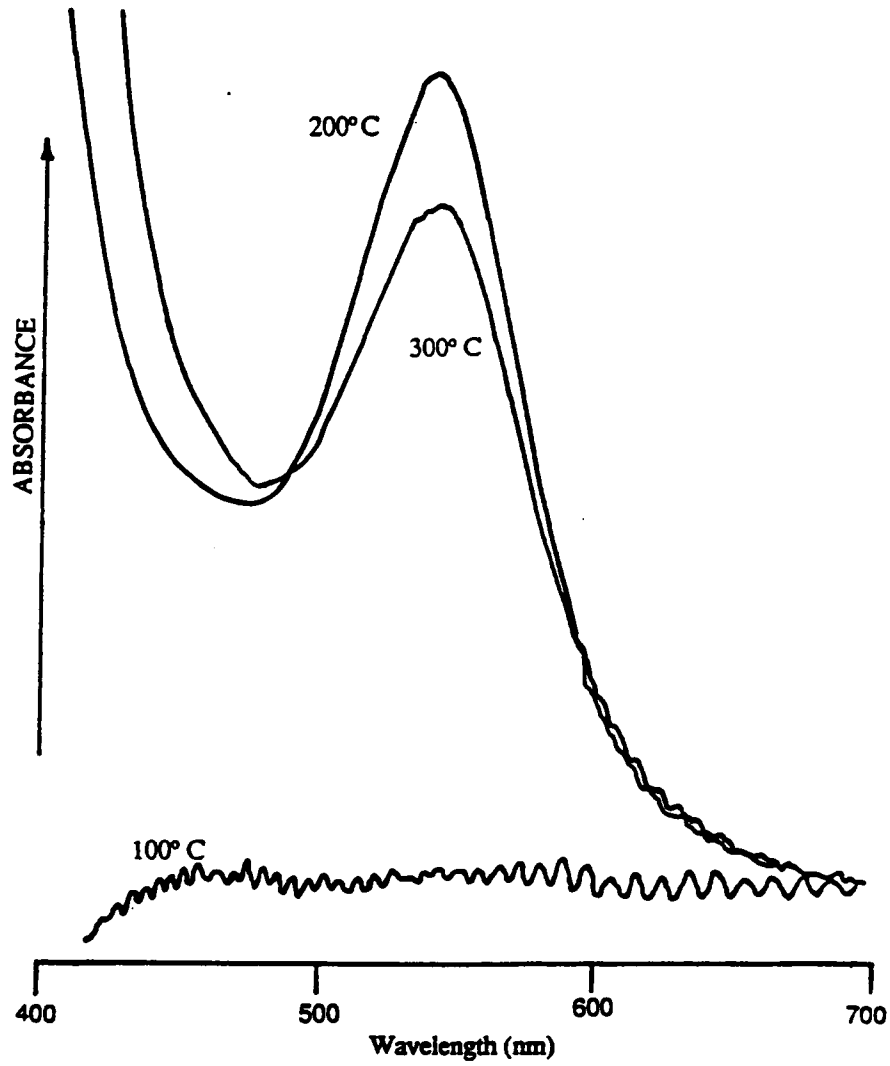

Figure 30. Visible spectral of modified BTDA-ODA film subjected to different thermal treatments.

Equation 4.7. Therefore, the particle size of the colloidal gold formed in UV/Vis samples was expected to be smaller than the particles observed in the standard films. The most important information obtained by these spectra was that colloidal gold was found in the 100°C BTDA-ODA film and that higher temperatures had to be used to produce colloid in the XU 218 film. The presence of colloidal gold will be discussed further in Chapter 5.

4.2.4. IMIDIZATION

In section 4.2.1, it was noted that the imidization reaction did not seem to influence the ultimate distribution of gold particles in the bulk metalizing films. The polyamic acid and imidized versions of BTDA-DAPI resulted in films of similar appearance. However, the bimodal distribution of aggregates in the surface metalizing film suggested that imidization may influence the surface metalization process. The relationship between metalization and imidization was explored by relating the optical microscopic observations to the extent of imidization, as determined by thermogravimetric analysis (TGA).

The temperature necessary to effect cyclodehydration for production of aromatic polyimides is often cited as 165°C [28]. Since nucleation and growth were studied between 160°C and 200°C, it was reasonable to assume that

the metalization process may be related to the imidization reaction. In order to study the physical changes in the polymer which occurred during the heat treatment, unmodified polyamic acid films were prepared at a thickness of 0.5 mm, by casting a solution of unmodified BTDA-ODA polyamic acid onto a glass plate. The solution was dried 0.5 h. at 80°C and 1 h. at 100°C. The change in the mechanical properties of this film which occurred during imidization were then monitored using a Polymer Labs dynamic mechanical thermal analyzer (DMTA). The film was secured in the analyzer head using a single cantilever geometry and heated at 5°C/min from 50°C to 300°C. The information obtained was storage modulus (E') and tan δ as a function of temperature at one hertz of vibrational frequency. A plot of these quantities for unmodified BTDA-ODA is shown in Figure 31. The maximum in tan δ at 93°C probably corresponded to the glass transition temperature of the polyamic acid. At the Tg of the polyamic acid a decrease in E' was observed. As the temperature was allowed to increase, however, there was a subsequent increase in the storage modulus between 160°C and 225°C. The increase in log E' was probably associated with the cure of the polyimide. Conversion of the polyamic acid to polyimide resulted in a stiffer polymer and accounted for the increase in modulus in this region.

The increase in modulus caused by stiffening of the

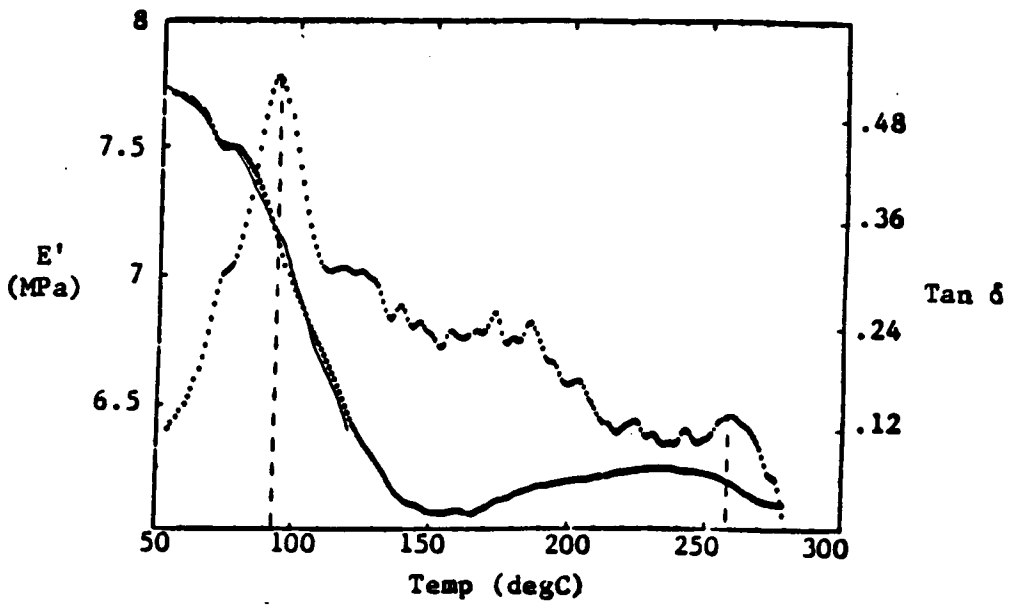

Figure 31. Dynamic Mechanical Thermal Analysis of an unmodified BTDA-ODA polyamic acid film. solid line represents the storage modulus and the dashed line represents tan δ.

polymer matrix may have a profound effect on diffusion controlled processes in the modified polymer. In order to ascertain the extent of imidization at isothermal temperatures, thermogravimetry of unmodified polyamic acid was performed. Small samples of the polyamic acid (ca. 10 mg) free of residual solvent were loaded into the TGA balance and heated under nitrogen for one hour at 100°C. The sample was then ramped at 40°C/min to one of the three isothermal temperatures studied previously during the hot stage optical microscopy experiments. The weight loss indicated during the TGA experiment could then be related to the degree of imidization by assuming all weight loss was due to the liberation of water during the cyclodehydration reaction. The isothermal weight loss at 160°, 175° and 200°C is shown in Figure 32. The y-axis indicates the percentage of sample weight loss. The plateau regions of each weight loss curve corresponded to the one hour isothermal treatment at 100°C. It is interesting that very little cyclodehydration occurred at this temperature. A similar conclusion can also be made from the IR results of Chapter 3. Weight loss, on the other hand, occurred very quickly as each polyamic acid sample was ramped from 100°C to the indicated isotherm. Loss of water at the isotherm appeared to follow an exponential decay. Comparing the induction times listed in Table 5 (from Figure 27) to the

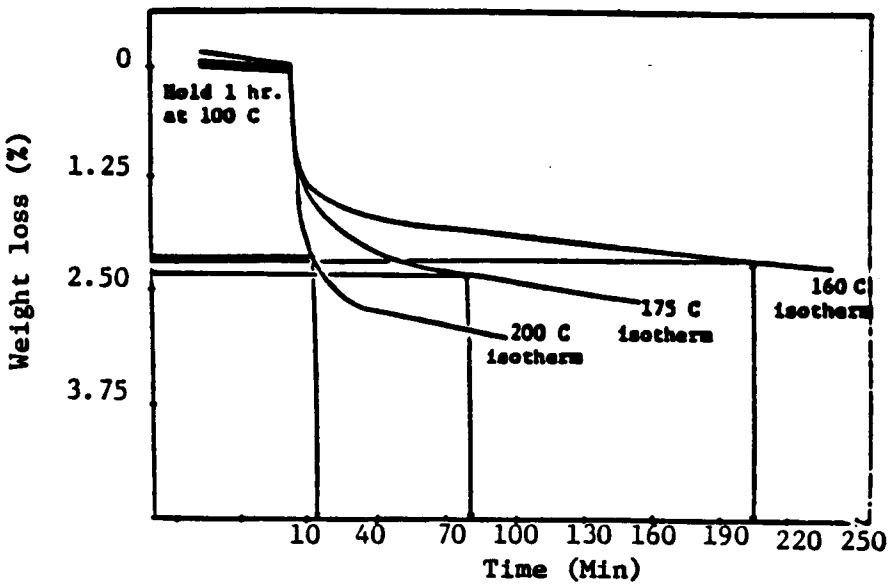

Figure 32. Thermal gravimetric analysis of unmodified BTDA-ODA polyamic acid film.

extent of imidization at the same time (from Figure 32) indicated that regardless of the temperature of the isotherm, the degree of imidization was the same when Class II particle nucleation started (Table 6).

Table 6

Isothermal Temperature (°C)	Relative Percent Imidization at Start of Class II Aggregation
160°	29% ± 2%
175°	31% ± 3%
200°	29% ± 2%

The preceding results suggested that a "critical" degree of imidization is necessary for the onset of the Class II particle nucleation. One explanation for this phenomenon considers the fate of both the colloid and polymer during thermal treatment. The UV/Vis and TGA data suggested that after the 100°C heat treatment, the transparent, modified BTDA-ODA film is still primarily polyamic acid; yet, it contains some colloidal gold. The Tg of the unmodified polyamic acid was found to be 93°C. Heating the film at the isothermal temperatures situated the colloid particles in a polymer matrix 60° to 100°C above its Tg. Presumably, gold migrated easily in this "rubbery" matrix, diffused to the growth centers and formed the Class I structures as the sample was heated. However, coincident

with this process is the imidization reaction, which increased the modulus of the film, the viscosity of the polymer matrix and the glass transition temperature of the polymer. The increase in modulus as a function of polyamic acid "cure" is analogous to vitrification in thermoset polymers [29]. In the case discussed here, vitrification occurred when the Tg of the polymer was equal to or surpassed the isotherm temperature. The corresponding increase in modulus retarded the migration of the gold. When the "critical" imidization value was obtained it was thought that the locus of particle aggregation changed. The colloidal particles no longer migrated the relatively long distance necessary to populate the large Class I aggregates. Rather, short distance local migration was preferred and gave rise to the Class II aggregates. In the next chapter, the relationship between the growth environment of the aggregates and the metalization process will be discussed.

CHAPTER FIVE

THE PROPOSED MECHANISM OF GOLD AGGREGATION IN POLYIMIDE FILMS MODIFIED WITH GOLD

5.1 INTRODUCTION

Scientists throughout the centuries have sought to relate observations to theories by the use of mathematics. However, the complicated shapes and apparent asymmetry of many natural objects seemed to defy description by Euclidian geometry. Over the past decade, the pioneering work of Benoit Mandlebrot has given new life to the mathematical description of disordered systems [30]. As a result, there has been a great deal of interest in the relationship between the growth of disordered objects and their resulting form.

Mandelbrot coined the term "fractal" to describe a type of geometry which could be used to describe disordered objects. One of the powerful features of fractal growth and geometry is the ability to describe a wide variety of observations without making reference to the details of the chemistry or physics which underlie the growth process. The ubiquitous nature of fractal objects is demonstrated by their tremendous range in size. Indeed, coastlines [31] and riverbeds [32] on the one hand are thought to be fractal; whereas, small scale objects, such as the

coalesence of colloids [33-35] and the electrolytic deposition of metals [35], have been shown experimentally to be fractal objects. While the growth of many other objects can be describe as fractal, it is interesting to note that all of the structures mentioned above are thought to grow by the aggregation of smaller subunits. Indeed, in this work, polyimide surface metalization by the formation of gold aggregates is believed to be governed by the same rules used in models of fractal growth.

Before describing the features of fractals, it is useful to consider some aspects of Euclidian (non-fractal) objects. In general, the mass of a Euclidian object will scale with a characteristic length of the object, to an exponent D:

$$\text{Mass} \approx \text{length}^{D} \qquad 5\text{-}1$$

where D is simply the dimensionality of the object. For example, consider a one dimensional rod of length r. If the length of the rod is tripled, then the mass of the rod would also triple, as D = 1. If the radius of a two dimensional disk is tripled, then the mass of the object would increase ninefold, as D = 2. Similarly, tripling the

radius of a sphere will increase the mass twenty-seven times, as the dimensionality is equal to 3.

One characteristic of fractal objects is that the dimensionality is not necessarily an integer number. For instance, the object shown in Figure 33 is a fractal object with a dimensionality of 1.71 [36]. As will be discussed, this diffusion limited aggregate (DLA) is embedded in a two dimensional lattice (D=2). The power law behavior of fractals is similar to that observed in critical phenomena. Indeed, fractal geometry has been used to describe phase transitions near critical points.

One of the ways of characterizing fractals is to determine their dimensionality by measuring the scaling properties between mass and length. This can be done by measuring the radius of gyration, Rg, as a function of mass [37]. Alternatively, the two point density-density correlation function, C(r), can be plotted as a function of radius [38].

The scaling relationship between mass and radius in a fractal object is illustrated in Figures 34 and 35 [39]. Figure 34 is an illustration by T. Viscek of a fractal at three different stages of growth, when the radius is equal to 1, 3 and 9. It can readily be observed that the r=9 structure is made up of five of the r=3 structures. Similarly, the r=3 structure is comprised of 5 of the r=1

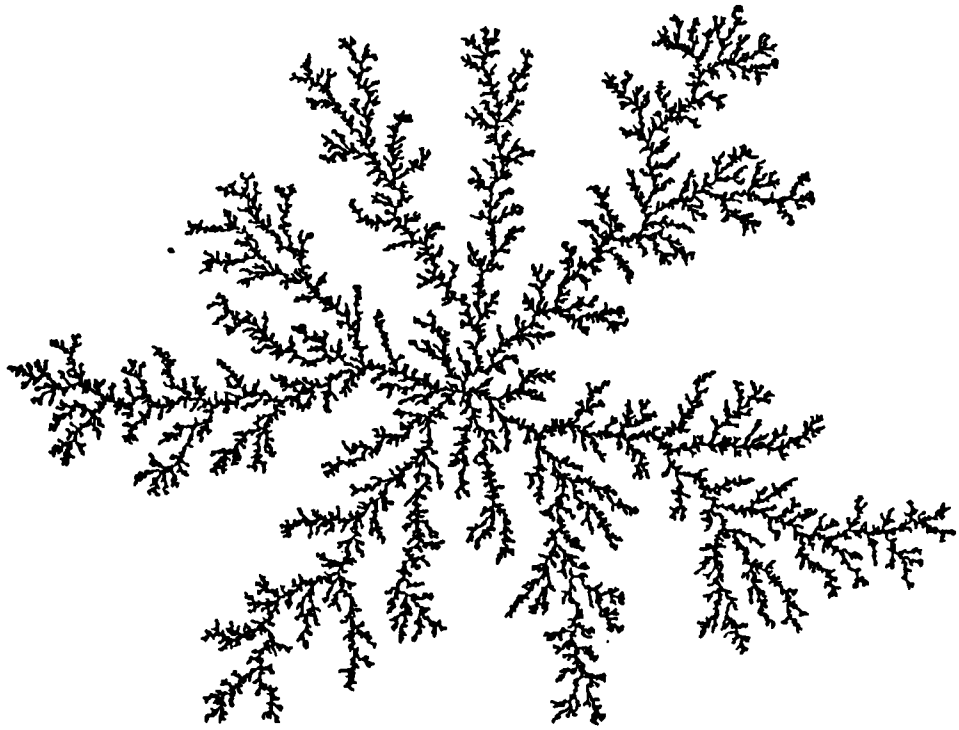

Figure 33. Witten-Sander diffusion limited aggregate (from Reference 36).

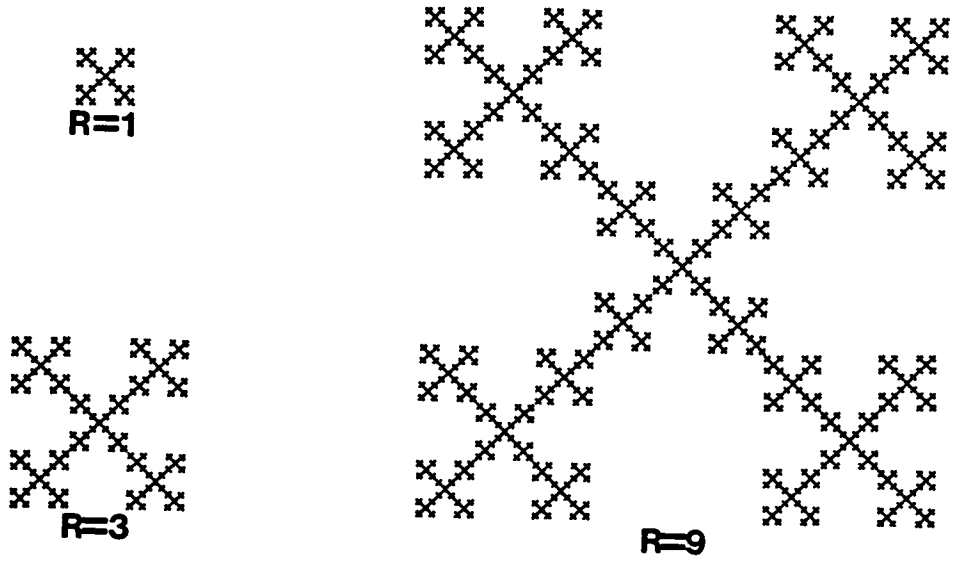

Figure 34. Model fractal at three stages of "growth". A) Radius = 1; B) Radius = 3; C) Radius = 9 (from Reference 39).

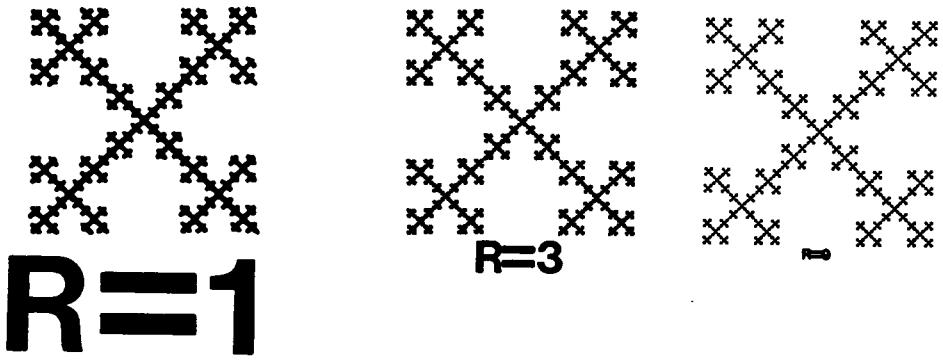

Figure 35. Magnification of the R = 1 and reduction of the R = 9 fractals from Figure 2 illustrates the concept of self-similarity (from Reference 39).

units. In the previous discussion of Euclidian objects, it was shown that the mass of a two dimensional object increased ninefold when the radius was tripled. However, in the case of the object in Figure 34, tripling the radius only increases the mass (as determined by the quantity of the ink used to draw the figure) by a factor of five. Therefore, the fractal dimension must be non-integer and lie somewhere between D=1 (where the mass increases threefold) and D=2 (where the mass increases ninefold). The actual value of D for this particular fractal is 1.46. The greater the portion of the two dimensional lattice covered by the fractal, the closer the value of D will be to that of the embedding lattice (D=2).

Figures 34 and 35 can also be used to demonstrate self similarity, an additional feature of fractal objects. Self similarity is a symmetry property of fractals; that is, the object is symmetric (appears the same) under the operation of dilation or reduction. An exact fractal always looks the same, even when changing the scale on which the observation is made. If the r=1 object is magnified three times it looks exactly like the r=3 object, as is shown in Figure 35. Similarly, if the r=9 figure is reduced threefold, then it appears identical to the r=3 object. The DLA shown in Figure 33 is self similar in a statistical sense. That is, similar objects are obtained under the operation of

dilation or reduction.

Fractal objects also show a decrease in density as the radius increases, as is shown in Figure 36 [39]. This phenomenon is in contrast to amorphous and crystalline materials which reach a constant value of density as a function of distance.

The preceding criteria can then be used to identify the form of an object and determine if it is fractal. However, much of the work done in this area has centered about computer simulations of shapes and growth.

One of the earliest models adopted by physicists to describe growth is the Eden model [40]. Several versions of this model have been studied, but the simplest one starts by randomly occupying a site on a two dimensional lattice with a seed particle. The nearest neighbor lattice sites are identified as growth sites, one of which will be occupied with a probability proportional to the number of available growth sites. Addition of the second particle increases the number of nearest neighbor sites at the periphery of the cluster. As subsequent particles are added at the peripheral growth sites, a compact cluster is generated as is shown in Figure 37A. The compactness of the Eden cluster is shown by noting the order in which lattice sites were occupied as a function of time, as is shown in Figure 37B.

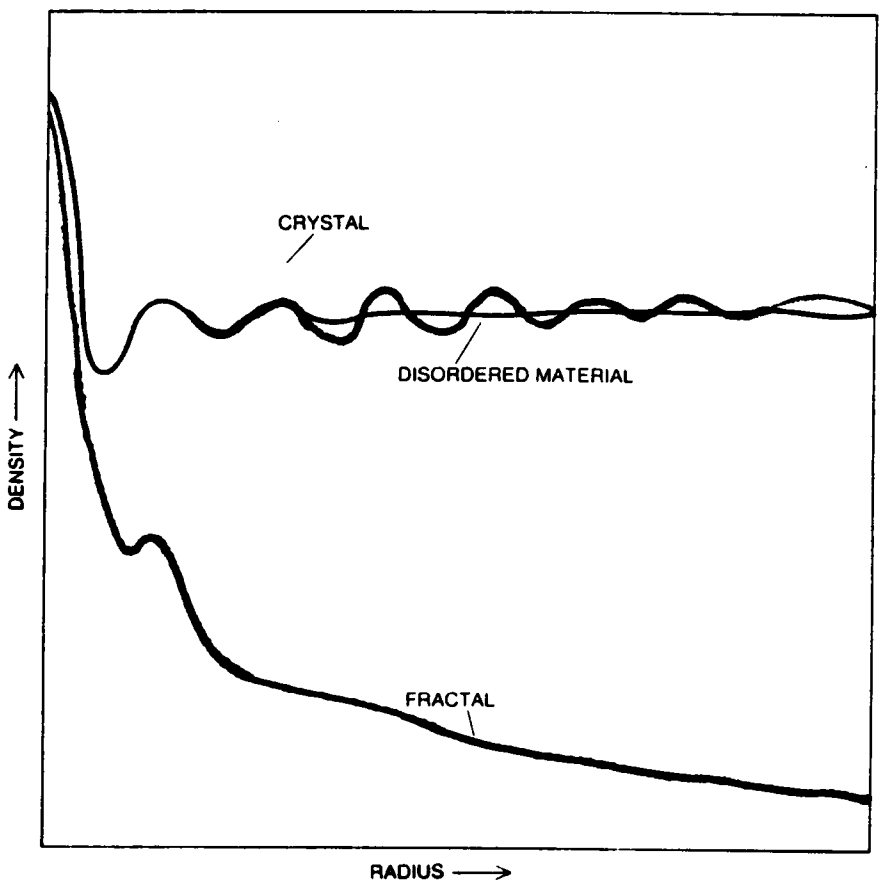

Figure 36. The density of an object as a function of radius is displayed for an amorphous solid, crystal and fractal (from Reference 39).

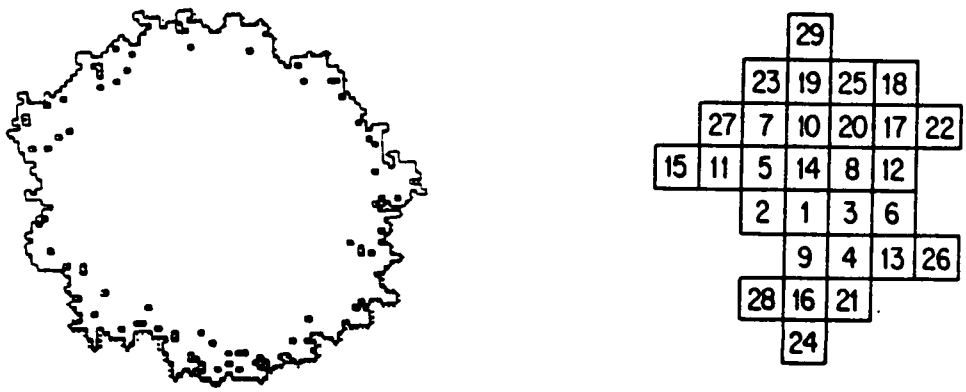

Figure 37. Eden clusters. A) Computer generated model; B) Following the occupation of lattice sites as a function of time illustrates the uniformity of growth (from Reference 40).

A more recent two dimensional model used to describe aggregation was developed by Witten and Sander in 1981 [38]. In their diffusion limited aggregation (DLA) model, fractal structures were generated by allowing a stationary seed particle to occupy a site on a two dimensional lattice, as is shown in Figure 38. A second particle is then randomly introduced onto the lattice at a distant site and translated by a series of random walks. This process is described as a non-local diffusion field. When the mobile particle reaches a site adjacent to the seed particle, it "sticks" to the seed and becomes part of a growing cluster. Repetition of this process leads to the highly ramified DLA structure, shown previously in Figure 33. This process develops a fractal object with a dimensionality of 1.71, embedded in the two dimensional lattice. The DLA cluster has also been generated using a three dimensional lattice [41].

A generalized model of Witten-Sander DLA has also been studied [42]. In this approach, a particle adding to the growing cluster does not stick in an irreversible manner. Rather, the randomly walking particle sticks with a probability, s. The value of s was related to the number of filled nearest neighbor sites B, by

$$s = t^{3-B} \qquad 5\text{-}2$$

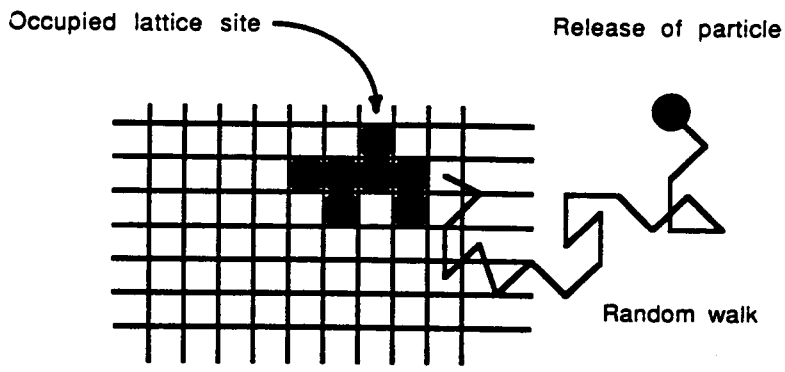

Figure 38. Lattice model of diffusion limited growth.

where t is an adjustable parameter (O<t<1) which controls the shape of the aggregate and B = 3, 2 or 1 on a square lattice. From this relation, it is obvious that a walker is more likely to occupy a hole (B=3) than a point (B=1). Witten and Sander observed that a sticking probability s=1 generates the standard DLA cluster; decreasing the value of s thickens the dendritic branches. Banavar, et. al [43], used this technique to study the evolution of the DLA pattern as the sticking probability was varied. They observed that the ramified cluster which formed when t=1 (in the Witten-Sander notation) gave way to thickened clusters when t was decreased to 0.4 or 0.2, as shown in Figure 39. At a value of t=0.05 the structure was completely compact. The generalized DLA model generates the Witten-Sander cluster in the limiting case of irreversible sticking and the Eden cluster in the limiting case of no sticking.

DLA type growth is not usually observed in nature since other phenomena (such as surface tension) tend to smooth out the aggregates and form more compact structures. Indeed, DLA growth corresponds to zero surface tension growth; whereas, Eden clusters correspond to high surface tension growth. Therefore, the adjustable parameter t, which controlled the shape of morphology in Figure 39, mimics the effect of surface tension in the simulation.

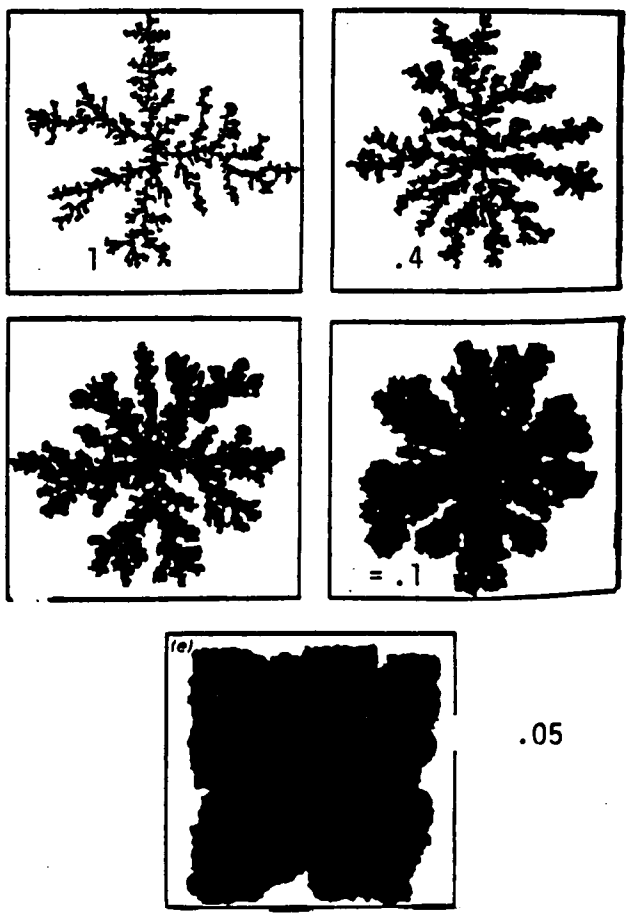

Figure 39. Evolution of DLA structure in radial geometry as sticking probability is decreased from t=1 to t=0.05 (from Reference 43).

Relating the aggregate shape to surface tension was done to emulate the description of growth instability developed by Mullins and Sekerka [44]. In their model, the Gibbs-Thompson (Kelvin) equation is used as a boundary condition. In its simplest form, the Gibbs-Thompson equation can be written as:

$$\Delta\mu = -2\gamma\Omega/r \qquad 5\text{-}3$$

where μ is the chemical potential, γ is the surface tension, Ω is the atomic volume and r is the radius of the particle. The Gibbs-Thompson equation can also be used to predict the increased solubility and lower melting temperature of small particles, which are of great interest in the subsequent discussion

All three of the models described possess polar geometry. Similar modeling can also be done in rectangular geometry starting with seed particles that lie along a straight line boundary. The simulation is then performed employing the generalized DLA model outlined previously; (i.e., non-local diffusion of random walkers and incorporation of a sticking probability) [43]. Figure 40 shows the results of such a simulation. Viscous fingers grew outward from the boundary, and these fingers thickened as the sticking probability was decreased via the adjustable parameter, t. Similar results were also

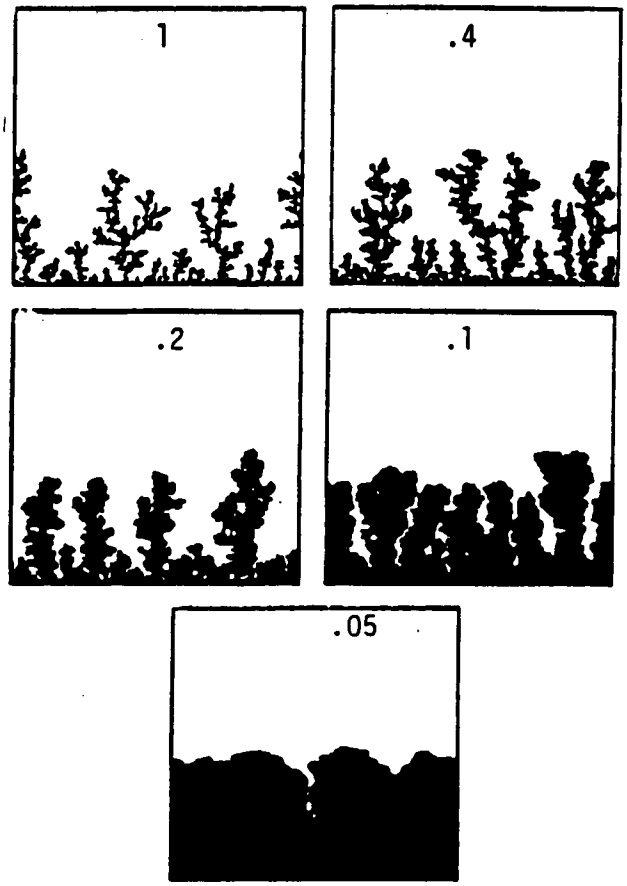

Figure 40. Evolution of DLA structure in rectangular geometry as sticking probability is decreased from t=1 to t=0.05 (from Reference 43).

obtained by Vicsek, who related the sticking probability to the local surface curvature (a macroscopic rule) which allowed the attached particle to assume the lowest potential energy site among the nearest or next-nearest neighbor lattice site (a microscopic rule) [45]. Therefore, the generalized DLA model gives rise to clusters or viscous fingers. The growth rules are the same in both cases; only the location of the seed particles in the lattice is changed.

In addition to the models outlined above, the dense branch morphology (DBM) has also received considerable interest in the recent literature. In the work of Ben-Jacob et. al., [46] non-fractal objects were obtained experimentally, and the morphology of the aggregate could be related to a number of control parameters. In addition, very recent work of Suresh [47] showed that DBM and Eden clusters are obtained during the phase separation of a lipid monolayer near the critical point, as shown in Figure 41. Stanley, et. al., [48] related the Suresh clusters to the gold aggregates discussed in this work via a two parameter equation. The Stanley model will be discussed in greater detail in the Results and Discussion section.

If there is sufficient fluctuation in electron density between an object and the embedding space, and the distance between these fluctuations are colloidal in size, then the

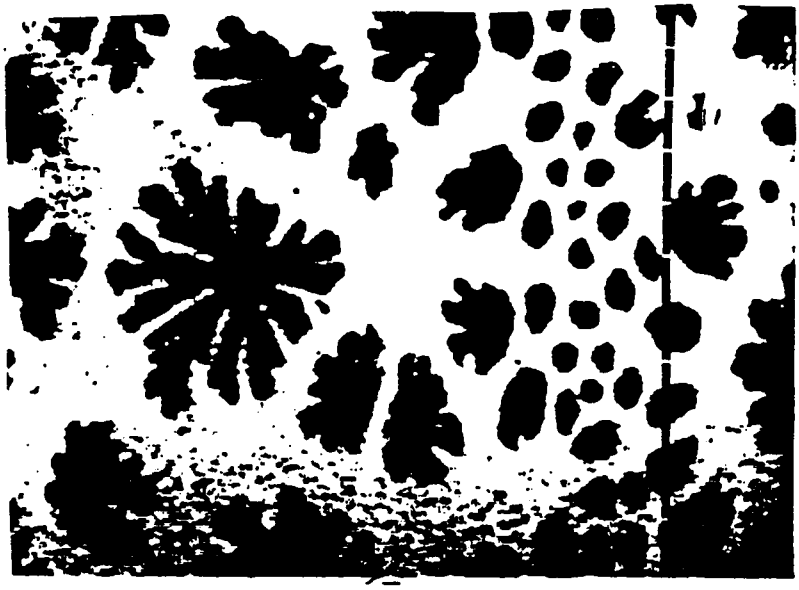

Figure 41. Condensed phase of lipid monolayer (from Reference 47).

shape of fractal and non-fractal objects may be studied by small angle X-ray scattering (SAXS). With this technique it is also possible to calculate the radius of gyration (Rg) of the particles. SAXS is useful in the study of these metal containing polymers because it has been shown previously that colloidal gold is formed in the early stages of thermal treatment. While the aggregates observed on the glass side surface are much too large to be studied by this small angle technique, it is possible to obtain some information concerning the formation, size and shape of colloidal particles. Because of differences in nomenclature used by the various experts in the field of SAXS, it is useful to present some background into this scattering technique.

The relationship between the scattered waves and the distance between scattering elements is governed by the Bragg equation:

$$n\lambda = d \sin 2\theta \qquad 5\text{-}4$$

where n an integer number (the order of the maximum), λ is the wavelength of radiation, d is the distance between scattering elements, and θ is the angle between the incident ray and the angle of observation. Typically, the X-rays are obtained from a copper anode (CuK_α = 1.54

angstroms). The Bragg relationship is quite useful in illustrating the reciprocal nature between θ and d. For example, wide angle X-ray scattering (WAXS) is used to study the spacing between crystallographic planes; whereas, SAXS is used to probe larger features.

Figure 42 is a schematic representation of X-ray scattering from an amorphous material [49]. The intensity I(K) of the scattered beam is plotted versus K, a measure of the scattering angle ($K = 2\pi \sin 2\theta/\lambda$). The scattering curve is broken down into four regions and each region contains information about the system under consideration. In the limiting region, where I(K) approaches zero, I(K) is proportional to the number density of scatterers. As expected by the Bragg equation, smaller features of the system are probed as the scattering angle becomes larger. In the Guinier regime, the actual dimensions of the scattering elements can be measured through the radius of gyration, Rg. Typically, colloids (30 - 1000 Å) and microvoids account for the scattering in the Guinier regime. At even greater angles, the surface of scattering elements account for the scattering in the Porod Regime. In this region, information concerning the surface area and shape of the scattering elements can be obtained. In the wide angle or Bragg region, the scale length is near that of the distance between crystallographic planes.

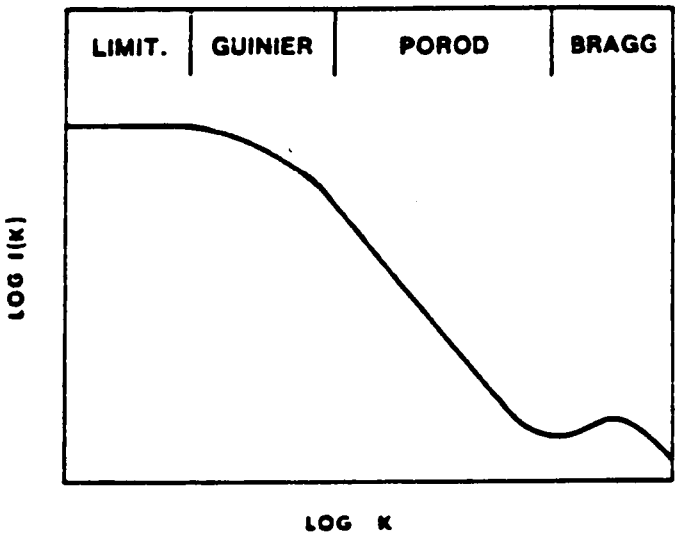

Figure 42. Schematic diagram of X-ray scattering from an amorphous solid (from Reference 49).

Of particular interest in this study is the SAXS scattering which occurs in the Guinier and Porod regimes. As will be discussed in the following paragraphs, in some cases, it is possible to obtain the radius of gyration, Rg from the scattering profile in the Guinier region and information about the surface conformation from the Porod regime.

Figure 43 outlines schematically the general set up of an X-ray scattering experiment [50]. As shown, an X-ray travels in a direction parallel to s_o and impinges on the scattering element (electron) defined at P. The scattering element at O is arbitrarily defined as the coordinate origin for the system under consideration. Secondary rays are emitted in a direction parallel to $\underline{s}$ at a scattering angle of 2θ. The vector $\underline{b}$ is a measure of the scattering angle:

$$\underline{b} = \underline{s} - \underline{s_o} = 2 \sin \theta \qquad 5\text{-}5$$

The distance between the origin and the nth scattering element is given by $\underline{r_n}$. As the secondary (scattered) waves emanate from the points of impingement, they will interfere both constructively and destructively; the degree of interference (and hence the scattered intensity) depends on both the path difference between the scattering elements

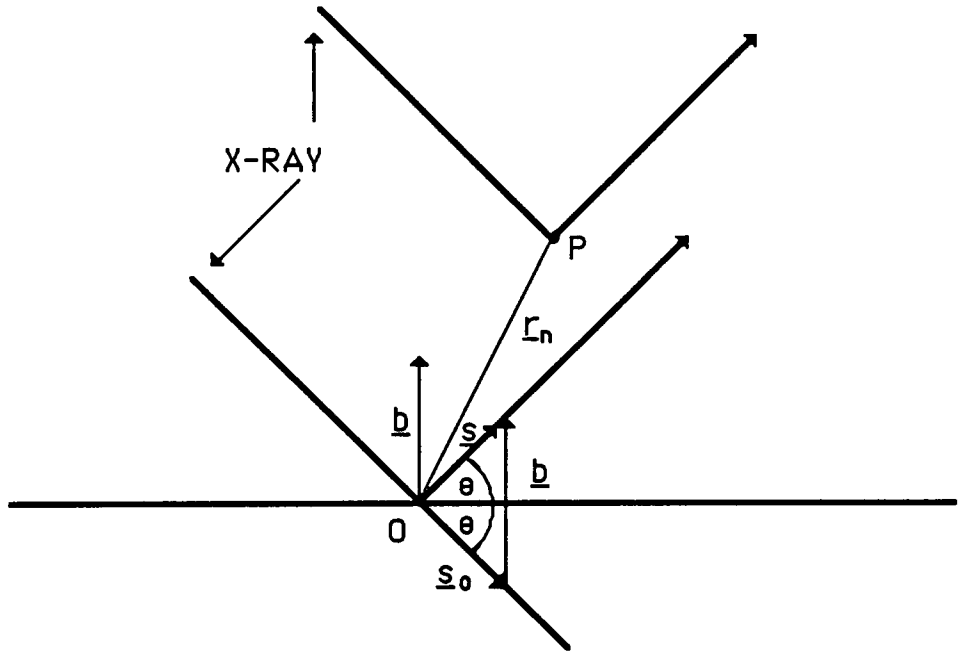

Figure 43. Schematic representation of scattering experiment (from Reference 50).

and the scattering angle θ. In Figure 43, the path difference between the origin and the $\underline{r}_n^{th}$ scattering element can be expressed as $\underline{b} \cdot \underline{r}_n$.

The amplitude A, of the scattered composite wave can then be expressed as:

$$A=\Sigma f_n \exp\{-2\pi i(\underline{b}\cdot\underline{r}_n)\} \qquad 5\text{-}6$$

where f_n is the atomic scattering factor of the nth atom in the assembly. The value of f_n is a dimensionless quantity which accounts for the scattering power of an individual atom at a given value of θ. Squaring the amplitude (multiplying by the complex conjugate) gives the intensity of the scattered wave I(K). In the case of scattering at small angles it can be shown that [49]:

$$I_{\infty} = I_o \exp[-Rg^2K^2/3] \qquad 5\text{-}7$$

where I_o is the intensity of the scattered wave in the forward direction $\theta = 0$ and $K = 4\pi\sin\theta/\lambda$. Taking logarithms of both sides of results in the Guinier equation:

$$\ln I_{\infty} = \ln Io - Rg^2K_2/3 \qquad 5\text{-}8$$

Therefore, the intensity of the forward scattered wave and the radius of gyration can be found by the intercept and the slope of a plot of $I_{\infty}(K)$ versus K^2, respectively. Figure 44 is a schematic representation of the data obtained by the SAXS experiment from a single particle via a Guinier plot [51]. Qualitatively, it can be seen that the larger particles give rise to steeper scattering curves for the same angle Θ, and hence the slope is steeper in the Guinier plot (larger Rg).

The total surface area S, of the interfacial region in a two phase system can be evaluated from Porods Law:

$$I(K) = (\Delta p)^2 \frac{2\pi S}{K^4} \qquad 5\text{-}9$$

where p is the difference in electron density between the two phases (typically the scattering particles and the solvent) [52]. Porods Law indicates that the "tail" region of the scattering curve -using pinhole collimation- will have a slope of -4 for a dilute monodisperse assembly of spheres. The same specimen will have a scope of -3 if slit collimation is used.

While many systems exhibit integer values for the slope in the Porod regime, deviations from these values have been

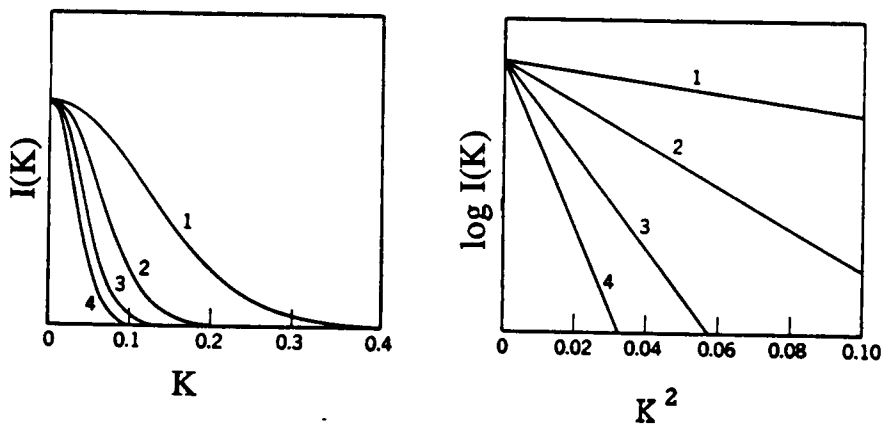

Figure 44. A) Schematic of SAXS data obtained from a single particle. The particle size increases with the indicated numbers. B) Guinier plot of data obtained in 47A (from Reference 51).

explained in terms of the interface of the scattering element. Bale and Schmidt [53] showed that the power law relationship is actually described by:

$$I(K) \approx K^{D_s - 4} \qquad 5\text{-}10$$

where D_s is the surface dimension of the scattering object. The relationship derived by Porod assumed spherical scatterers; therefore $D_s = 2$ and Equation 5-10 agrees with Porods Law. For fractally rough surfaces $2 < D < 3$ and the slope m, is $-3 < m < -4$. Scattering curves with an observed slope less than -4 are thought to arise from diffuse interfaces [54]. Therefore, by evaluating scattering data by the Guinier and Porod equations, it is possible to obtain some insight to the average size and shape of colloidal particles.

The observations presented in this chapter relate to the mechanism of phase separation during thermal treatment and are divided into six sections. The first two sections will present SAXS data of bulk and surface metalizing films, respectively. In the third section, the fate of surface colloidal particles during thermal treatment will be examined and related to the growth of surface aggregates. The growth environment of these aggregates will be explored further in the fourth section and then related to a

thermodynamic model of phase separation in the fifth section. Lastly, the growth of gold surface aggregates will be discussed in light of some solid state models used to describe aggregation.

5.2 RESULTS AND DISCUSSION

5.2.1 SAXS OF MODIFIED FILMS

The structure of modified XU 218 during thermal treatment was evaluated by SAXS. This technique was thought to be quite useful in the study of gold containing films because of the size of the scattering elements and the difference in electron density between the polymer and the gold. Also, the polymers themselves do not exhibit any scattering in the SAXS region which would otherwise complicate the interpretation of the data. Shown in Figure 45 is the log I(K) versus log K plot for a modified XU 218 film heated isothermally at 200°C.

At short times, no scattering is observed in the sample. However, after prolonged heating, there is a pronounced peak in the scattering profile with a maximum at $K = 0.015\ Å^{-1}$. The emergence of this peak as a result of heating suggests that it is due to the formation of colloidal gold. This assessment is consistent with the UV/Vis data of Chapter 4, which also showed evidence for

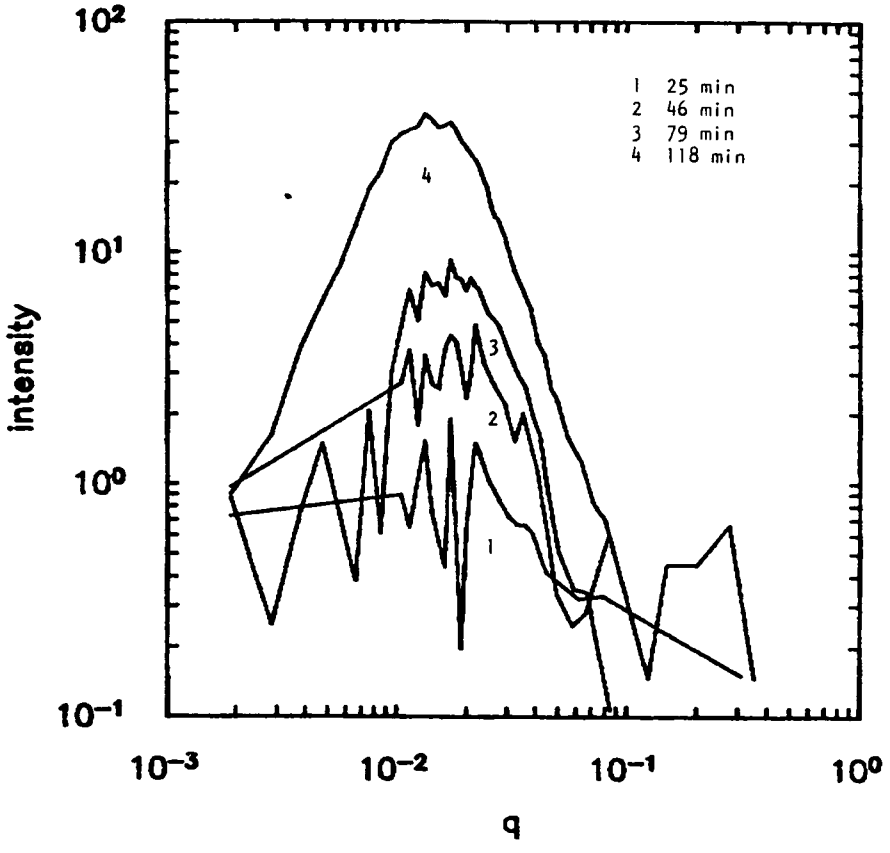

Figure 45. SAXS spectra of XU 218 at 200°C as a function of the indicated time.

colloidal formation in heated XU 218 film.

The presence of a correlation peak in the small angle X-ray scattering is not the type of behavior predicted for the scattering of a single particle or an amorphous material, as discussed in the Introduction. Rather, the correlation peak suggests that the gold has assumed some sort of periodicity in the polymer matrix. If the peak is due to scattering from colloidal gold, then there must be regularity in the spacing of these particles. However, homogeneous nucleation of the colloidal gold would be expected to occur in a random fashion throughout the film. The periodicity of this phase separation event suggests that spinoidal decomposition may be the mechanism which initially occurs in the film.

A plot of the "tail" of the scattering curve in Figure 45 indicates that the slope is -3.6 ± 0.1 . Since slit collimation was used, a value of -3 is predicted by Porods law. A value for the slope greater (more negative) than -3 is associated with a diffuse or "fuzzy" interface in single particle scattering theory [54]. Since single particle scattering has been discounted in the specimen, it is difficult to arrive at an unequivocal conclusion concerning the shape of the colloidal particle. However, it has been suggested that the formation of the colloid gives rise to microscopic depletion zones around the particle [55].

Therefore, the fluctuations in electron density needed to produce scattering is thought to arise from the solute rich (colloidal particles) and solute poor (depletion zones) regions in the film. A diffuse depletion zone surrounding the particle could give rise to slopes greater than -3.

The metalization process in the polyamic acid version of XU 218 was also examined. As indicated previously in Chapter 2, the condensation of BTDA and DAPI resulted in a polyamic acid that had the same chemical composition as XU 218 after thermal imidization. Comparison of the properties of the soluble polyimide XU 218 to the polyamic acid (BTDA-DAPI) allowed for an assessment of the imidization reaction on the ultimate distribution of the metal. It was noted that the films formed from the BTDA-DAPI polyamic acid had the same visual appearance as the modified XU 218 film. Hot stage optical microscopy at 200°C revealed that metalization occurred in the BTDA-DAPI polymer in much the same way as the XU 218 polyimide. Therefore, the imidization reaction (i.e., water release) does not seem to have a profound effect on the ultimate distribution of gold in the film.

The modified BTDA-DAPI was somewhat similar to the modified XU 218 in its scattering behavior, as shown in Figure 46. The intensity of the scattering grew as a function of time at the isotherm, while the peak maxima remained constant at K = 0.015 $Å^{-1}$. The increase in the

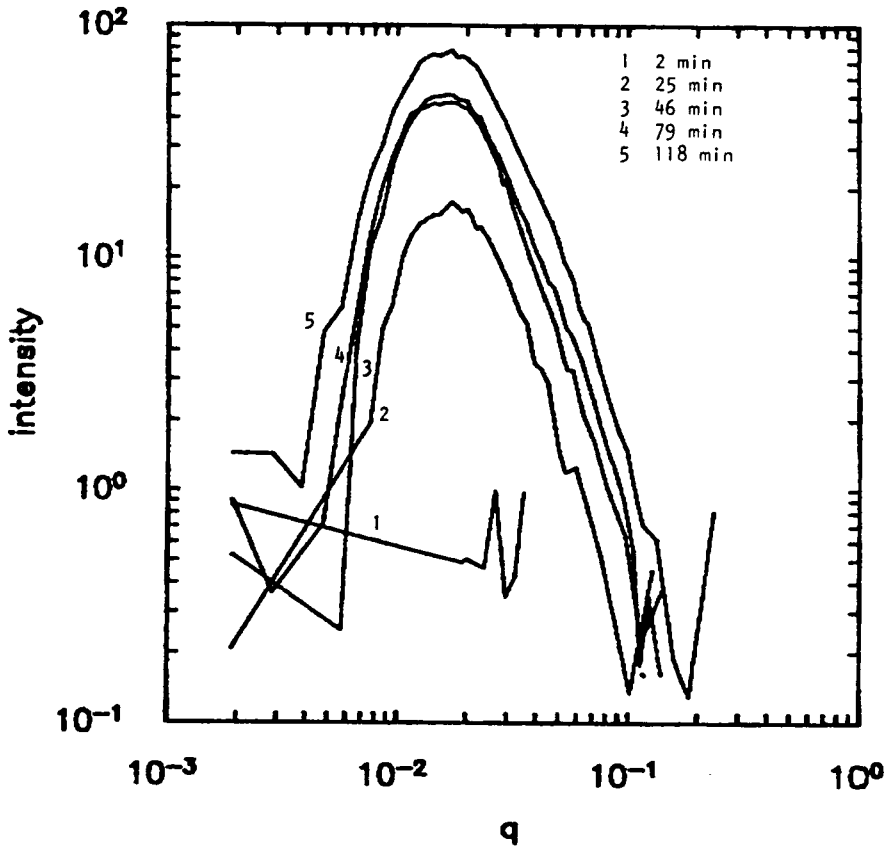

Figure 46. SAXS spectra of BTDA-DAPI at 200°C as a function of the indicated time.

scattering intensity combined with the fixed location of the correlation peak maxima suggests that spinoidal decomposition may also be the initial mechanism of phase separation in the modified BTDA-DAPI film. If the scattering centers remain a constant distance apart and the intensity increases, then it appears as if the wavelength of fluctuation (Figure 16 in Chapter 4) remains constant while the amplitude of the fluctuation increases. The scattered intensity I(K), depends on the electron density difference between the scattering elements and the supporting matrix. This result indicates that either the colloidal particles are "densifying" or the matrix is being depleted of gold. However, the growth occurs without a change in the distance between scattering centers. Therefore, the particles appear to be fixed in their position in the film. If this is the case, then the particles observed in the SAXS experiment cannot participate in the formation of larger structures in the bulk of the film. The final slope of the curve is -3.6 ± 0.1, which was consistent with the value obtained in the modified XU 218 film.

A second polyamic acid derived film, BTDA-DDS, which also showed bulk metalization was evaluated by SAXS, as shown in Figure 47. In this case, the growth of the correlation peak was not as dramatic as in the previously modified film. A peak was observed in the modified film at

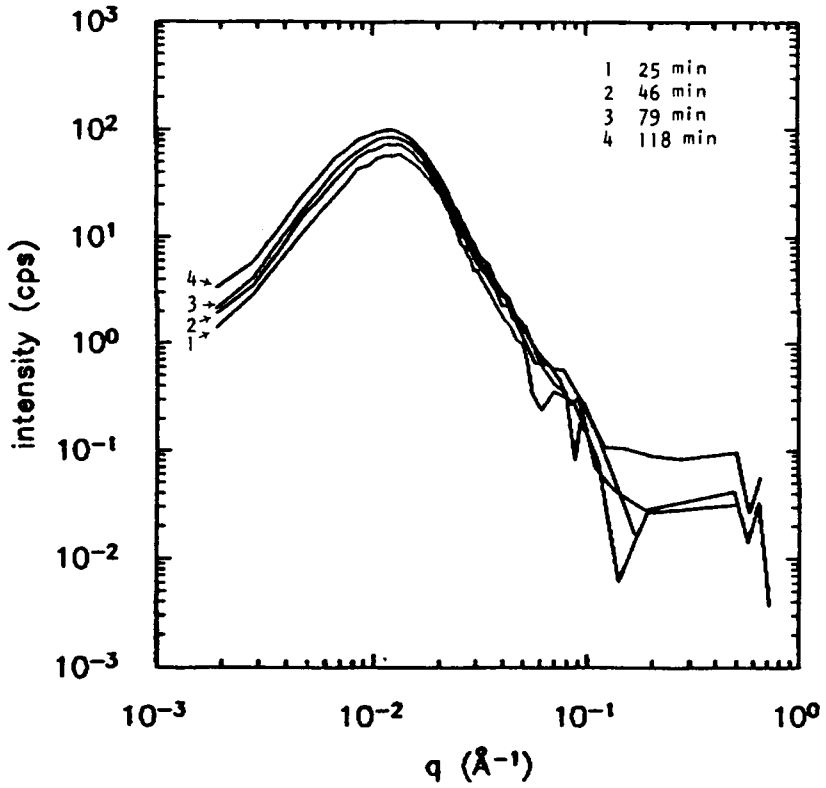

Figure 47. SAXS spectra of BTDA-DDS at 200°C as a function of the indicated time.

$K = 0.015\ A^{-1}$.

As was made evident in Chapter 4, there is a substantial difference between the ultimate distribution of gold in the modified BTDA-ODA polyimide film and the rest of the modified polyimide films studied. However, this difference did not manifest itself in the SAXS data. As shown in Figure 48, a correlation peak was centered at 0.015 A^{-1}. The BTDA-ODA film more closely resembled the BTDA-DDS film in that colloid seemed to form quite early at the isothermal temperature. In the XU 218 and BTDA-DDS film, longer times were needed to develop the correlation peak.

The observations concerning metalization presented in Chapter 4 can now be considered in terms of the SAXS data. The thermal treatment of the film promotes phase separation of the gold from the polymer. Also, there appear to be two different sizes of gold particles formed as observed by optical microscopy as described in Chapter 4. The SAXS data indicate that colloidal gold, separated by a distance of about 100 A. was formed in all of these films. The presence of the colloidal phase was also detected by the color of the film, and the UV/Vis results of Chapter 4. The periodicity observed in the SAX data, along with the value of the slope in the Porod region, suggest that spinoidal decomposition may be the inital mechanism of phase separation that gives rise to the colloidal phase. In addition to the colloidal

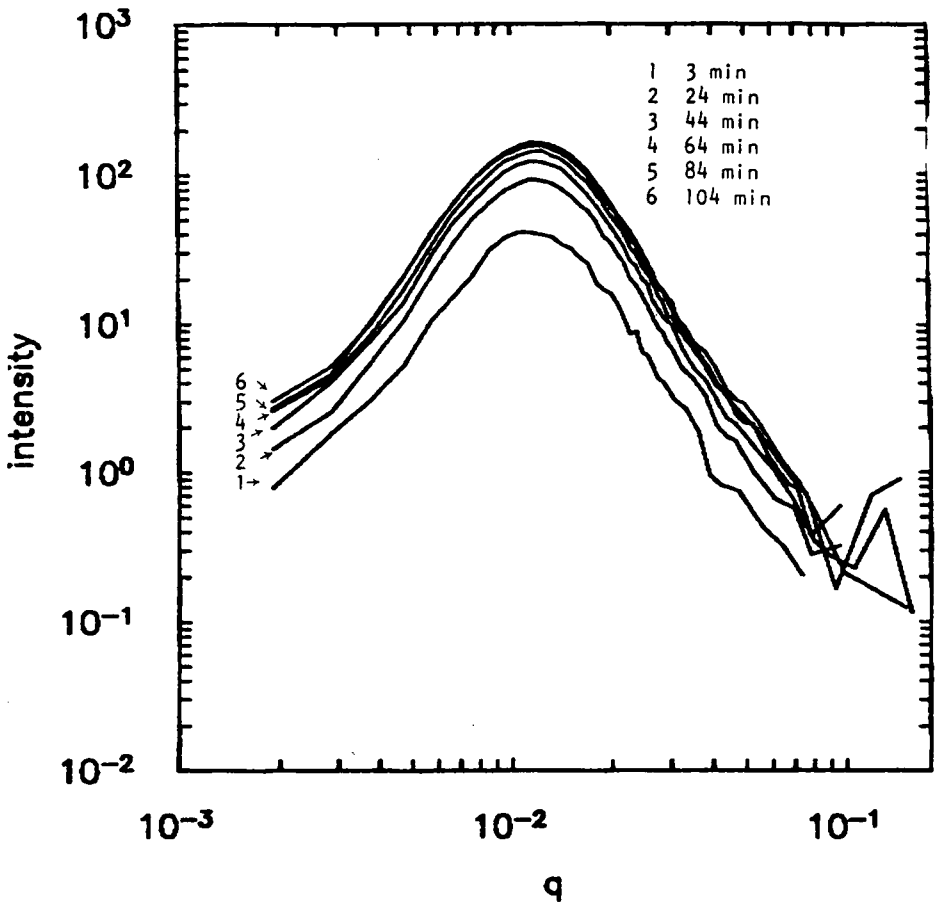

Figure 48. SAXS spectra of BTDA-ODA at 200°C as a function of the indicated time.

particles, there were also particles approximately 5 μm in diameter which populated the interior of the bulk metalizing films and large gold aggregates on the surface of the BTDA-ODA film. The growth of these larger particles does not seem to be related to the colloidal gold material, as indicated by the invariance of the SAXS correlation peak. In the next section on surface metalization, a thermodynamic approach to phase separation will be considered. At this point though, it is useful to consider a possible "physical" model of the driving force for the phase separation in the bulk film, without regard to the mechanism of phase separation (spinoidal decomposition versus nucleation and growth) or even the size or shape of the particles formed.

In their idealized initial state, the modified films are thought to be solid state solutions of the polymer and dopant. This state corresponds to the 100°C modified XU-218 film, but may occur at lower temperatures in the condensation polymers. In any case, heating the film to 200°C promotes the decomposition of the dopant to its products: metallic gold, HCl, Cl_2 and H_2O (see the Appendix). During this reaction, very small gold particles -perhaps even atomic gold- are formed in the polymer matrix. This arrangement of matter is similar to a supercooled liquid and it is useful to think of the "atomic" gold in these films existing in a liquid-like or disordered state

nearly 1000°C below the freezing point of the metal. In this situation, there would be a tremendous driving force for condensation and/or crystallization of the metallic phase. However, the formation of colloidal gold and the larger bulk gold particles may arise by different mechanisms of phase separation. Colloidal gold may form by spinoidal decomposition, whereas aggregates form by nulcleation.

5.2.2 FATE OF SURFACE COLLOID PARTICLES IN BTDA-ODA

Heating the modified BTDA-ODA film resulted in behavior not seen in the bulk metalizing films; that is, the formation of colloidal particles (0.16 μm in diameter) on the atmosphere side surface of the film. A SEM of these particles in a fully cured film was shown previously in Figure 20. It should be stressed that these surface colloidal particles are larger than the structures identified by SAXS and therefore are not responsible for the SAXS scattering. In order to evaluate the formation of these surface colloid particles, thermally treated films (100°C) were heated for short periods of time at elevated temperature (ca. 200°C) in the hot stage microscope. In this way, it was possible to prepare films which had thermal histories representative of the gold distribution just prior to the formation of the large surface aggregates. The films were quickly quenched to room temperature and then examined

by SEM. It was found that surface colloidal particles - identical to the structures observed only on the air side surface of the fully cured film- populated both surfaces of the film. Therefore, the formation of these structures is not limited to the air side surface; however, these particles seem to be "permanent" on the air side surface but "transient" on the glass side surface, as will be shown in the subsequent discussion.

The preceding experiment was repeated except the optical microscope was used to observe the appearance of the gold "nuclei" which would ultimately become the large surface aggregates. This sample had a thermal history that was slightly advanced compared to the previous sample. When the surface nuclei were just observed to start forming, the sample was removed from the hot stage and prepared for SEM. Figure 49 shows an aggregate is shown that had grown to ca. 15 μm in diameter. As indicated in Chapter 4, this structure will grow to about 75-100 μm in diameter. It should be noted that surface colloid is also present and has the same size and morphology as seen in the previous sample on both surfaces of a fully cured film. Also, there is a depletion zone extending ca. 10 μm in thickness around the large aggregate.

At this point, it is useful to summarize the fate of the surface colloid as a function of thermal treatment. SEM

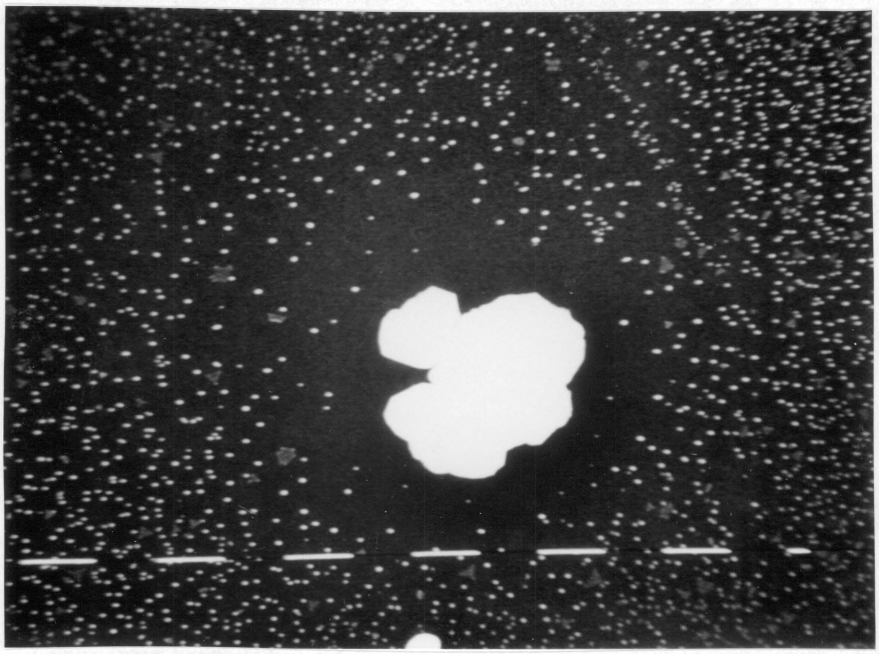

Figure 49. SEM of growing Class I aggregate with depletion zone and surface colloid particles.

indicated that these structures are not present on the surface of the 100°C thermally treated modified BTDA-ODA film. The initial heating of the film seemed to promote the formation of gold colloid at both the air and glass side surface. These structures formed only at the surface of the film, as they do not appear to be embedded into the polymer matrix, as was observed in the bulk metalizing film (Figure 18). While the structures on the air side surface persist through the full cure, this is not the case on the glass side surface. As seen in Figure 49, a depletion zone surrounds the growing aggregate. Further, none of these surface colloidal particles are observed on the glass side surface of the fully cured film. It seems inescapable to conclude that the surface colloidal particles are involved in the formation of the large surface aggregates. If these particles are partially responsible for the growing aggregates, then the particles must be transported in some manner to the periphery of the aggregate.

It is not believed that the surface colloidal particles migrate in their observed form and attach to the periphery of the growing surface cluster. Otherwise, the cluster would have a "grape-like" appearance reflecting formation by aggregation of these smaller subunits, as was reported by Weitz in the coagulation of aqueous gold colloids [56]. A more plausible transport mechanism would invoke the

evaporation and subsequent condensation of the surface colloidal particle on the growing aggregate. This process would be analogous to Ostwald ripening. In the ripening process, it is observed that larger particles in a precipitate will grow at the expense of the smaller particles. This process is governed by the Gibbs-Thompson equation, as outlined previously. This equation predicts that particles with a smaller radius are more soluble and melt at a lower temperature than larger particles.

One additional finding concerning the surface colloidal particles was obtained by high magnification SEM of a fully cured film in the region close to the aggregate periphery. Figure 50A shows a membrane which seems to envelop the aggregate. High magnification of this feature shows microscopic voids embedded in the film on the side closest to the aggregate and no corresponding features on the side opposite the membrane (Figure 50B). It appears that small holes surrounding the periphery of the aggregate lie within a well defined boarder. The size and shape of these holes is quite similar to the size and shape of the surface colloidal particles. Indeed, these pits seem to be cavities once occupied by the surface colloidal particles. The reason these imprints persist within a well defined region is unclear. It may be that gold particles, which occupied the voids, were the last structures to add to the growing

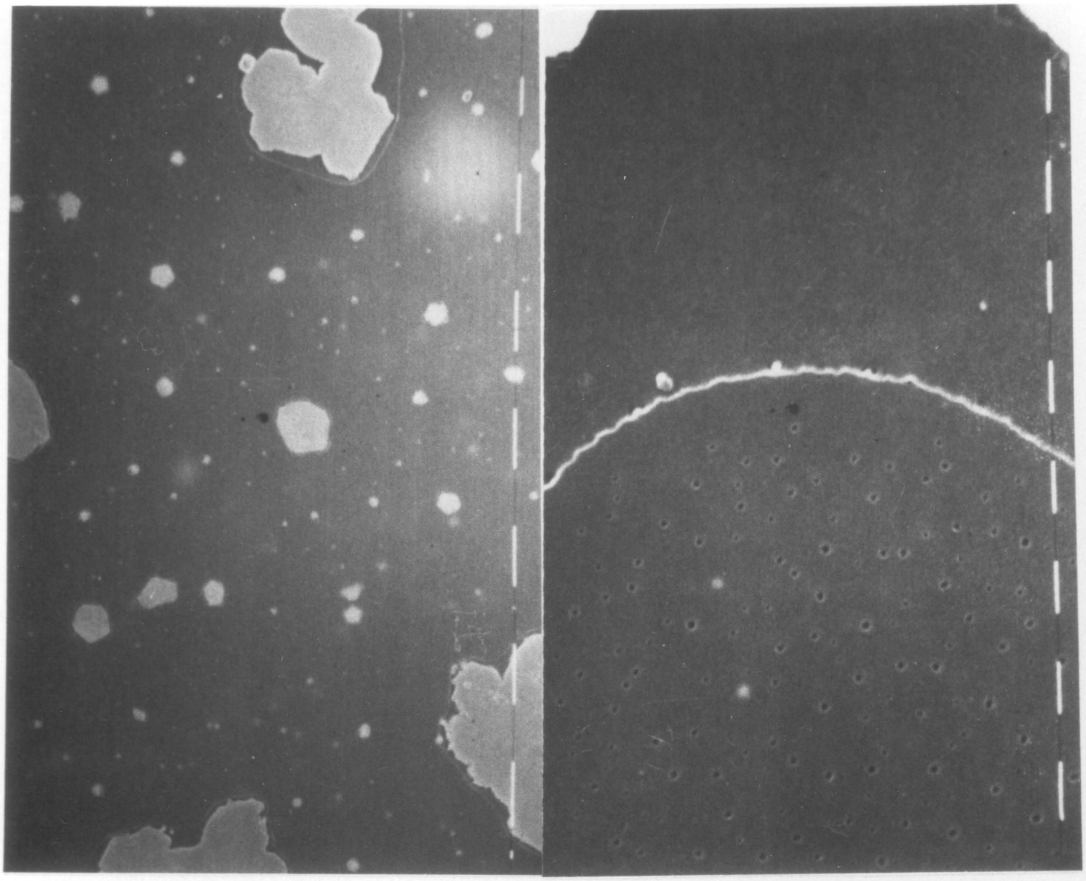

Figure 50. SEM of periphery region of Class I aggregate. A) 6400X; B) 25,000X.

aggregate by Ostwald ripening. As a consequence, the volume occupied by the particles was "frozen" into the glassy polyimide matrix. The cavities which were created in the early part of the ripening process were eliminated by the ability of the sub-Tg polyamic acid to flow. While this process is speculative, the presence of the pits and their size lends credence to the ripening theory as a means of transport in these films. Therefore, the surface colloid represents a metastable state during the metalization process.

5.2.3. GROWTH ENVIRONMENT OF SURFACE AGGREGATES

In addition to investigating the changes on the surface during aggregate growth, it was also possible to follow the changes in the bulk of the film by optical microscopy. This technique was used in Chapter 4 to follow the growth and nucleation of the Class I and II aggregates. In this chapter, optical microscopy was used to investigate the growth environment of the aggregates. The observations made concerning surface metalization will be considered in light of some aggregation models outlined in the Introduction of this chapter. As noted previously, three different categories of surface aggregates were identified based on shape: Class I aggregates were large (75-100 μm) forms with a branched periphery, Class II aggregates were smaller (10-

30 μm) and more compact, and Class III aggregates were highly dendritic, with arms emanating from a central core. The Class III aggregates sometimes lacked the central core and the dendritic arms emanated from one central point. A large number of films were studied and these three general classes of aggregates were characteristic of each film. However, there was significant variation in the relative abundance of each type of aggregate observed. Also, the size and shape of the arms varied within a class. Examples of these surface aggregates can be seen in Figure 51A.

In general, two types of particles are observed in the bulk, distinguished only by their size. The larger particles (ca. 5 μm in diameter) were termed nodules; whereas, the smaller particles (ca. 1 μm) were termed grains. When viewed with polarized transmitted light, additional features located in the interior of the film were also seen (Figure 51B). It is interesting to note that only the particles located in the interior (nodules and grains) repolarize light. The large surface aggregates did not show this effect, even when the aggregates were of comparable size during the early stages of growth. This result is similar to the bulk metalizing films which also showed optical birefringence. It is also apparent that the bulk "nodule" particles exhibit a depletion zone. This observation may provide evidence relevant to the growth

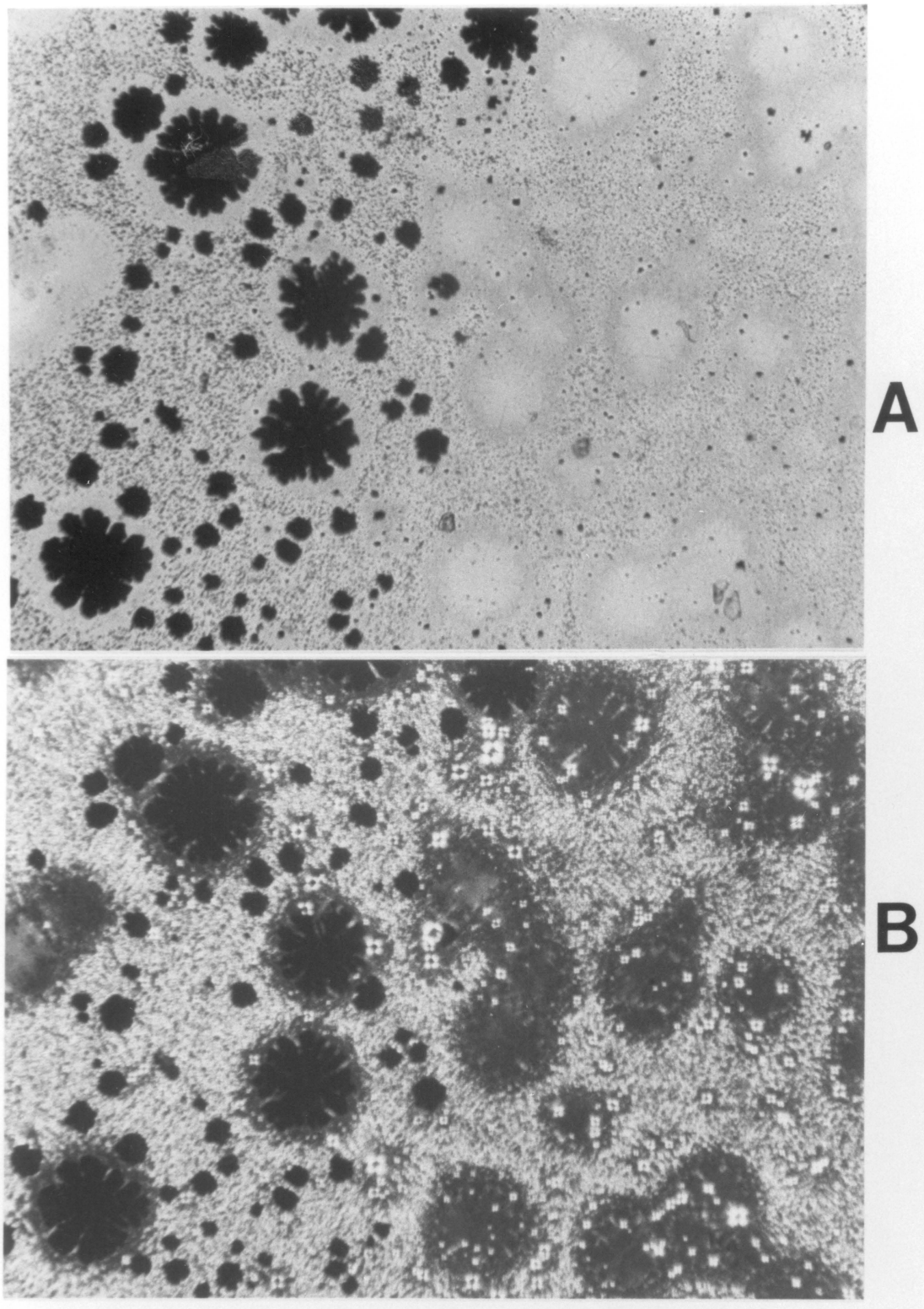

Figure 51. Transmitted light micrograph of modified BTDA-ODA film showing depletion zones and aggregates stripped from the surface, 125X. A) Unpolarized light; B) Polarized light.

mechanism, as will be discussed in the next section. The depletion zone is an area surrounding the particle which lacks any of the "grain" particles.

Figure 51 represents a modified film after heating for one hour at 200°C. As expected, Class I and II aggregates were observed on the glass side surface and the gold nodules and grains were seen in the bulk of the film. No Class III aggregates were observed in this particular region. When the film was removed from the glass casting plate, some of the Class I and II aggregates were stripped away from the surface and remained stuck on the glass. The poor adhesion of the metal to the polymer seems to be a result of the failure to "cure" the sample the final hour at 300°C. In any case, this result was fortuitous in that the environment "above" the aggregates can be studied directly. Examination of the aggregates still attached to the polymer show a depletion zone surrounding the Class I aggregates that is mostly free of any bulk particles. In addition, the exposed areas above a stripped Class I aggregate further suggest that the bulk of the film was free of gold grains. These observations define an environment from which the Class I aggregate grew. As is indicated schematically in Figure 52, there is both a horizontal (along the surface) and a vertical (from the bulk) component to the growth environment.

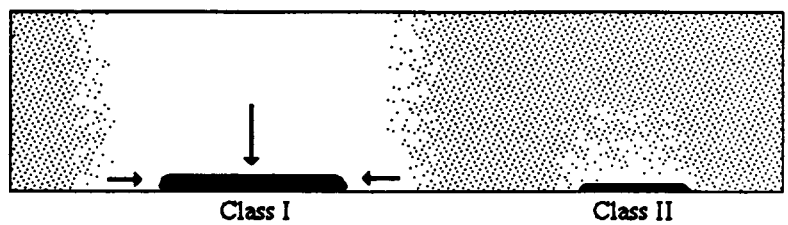

Figure 52. Schematic representation of growth environment of Class I and II aggregates.

These results can be compared to the growth environment of the Class II aggregates. Examination of Figure 51 shows the presence of the Class II particles, which originally populated the surface in the stripped area. However, there is no "fingerprint" of the Class II aggregate in the stripped region. This result suggests that the aggregates grew in a much more localized fashion and were not supplied with gold feedstock from very great distances. Also, examination of the Class II aggregates that were left behind showed no depletion zone and the presence of gold grains all the way up to the aggregate periphery. The growth environment of a Class II aggregate is illustrated in Figure 52. While no Class III aggregate was observed in the area shown in Figure 51, it is thought that these types of aggregates form from the same environment as Class I aggregrates. While none of the Class III structures were directly observed in the stripped areas, the region between gold fingers appears to be free of any bulk particles.

Four important features of surface metalization can now be summarized. These observations will then be compared to the events noted in the bulk metalizing films.

The first and foremost observation in the surface metalizing film was the tendency for the gold to migrate to the glass side surface. This phenomenon is unlike any other modified film studied and is highly dependent on the casting

surface. In the next section, this behavior will be discussed in terms of the thermodynamics of phase separation.

The second important observation concerns the presence of the depletion zones. As shown schematically in Figure 52, these depletion zones surround the Class I aggregate in both a vertical and horizontal direction. The gold dispersed in the polymer matrix is referred to as feedstock, without making specific reference to the state of the gold. The aggregates grew by "feeding" on the gold feedstock, which led to the "starved" depletion zones. The depletion zone seems to be a pervasive feature of the gold containing films. These zones represent areas devoid of feedstock that surround the aggregated gold phase, whether it was colloidal particles (30-40 angstroms), bulk particles (5 μm) or Class I aggregates (75-100 μm).

The mechanism of Ostwald ripening represents the third important feature observed in the surface metalizing films. This phenomenon was observed indirectly on the glass side surface of the BTDA-ODA film. Ripening provides a plausible mechanism for the surface colloid particles to add to the growing aggregate. It is also interesting to note that the observance of this process on the glass side surface supplies a "two dimensional" growth environment. The diffusion limited models of aggregation, which are similar

to the gold aggregates observed here, rely on a two dimensional diffusion field. Therefore, Ostwald ripening at the polymer interface may be the physical analog of the DLA process.

Lastly, the vitrification of the polymer affects the distribution of gold in the surface metalizing film. This point was explored in Chapter 4. In essence, it is believed that the increase in viscosity of the curing polymer limits the mobility of the feedstock during aggregation. Below the glass point, the Class I aggregates form; at the glass point, a cross over in aggregation is observed and the Class II and bulk particles form.

A common "theme" to the four observations noted above is the mobility of feedstock during phase separation. The presence of the large gold features on the glass side surface and the depletion zones indicate that the feedstock must traverse relatively large distances during phase separation. Also, the mechanism of Ostwald ripening is a transport phenomenon and vitrification may serve to limit the mobility of the feedstock. It seems reasonable to conclude that mobility of feedstock must be relatively high in the surface metalizing film in order to form the large aggregates. Further, when mobility is limited during vitrification, localized aggregation occurs and gives rise to the bulk particles and Class II aggregates.

The preceding discussion of feedstock mobility indicates that it is an important quantity. In "ideal" phase separation under equilibrium conditions, mobility of the components is not a consideration. However, in these non-equilibrium modified films, the phase separation process is limited by mobility. In other words, diffusion limited aggregation under non-equilibrium conditions is the process of phase separation. The latter terminology is used to make the connection between the modified films and a field of physics which deals with disordered matter. This relationship will be discussed in the last section of this chapter.

The preceding discussion emphasized the importance of mobility in the phase separation process. The dependence of solute mobility on phase separation has been studied extensively in the metallurgical literature [21,57]. In general, these texts deal with metal alloys which remain fixed in chemical composition during phase separation. However, there is an additional complication in the materials described here; that is, the composition continually changes as the dopant decomposes into gold and its by-products. Therefore, the phase separation will depend on the local concentration of gold, as well as diffusion, as discussed in the next section.

5.2.4 PHASE SEPARATION

The following expression is a generalized reaction that describes the formation of the metallic feedstock A, from the dopant A^+, at a rate R_d:

$$A^+ \longrightarrow A \qquad 5\text{-}11$$

The concentration of A will increase until a critical concentration [A]*, is obtained. At this point, phase separation will occur and result in α, the A rich phase (the metallic phase) and β, the A poor phase (matrix phase). During this process, n moles of A are transferred from β to α. The free energy of the system consists of the sum of the free energies of the two phases G^{α} and G^{β}. Therefore,

$$G_{tot} = G^{\alpha} + G^{\beta} \qquad 5\text{-}12$$

The change in free energy at constant temperature and pressure during this transfer process is:

$$dG = (dG^{\alpha}/dn_A)\, dn_A - (dG^{\beta}/dn_A)\, dn_A \qquad 5\text{-}13$$

or

$$dG = \mu_A^{\alpha}\, dn_A - \mu_A^{\beta}\, dn_A$$

At equilibrium, the free energy of the system is at a

minimum, so dG = 0. That is,

$$\mu_{\alpha} = \mu_{\beta} \qquad 5\text{-}14$$

However, if $\mu_{\alpha} < \mu_{\beta}$, then the system will attempt to minimize the chemical potential difference between the two phases by transferring A from β to α.

There is also a kinetic component to the phase separation phenomena. The velocity V, at which A is transported in the z direction during the phase separation process is

$$V_z = -M_A (d\mu_A/dz) \qquad 5\text{-}15$$

where M_A is the mobility of A and $d\mu_A/dz$ is the chemical potential gradient of A in the z direction. This equation indicates that the velocity of A will be increased by increasing the mobility or chemical potential gradient. In terms of the flux of A (velocity times concentration) the previous equation becomes

$$J_z = -M_A C_A (d\mu_A/dz) \qquad 5\text{-}16$$

The preceding equations can now be applied to phase separation in the modified films. A schematic cross section

of a 100°C film (which only contains dopant and no reduced gold) is shown in Figure 53. The component of interest in the phase separation is "atomic" gold produced by the decomposition of the dopant at higher temperatures. The atomic gold is initially soluble in the polymer; however, it will phase separate from the matrix when the critical concentration [Au]* is obtained. Also, consider that a chemical potential gradient pre-exists between the bulk and the surface(where μ_{Au} is low). Therefore, there is a driving force for surface metalization.

Now consider that a volume element exists in the bulk portion of the polymer and the boundaries of the element are only slightly permeable to the gold. This corresponds to low mobility. Therefore, the flux of gold across the boundary of the volume element on the low chemical potential side will be quite low. If the rate of gold production, R_a, in the volume element is faster than the flux of gold out of the element, J_a, then the critical concentration necessary for phase separation will be achieved. This event is shown schematically in Figure 53B. Therefore, when $R_a > J_x$ phase separation occurs on a local scale and gives rise to bulk metalization.

If instead the boundary is quite permeable to gold, then the critical concentration will not be achieved and phase separation will not occur in the volume element. This

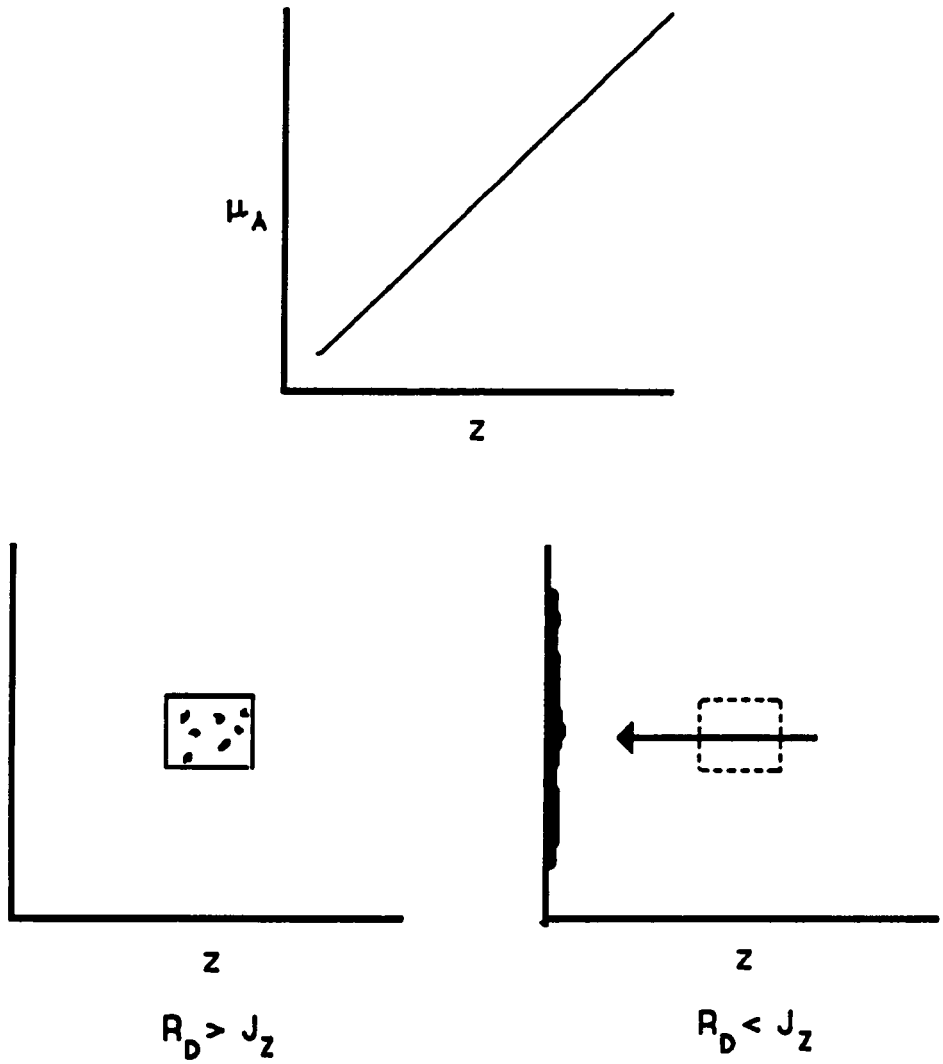

Figure 53. Representation of phase separation in modified films. A) Chemical potential gradient; B) Bulk metalization; C) Surface metalization.

corresponds to the case where $R_{ad} < J_z$. As a result, surface metalization properties are observed.

A third case can also be explored, where the mobility M, starts out high and then becomes low. From the preceding model, surface metalization would be expected to occur first followed by the formation of bulk particles. In fact, this is the order of phase separation observed in the BTDA-ODA surface metalizing film.

The preceding model was developed to relate the observed phase separation process to the diffusion of feedstock in a chemical potential gradient and the rate of feedstock production. The thermodynamic approach invoked a chemical potential gradient in the films. The kinetics of the decomposition reaction and its relationship to flux were also considered. In a qualitative way, the model describes the phase separation process observed with optical microscopy.

However, the model does not account for the colloidal gold detected by SAXS. Therefore, it is necessary to consider this material as well. As indicated previously, the SAXS data suggests that spinoidal decomposition may be an initial phase separation process that gives rise to the colloidal particles. However, these particles are not mobile, and therefore cannot be the precursors to the surface aggregates or bulk particles. The fact that the

scattering intensity increases with time suggests that the electron density between the scattering elements and the background is increasing. This effect can be accounted for in two ways; either the colloidal particles are densifying or the dispersed gold is being depleted. The second explanation is consistent with the macroscopic observation of the simultaneous formation of the larger gold particles. Therefore, the remaining gold which did not participate in spinoidal decomposition was involved in the formation of the much larger features outlined in the previous model.

The chemical potential gradient is a reflection of the lower Gibbs free energy of gold at the surface than in the bulk of the preceding film. This conclusion demonstrates the importance of the "interphase" properties of the films during preparation. The sensitivity of the modified BTDA-ODA film to the casting surface was made evident in Chapter 4. Therefore, the physical properties (nucleation sites, mechanical properties, transport, etc.) and the chemical properties (atmosphere during casting, surface chemistry of the casting surface) of the interphase region may be as important as the choice of polymer and metal in film fabrication.

5.2.5 GROWTH MODELS

In order to relate the shape of an aggregate with its

growth environment and the order in which the aggregate evolved during the thermal treatment, it useful to compare models described in the Introduction to this chapter with the observations cited in the previous sections. It is important to stress that the following models are products of computer simulations. These models are relatively easy to visualize and, therefore, provide a convenient mechanism to illustrate aggregation. However, direct comparison of these two dimensional models with the gold aggregates described in this manuscript can only suggest a possible mechanism of aggregate formation.

Several analogies can be made between the computer generated forms and the gold aggregates on the polyimide film. As stated previously, phase separation occurs by the diffusion of gold feedstock through the polymer matrix and its subsequent aggregation near the glass side surface of the film. The Brownian motion of feedstock in the polymer matrix would be analogous to the random walk of particles in the DLA model; and as indicated previously, there is a two dimensional component to the aggregation process (Ostwald ripening of the surface colloidal particles). Further, it was observed that the presence of the glass casting plate was necessary for the formation of aggregates. It may be that the glass provides nucleation sites for the aggregation process, which emulates the seed particles in the DLA model.

It is also interesting to compare the shape of these aggregates to the simulations and experiments outlined in the Introduction. In this way, a qualitative understanding of aggregate pattern selection can be attained.

The Class III aggregate shown in Figure 21 possesses a ramified structure similar to the Witten-Sander DLA shown in Figure 33. Experiments are currently underway to obtain the dimensionality by measuring the scaling properties of the structure through image digitization at Sandia National Laboratories. Observing the growth of a Class I aggregate using a video camera indicates that these aggregates grew from an initially circular nucleus, approximately 5μm in diameter. The surface of the aggregate appeared to "roughen" and then the arms grew out from the central core. This progression of events, known as growth instability, has been treated in dendritic solidification by Mullins and Serkerka [44] as well as others.

The application of growth instability in DLA was shown recently by Sander [39]. In Figure 54, the vertical arrows represent the flux direction of the random walkers, the horizontal lines represent contours of equal walker density and the solid area represents the surface of the growing structure. A small bump is introduced on the surface of the aggregate (Figure 54A) and growth occurs preferentially at the tip (Figures 54B and 54C). In the Mullins-Serkerka

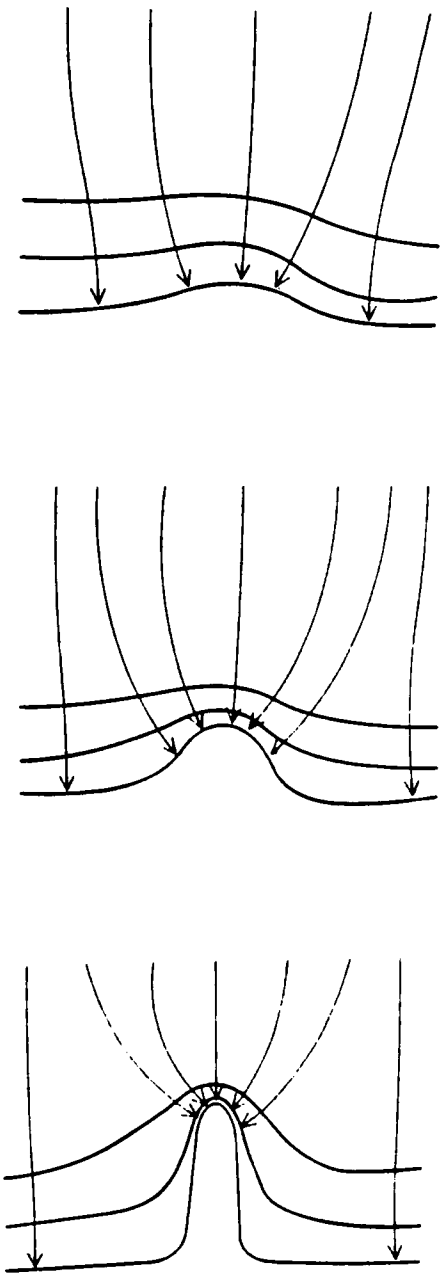

Figure 54. Schematic representation of growth instability. The pattern evolves in time from A to C (from Reference 39).

treatment, the bump represents a surface perturbation which can be modeled by a sinusoidal wave. In Sander's discussion, the bump formed due to the random nature of the incoming walkers. Subsequent walkers are more likely to encounter the tip of the growing arm than diffuse down into the interior "fjord" regions between the arms. For this reason, growth occurs preferentially at the tips and gives rise to the ramified structures typical of DLA growth. Therefore, growth instability is another important feature of DLA growth that is observed in the aggregates.

DLA growth is thought to control the shape of a variety of different structures, as indicated in the Introduction. Electrical discharge patterns are similar to the Class I aggregates, even though each was formed in an entirely different fashion. However, DLA structures formed by the sputter deposition of metals not only appear similar to the gold aggregates, but share some similar features in their formation. For instance, $NbGe_2$ was deposited onto quartz by rf reactive sputtering of a niobium target in a argon/germane gas mixture [58]. This process occurs by the formation of an "atomic" vapor of the alloy which then condenses and forms the DLA structures. Most importantly, a three dimensional feedstock environment (vapor) gives rise to two dimensional fractal structures. As discussed previously, an "atomic" gold-condensation model was proposed

as a physical picture of supercooling in the modified films. Therefore, the three dimensional depletion zone, which gave rise to the two dimensional aggregate, is analogous to the growth environment of the metal sputtered films.

In most cases, the Class III aggregate exhibited the core-arm morphology. However, Class III aggregates have also been observed which lacked the central core and therefore bear a closer resemblance to the "classic" Witten-Sander DLA cluster. This sample was prepared by loosening the 100°C film from the glass casting plate prior to the high temperature thermal treatment (Figure 24). In general, the aggregates observed in a sample prepared in this manner were more ramified. Again, the interfacial properties between the polymer and the casting surface seem to influence the metalization process. While the relationship between adhesion and aggregate morphology is not understood, it may be that transport in the interfacial region was altered in this experiment.

The Class I aggregates possess much thicker "branches" than the DLA structure and appear to be intermediate in shape between Class III and II. These features are quite similar to the DBM (dense branched morphology) which has been studied experimentally by Ben-Jacob and Suresh. In a subsequent discussion, DBM and its relationship to the Class I aggregates will be discussed in greater detail. Vapor

deposition has also generated shapes that look very much like the Class I aggregates. In this case, gold was vapor deposited onto a polycarbonate substrate [59]. The same mechanism of aggregation is believed to occur in the case of gold as in $NbGe_2$.

The Class II aggregates resemble Eden clusters. In this type of growth, symmetric structures are observed, which indicates that growth occurred at an equal rate at all surface sites.

The three classes of aggregates can be simulated by three distinctly different mechanisms of growth; DLA, DBM and Eden growth. However, the generalized Witten-Sander model is capable of generating all three structures by variation of the sticking probability, as outlined in the Introduction to this chapter. Using radial geometry, the evolution of the DLA structure shown in Figure 39 seems to model the gold aggregates shown in Figure 21 and 51. In addition, using this model and employing rectangular geometry gave rise to viscous fingers (Figure 40). Similar features grew at the film interface of samples sandwiched between glass microscope slides, as shown in Figure 55.

The fact that the generalized Witten-Sander model is capable of producing structures which resemble all three classes of aggregates and the viscous finger "fringe" strongly suggests that a diffusion limited process is

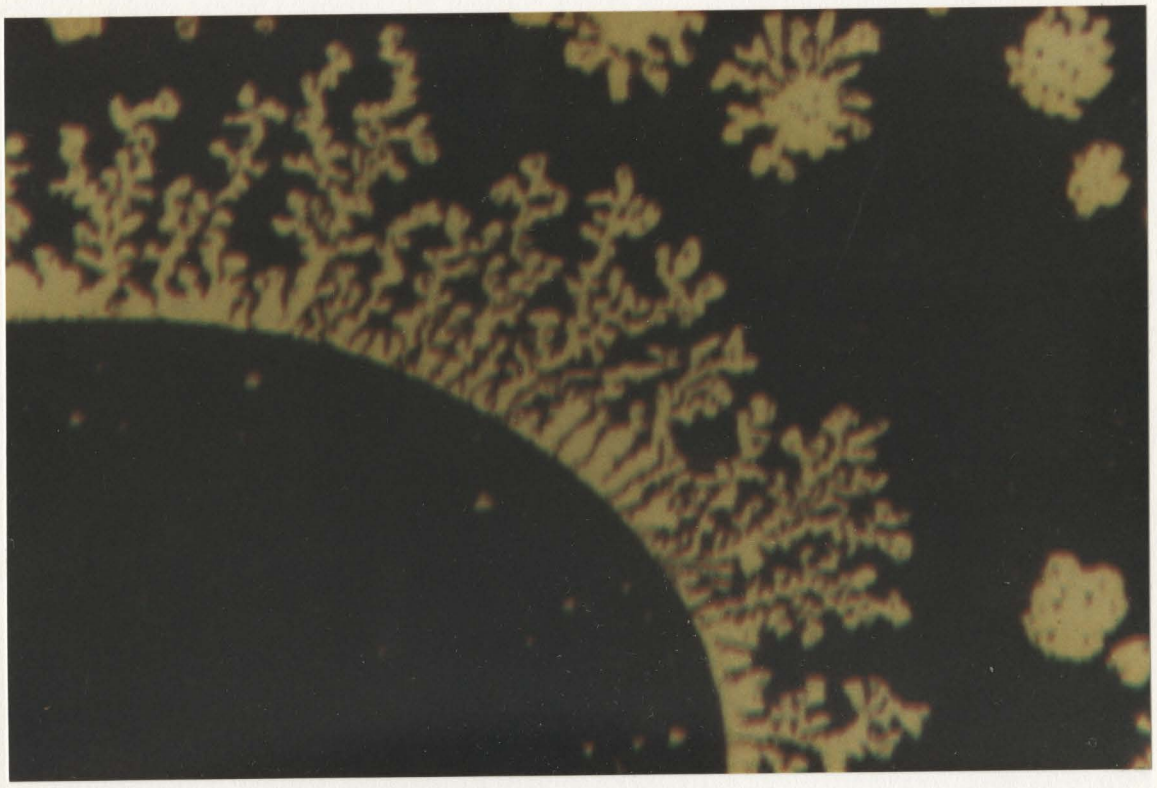

Figure 55. Reflected light micrograph of gold viscous fingers growing from an interfacial region in modified BTDA-ODA, 150X.

responsible for the gold surface aggregates. In this model, it is possible to introduce a surface tension via the sticking probability. However, it is difficult to envisage a suitable physical counterpart to the surface tension. Gold is a very high surface tension material and it is doubtful that there is any difference in surface tension between the three classes of aggregates.

However, the shape may be related to the growth rate of the aggregate. If the diffusion limited growth rate of the cluster is quite high, then other physical effects, such as surface tension, may not have time to exert any influence on the shape of the ultimate structure. Growth occurs quickly at the tips of the cluster and DLA structures are observed. If growth is slow, then surface tension effects would predominate and give rise to a more spherical (Eden) morphology [60]. One of the attractive aspects of the model presented below, is that features similar to the aggregates are formed without having to invoke changes in surface tension.

In addition to the qualitative similarity between the gold aggregates and the computer simulations outlined above, the shape of the aggregates can be compared to non-fractal structures as well. In the introduction to this chapter, it was noted that the dense branched morphology (DBM) observed in a Hele-Shaw cell and lipid monolayer bear a strong

resemblance to the fractal aggregates. Stanley, et. al. [48] recognized the strong similarity between the previously cited works and the gold aggregates reported here. Consequently, they developed a model which can be used to describe the formation of the gold aggregates.

In this section, the work of Stanley, Nittmann and Suresh will be discussed in some detail. While several investigators worked on the development of the model described, it will be referred to as the Stanley model. The features of this model which are most applicable to the surface aggregates will be discussed and compared to the other models of aggregation outlined above. In order to fully describe the Stanley model it is useful to relate some aspects of the lipid monolayer experiments, which bear a strong resemblance to the gold aggregates.

Recently, Suresh et. al. [47] studied the phase separation behavior of a lipid monolayer on water. The lipid condensed phase L_c, can be observed by the addition of a fluorescent dye to the system. The lipid condensed phase exists as domains in the lipid expanded phase L_e, as indicated in the phase diagram of Figure 56. It was observed that the shape of the condensed phase changed from a circular morphology to a dense branched morphology as the critical temperature T_c, is approached. It is interesting to note that the circular morphology bears a striking

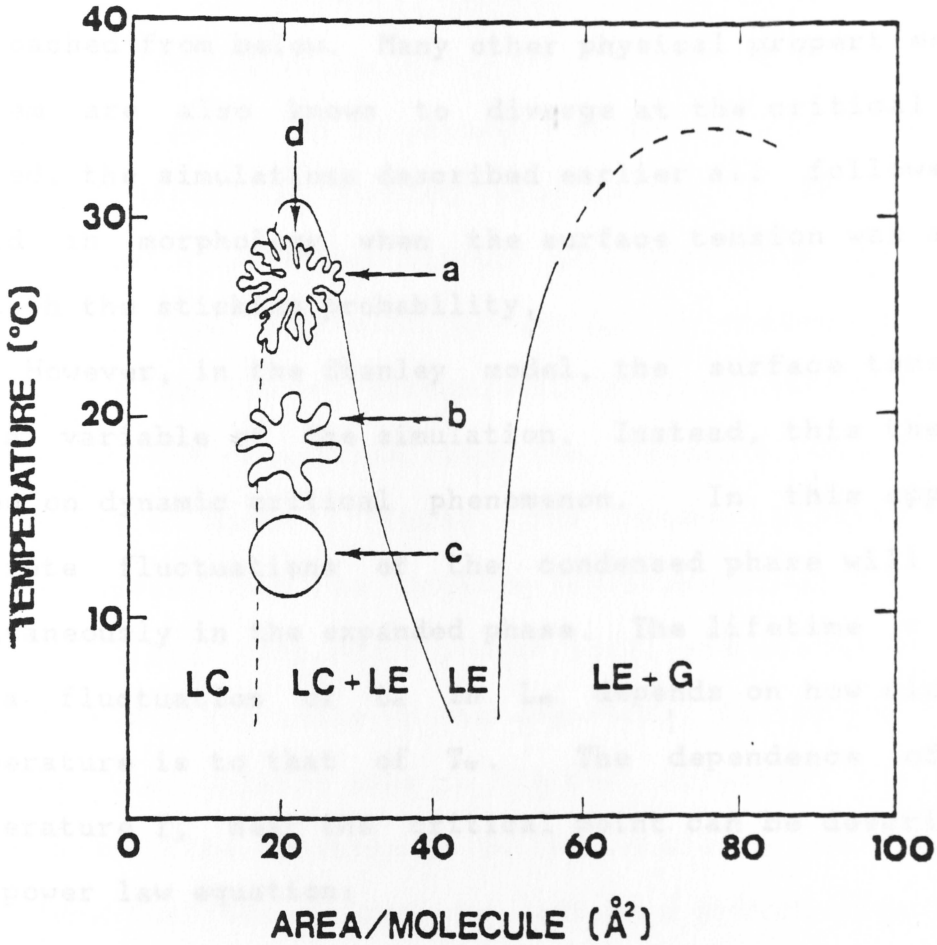

Figure 56. Phase diagram of lipid monolayer (from Reference 47).

similarity to the Class II aggregates whereas, the structures obtained near T_c are similar to the densely branched Class I structures. In the case of the monolayer, it was concluded that the change in morphology was due to a reduction in the surface tension of the aggregate as T_c is approached from below. Many other physical properties of a system are also known to diverge at the critical point. Indeed, the simulations described earlier all followed this trend in morphology when the surface tension was altered through the sticking probability.

However, in the Stanley model, the surface tension is not a variable of the simulation. Instead, this theory is based on dynamic critical phenomenon. In this approach, discrete fluctuations of the condensed phase will appear spontaneously in the expanded phase. The lifetime τ (Tau), of a fluctuation of L_c in L_e depends on how close the temperature is to that of T_c. The dependence of τ on temperature T, near the critical point can be described by the power law equation:

$$\tau \approx (T - T_c)^{-z} \approx (\Delta T)^{-z} \qquad 5\text{-}17$$

Therefore, as the critical temperature is approached from below, ΔT decreases and the lifetime of a fluctuation τ, increases.

As Stanley indicated, a value of -2 for the critical exponent is associated with diffusion of the the fluctuations. Near the critical point, the fluctuations of the L_c phase are able to diffuse through the L_∞ phase by Brownian motion. However, these diffusing entities only have a discrete lifetime, τ.

At this point, it is possible to relate the fluctuation model to diffusion limited aggregation. This approach assumes that the fluctuations are analogous to random walkers and their diffusion through L_∞ is analogous to the random walk on the two dimensional lattice. However, there are two notable departures from the "classic" DLA approach in Stanley's model. First, the random walkers can be created anywhere on the lattice (corresponding to a local diffusion field) with equal probability, whereas walkers are created at distant sites in DLA (non-local diffusion field). Secondly, the walkers have a limited lifetime, τ. In DLA there is no "time dependence" on the existence of a walker. In order for the walker to add to a growth site in the Stanley model, it must do so in the time interval t, where $0 < t < \tau$.

A consequence of modeling the phase separation of lipids by the Stanley model is that it generates non-fractal objects. This is a result of the local diffusion field, which "launches" walkers from the "fjords" of the growing

condensed phase. Stanley showed how the shape of a domain will change as the critical temperature is approached. At temperatures well below T_c, τ will be quite small, as shown by Equation 5-17. Only those fluctuations (walkers) created near the periphery of the growing condensed domain have a chance to participate in aggregation. Fluctuations created at more distant sites will "die" ($t > \tau$) before they are able to traverse the distance necessary to participate in the cluster growth. As a result, the Stanley model reduces to the Eden model in the limit of $\tau \longrightarrow 0$.

As the temperature approaches T_c, then τ approaches infinity, which mandates that all walkers can participate in cluster growth. The evolution of the aggregate shape generated as a function of τ is shown in Figure 57. Stanley reported that the density of the aggregate did not decrease as the radius increased, which verifies that the dense branched morphology of Figure 57 is not a fractal structure. Comparison of the phase behavior of the Suresh lipids and the theoretical work of Stanley is in good agreement.

In the "Tau" model outlined above, any number of random walkers can be generated from a lattice site (or in the lipid monolayer, an infinite number of fluctuations could appear at different times in the same region of space). However, Stanley defined a new parameter F, the concentration of "feedstock", as the maximum number of

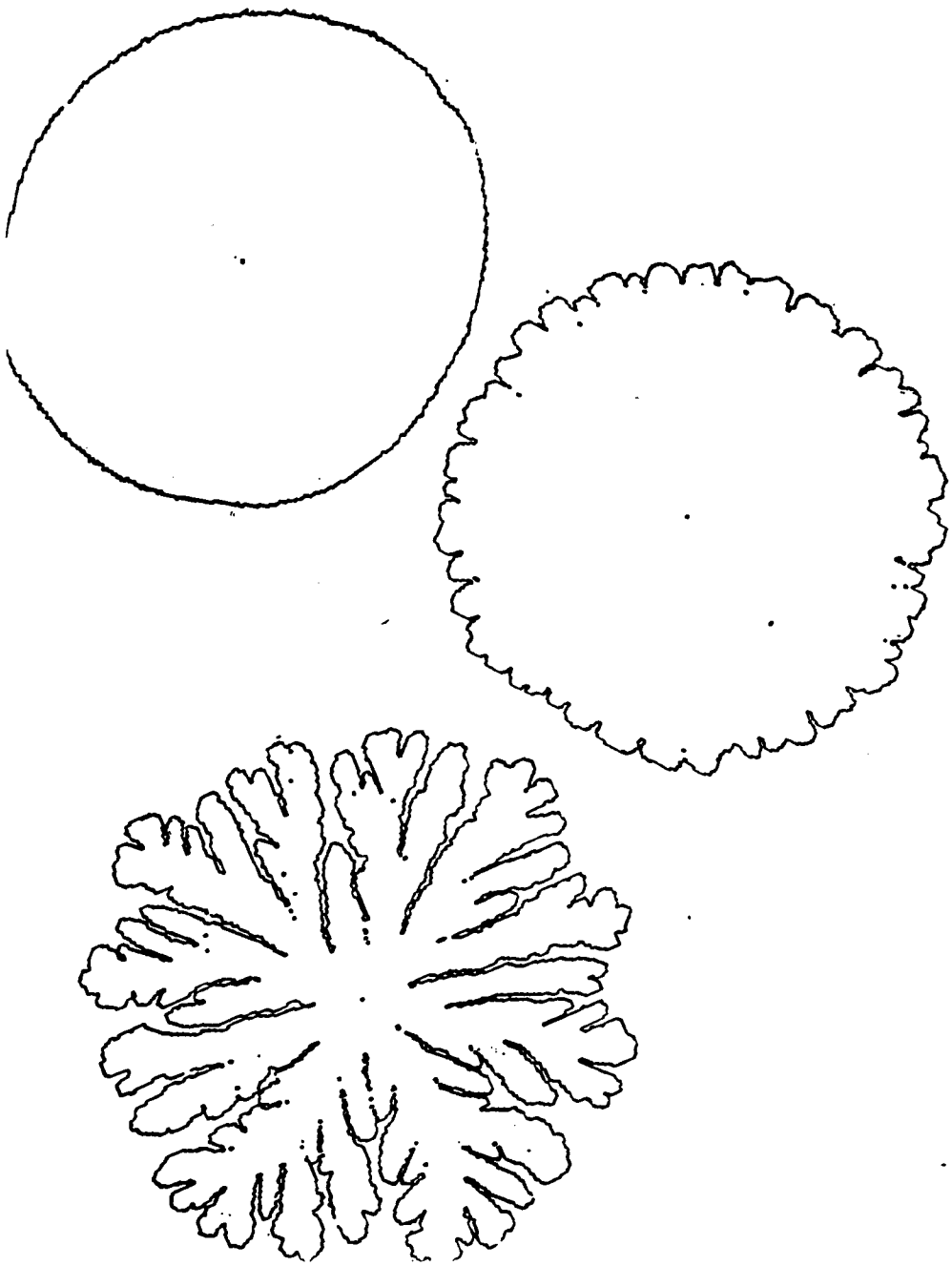

Figure 57. Evolution of pattern in the Tau model. A) τ=1; B) τ=20; C) τ=6400 (from Reference 48).

walkers that can be launched from any lattice site. Therefore, in the Tau model, F is equal to infinity. In the limit of F=1, walkers adding to the cluster are more likely to come from increasingly distant sites and the morphology would resemble the Witten-Sander DLA cluster. For intermediate values of F, Stanley observed that the shape of the aggregate "crossed over" from a DBM (where τ is large and F is large) to a DLA type structure (where τ is large and F is small). Therefore, the evolution of the pattern is controlled by the depletion of feedstock as F decreases. In Figure 58 Stanley showed the morphology of a cluster formed by the τ-F model; this simulation does have the appearance of the "core-arm" typical of the Class III aggregates.

The τ-F model is applicable to the formation of the gold aggregates because fluctuations giving rise to the condensed phase (gold aggregates) would be of infinite duration (τ —> infinity). Also, the number of fluctuations is limited by the availability of feedstock. Further, a "DBM-like" or "DLA-like" structure can be generated by adjustment of the variable F. At high values of F, DBM type structures will grow; whereas, at low values of F, DLA structures will prevail. However, to generate these "pure" DLA or DBM patterns, the value of F would have to be held constant rather than decremented.

According to the Stanley model, the local concentration

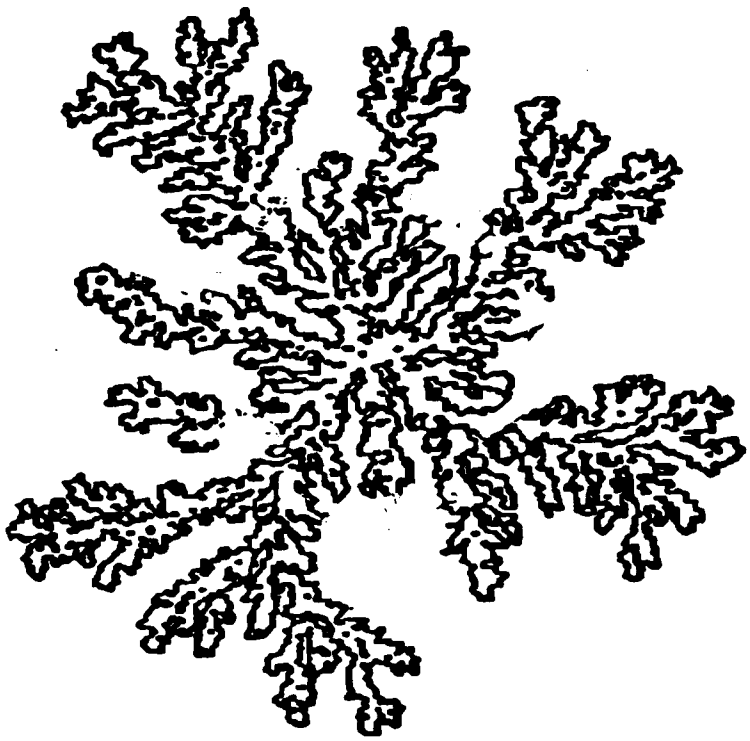

Figure 58. Pattern generated from the T-F model (from Reference 48).

of gold during the aggregation process accounts for the various Classes of structure. If growth occurs while there is a low concentration of the gold feedstock present, then ramified structures occur. However, if the local concentration of feedstock gold is high, then the DBM structure or Eden growth is observed. Therefore, the Stanley model relies of the parameter F, rather than surface tension to explain the aggregates. Indeed, the general trend observed is that the more ramified gold aggregates were the first observed in the growth process (when feedstock is low) whereas the more compact structures form at longer times when more feedstock is present.

CHAPTER 6

CONCLUSIONS AND FUTURE WORK

The goal of this work was to characterize and describe phase separation in polyimide films modified by the incorporation of hydrogen tetrachloroaurate. The study of phase separation in these materials is quite important, as the ultimate distribution of metal will greatly affect the properties of the film.

Regardless of their visual appearance, the surfaces of these films were comprised mainly of polyimide as indicated by XPS. In some cases, the photoelectron peaks were quite complex; however, the polymer did not seem to be chemically altered by the modification process. This finding was also supported by infrared spectroscopy.

The thermal treatment used to imidize the polymer also promoted phase separation by the nucleation and growth of a metallic gold phase. In the bulk metalizing films, gold domains were quite small and dispersed throughout the film. However, surface metalization occurred by the nucleation and growth of large gold aggregates. The kinetics of aggregate nucleation is quite similar to the process observed in aqueous gold colloids. The similarity between these two systems may not be surprising, considering

colloidal gold was observed in these films by UV/Vis spectroscopy and microscopy. Spinoidal decomposition may also be involved in the formation of a colloidal gold phase, as evidenced by a correlation peak in the SAXS scattering profiles.

The gold domains appear to grow by the diffusion and subsequent aggregation of gold feedstock. This process also leads to the development of depletion zones around the aggregates. The mobility of the gold feedstock may be influenced by the physical state of the polymer. This conclusion was based on the relationship between degree of imidization and aggregation. Transport of the feedstock may occur in a process quite similar to Ostwald ripening.

The importance of diffusion in the phase separation process is also quite apparent by the shape of the surface aggregates. Diffusion limited aggregation and its variants provide a model for gold aggregation that is consistent with the experimental results described here. A model developed by Stanley, based in part on the results cited here, accounts for the various morphologies which comprise the metallic surface layer.

Future examination of the phase separation process in these materials would fall into two catagories. First, a more through investigation of the variables which affect gold aggregate growth would be valuable in understanding

the basics of aggregate formation. Secondly, extension of these studies to other metal/polymer systems would extend the understanding of in-situ polymer metalization. To meet these goals, the following experiments are proposed.

It would be quite useful to digitize the video signal used to evaluate the growth process. By measuring the radius of gyration as a function of mass, one could calculate a fractal exponent for the various shapes observed on the glass side surface of the gold films. A possible result of this type of experiment may show a cross over in the growth exponent, which may be interpreted as a type of growth transition. Also, it would be possible to measure the locus of growth; that is, the rate of growth at the tips of the growing dendrites could be compared to the rate of growth in the fjords.

The concentration of gold added to the films could also be studied over a much larger range. In this way, a minimum concentration of gold necessary to form fractal-like aggregates could be found. Combined with digitization, one could explore the types of aggregates formed as a function of metal content.

In order to understand the metalization process in polymers as a whole, it would be useful to expand the investigations described in this work to other metal and polymer systems. For instance, other metal/polyimide

systems are known to form continuous metal layers during thermal treatment. Microscopy could be used to determine if aggregates are precursors to the continuous metal layer. Also it would be instructive to evaluate the metalization process in a variety of other polymers with different glass transition temperatures. In this way, the relationship between viscoelastic properties and metalization could be better understood.

CHAPTER 7

APPENDIX

7.1 Ultraviolet Treatment of Modified Films

In a previously published report [7], the effect of UV exposure on a 100° C thermally treated modified XU-218 film was examined. It was found that a high intensity UV lamp was quite efficient in reducing the dopant to metallic gold on the surface of the film. Also, the film remained transparent after exposure. Subsequent thermal treatment of the exposed film (through 300° C) produced a highly reflective and metallic air side surface. Cross sections of this film examined by STEM revealed that the air side surface of the film was comprised of a high density of gold particles approximately 100 nm in diameter.

The preceding result suggests that gold containing air side surfaces may be produced by UV treatment prior to high temperature thermal treatment. Thiessen showed that colloidal gold can be produced by exposing solutions of chloroauric acid to UV light [22]. Therefore, the exposure of the modified XU 218 film to the UV source may have produced colloidal gold nuclei at the surface of the film. During thermal treatment, the gold particles grew and

formed the highly reflective metallic layer. Without the UV treatment, there is no preference for gold nuclei to form at the surface of the film and bulk metalization was observed.

The UV/thermal treatment of modified BTDA-ODA films also enhanced the reflectivity of the air side surface; however, the effect was not as pronounced as in the case of the XU 218 film. It was also observed that the glass side surface metalized in the usual manner in these films. It seems likely that the competition for the gold feedstock between these two surfaces was partly responsible for the diminished air side surface reflectivity of the BTDA-ODA film compared the XU 218 film.

7.2 Polyimide Casting Surfaces

In order to increase the mechanical strength of the modified polyimide films, a procedure was developed to produce multilayer films. In the first step, an unmodified BTDA-ODA solution was cast onto glass and heated through the full heat cycle (to 300° C). The film was cooled to room temperature and left stuck to the glass plate. A modified polyamic acid solution was then cast onto the fully cured polyimide film. It was noted that the solution did not seem to dissolve, swell or otherwise attack the polyimide substrate. The ensemble was then placed back

into the oven and heated in the usual manner.

Modified gold films derived from pyromellitic dianhydride-oxydianiline (PMDA-ODA) are usually quite brittle and shred when removed from the glass casting substrate. However, the same film cast onto an unmodified PMDA-ODA substrate produced a modified gold film that retained structural integrity. The two films adhered quite well to one another and could not be delaminated. It is believed that this technique can be used to produce modified films from materials which otherwise may not be suitable. Also, this technique could be used to apply a very thin coating of a modified polyamic acid solution to an unmodified film, thus decreasing the amount of metal needed to modify the surface properties of high temperature polymer films.

7.3 Thermal Gravimetric Analysis of $HAuCl_4 \cdot H_2O$

Thermogravimetric analysis (TGA) was used to evaluate the fate of chloroauric acid as a function of temperature. The gold compound was loaded into a glass lined platinum pan and heated at 10° C per minute between 50° and 400° C under a nitrogen atmosphere. Transfering the dopant from the reagent bottle to the thermal balance exposed the hydroscopic salt to atmospheric moisture. Figure 59 shows the weight loss suffered by the dopant as a function of

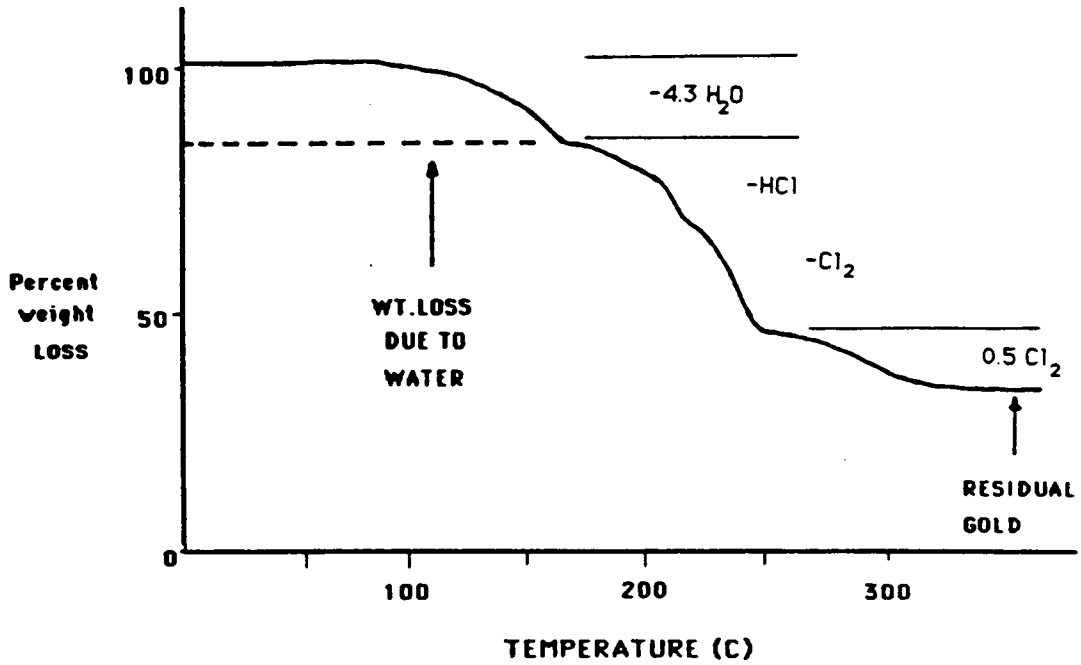

Figure 59. Thermal Gravimetric Analysis of Chloroauric acid.

temperature and it is apparent that decomposition is a multi-step process. Visual inspection of the TGA pan after the experiment revealed a metallic gold residue was left. Therefore, the plateau region between 300 and 400° C corresponded to the weight of the residual metallic gold. The weight loss events described below were calculated by assuming that 47.22% of the orginal sample weight left after the experiment was due to metallic gold. The first weight loss event (50-140° C) corresponded to the loss of 4.3 water molecules from each molecule of $HAuCl_4$. The high degree of hydration is probably due to the hydroscopic nature of the dopant and the uptake of atmospheric moisture during transferal.

The weight lost between 140° and 250° C has an inflection point at about 210° C. A total of 31.48% of the orginal sample weight was lost in this region.A theoretical weight loss of 31.59% is expected if anhydrous $HAuCl_4$ looses HCl and Cl_2. The inflection point may correspond to the transitory existance of $AuCl_3$ during decomposition.

Between 250° and 300° C the sample lost 7.93% of its orginal weight. If the inflection point at 250° corresponded to AuCl then a weight loss of 8.41% is expected. Based on the preceding results the following thermal decomposition of the dopant under nitrogen is proposed:

$$HAuCl_4 \cdot 4.3H_2O \longrightarrow HAuCl_4 + 4.3\ H_2O$$

$$HAuCl_4 \longrightarrow AuCl_3 + HCl$$

$$AuCl_3 \longrightarrow AuCl + Cl_2$$

$$AuCl \longrightarrow Au + 0.5Cl_2$$

The intermediates are proposed based on weight loss. In order to confirm the mechanism of decomposition, mass spectrometry of the evolved gases could be used. These results indicate that reduction of the gold occurs along with oxidation of chloride. Therefore, metallic gold is produced without the need of an external reducing agent. In the actual modified films, reduction occurs at lower temperatures, as indicated by hot stage optical microscopy.

7.4 Presence of Water During Fabrication

As reported in Chapter 3, some XU 218 films were produced that exhibited a glass side surface layer of gold. Later efforts to reproduce these materials were unsuccessful. In an attempt to understand these conflicting results, the role of water in the metalization process was explored.

In Chapter 3, it was shown that water of imidization was probably not involved in the metalization process. This effect was explored by comparing the properties of films derived from both XU 218 and BTDA-DAPI (the polyamic acid

counterpart of the soluble polyimide). In both cases, bulk metalization was observed. Therefore, it was concluded that the water evolved during imidization was not the factor which was necessary to form the surface aggregates.

The effect of added water was also examined. Two modified XU 218 solutions were prepared as outlined in Chapter 2. Approximately 0.5 mL of water was added to one of the preparations. Upon addition, the solution turned cloudy in the area of the water drop. However, the turbidity disappeared with stirring. The films were then cast in the usual manner and subjected to the full thermal treatment. Inspection of the resulting films showed no visual difference between the water "spiked" sample and the conventionally modified XU 218 film. These results suggested that wet solvent or wet XU 218 was not responsible for surface metalization.

The effect of moisture in the oven atmosphere was also examined. A fully cured modified XU 218 film was prepared under an atmosphere of water saturated nitrogen. The resulting film possessed a large number of bubbles. However, surface metalization was not observed in this film.

The preceding results indicated that adventitious water was probably not responsible for the anomalous XU 218 results. Other factors, such as impurities in the dopant,

glassware or casting surface may be responsible for the anomalous behavior of this system.

7.5 Differential Scanning Calorimetry of Modified Films

Differential scanning calorimetry (DSC) was used to evaluate the effect of polymer modification on the glass transition temperature (Tg) of polyimide films. Fully cured XU 218 and BTDA-ODA unmodified films, as well as films modified at one-half and one millimole of gold per millimole of polymer repeat unit were examined. It was observed that modification increased the Tg. Further, increasing the concentration of dopant further increased Tg, as shown in Table 7:

Table 7

Effect of Gold Modification on the Glass Temperature of Fully Cured XU 218 and BTDA-ODA Films.

Modification level	XU 218 (°C)	BTDA-ODA (°C)
unmodified	319	275
0.5X	325	283
1.0X	329	287

The increase in Tg upon modification is analogous to the effect of a reinforcing filler. In the case of the filler, interaction between polymer chains and the filler

particle may act to stiffen the matrix and increase the modulus and Tg [61]. However, the IR spectroscopy and XPS results of Chapter 3 concluded that there was no alteration of the polymer chains upon modification. Therefore, the DSC data seemed to contradict the spectroscopic results. It may be that modification promotes the formation of crosslinks between the chains which increases the Tg, yet the extent of reaction is too small to be detected by XPS and IR.

7.6 Dopants other than chloroauric acid and co-doped Films.

In addition to chloroauric acid, $AuBr_3$, AuI_3, and $AuCl_3S(CH_3)_2$ were used as gold dopants. All of these materials were soluble in the polyamic acid solution; however, only films derived from chloroauric acid exhibited the metallic glass side surface. A XU 218 film modified with $AuBr_3$ produced a transparent film that was bright red in transmitted light. This material was excluded from further consideration since surface metalization was not observed. Similarly, a transparent brown film was produced by the incorporation of AuI_3 into a BTDA-ODA film.

A BTDA-ODA film modified with $AuCl_3S(CH_3)_2$ also produced a transparent brown film. However, the air side surface of the film exhibited a slightly reflective surface when observed with reflected light. While the surface was

not conductive (as measured with an ohmmeter) the reflective quality and integrity of this film merit further study.

The use of more than one dopant was studied in the hope of fabricating more conductive metallic surface layers. Chloroauric acid was used in conjunction with either $SnCl_4 \cdot 2DMSO$ or $LiPdCl_4$ (LTP). The total number of moles of metal dopant to polymer repeat unit was approximately the same as used in the previous films. A BTDA-ODA film co-doped with chloroauric acid and $SnCl_4 \cdot 2DMSO$ was very brittle and cracked upon removal from the glass casting surface. For this reason the material was cast on top of a BTDA-ODA film as described in Section 7.3. The resulting film had a gold-bronze air side surface and was opaque to transmitted light. Although the film was not conductive ($>10^{15}$ Ohm) it was studied further with SEM. High magnification (3000X) indicated that the metal separated into two phases; the continuous phase was quite convoluted and the second phase consisted of small discrete particles which adhered to the continuous phase.

Co-doped films formed from chloroauric acid and LTP were quite brittle and did not merit further study. However, addition of LTP seemed to enhance the luster of the glass side surface metallic layer. High magnification of the gold aggregates on the glass side surface revealed

small satellite particles (1μm) that adhered to the larger gold aggregates.

REFERENCES

1. A.E. Javits, Design, January (1965), p. 64.
2. G. Piatti, R. Matera and G. Pellegrini, Advances in Composite Materials, G. Piatti, Ed., Applied Science Publishers Ltd., London, 1978, p. 53.
3. G. Lubin, Handbook of Composites, G. Lubin, Ed., Van Nostrand Reinhold Co., New York, 1982.
4. T. L. Wohlford, J. Schaff, L.T. Taylor, A. K. St. Clair, T. A. Furtsch and E. Khor, Conductive Polymers, R. B. Seymour, Ed., Plenum Press, New York, 1981.
5. S. A. Ezzell, T. A. Furtsch, E. Khor and L. T. Taylor, J. Polym. Sci. Polym. Chem., Ed., 21, 865 (1983).
6. S.A. Ezzell and L.T. Taylor, Macromol. 17, 1627 (1984).
7. D. G. Madeleine and L.T. Taylor, Polyimides: Synthesis, Characterization and Application, K.L. Mittal, Ed., Plenum Press, New York, 1984, p. 670.
8. R. K. Boggess and L. T. Taylor, Polyimides: Synthesis, Characterization and Applications, K.L. Mittal, Ed., Plenum Press, New York, 1984, p. 691.
9. R. A. Dine-Hart and, W. W. Wright, Makromol. Chem. 143, 189 (1971).

10. S. Numata, K. Fujisaki, N. Kinjo, Polyimides: Synthesis, Characterization and Applications, K.L. Mittal, Ed., Plenum Press, New York, 1984, p. 259.

11. H.J. Leary and D.S. Campbell, Surface and Interface Analysis, 1, 75 (1979).

12. P. L. Buchwalter and A. I. Baise, Polyimides: Synthesis, Characterization and Application, K.L. Mittal, Ed., 1, Plenum Press, New York, 1984, p. 537.

13. B. D. Silverman, P. N. Sanda, P.S. Ho, and A. R. Rossi, J. Polym. Sci. Polym. Chem. Ed., 23, 2857 (1985).

14. B. D. Silverman, P.N. Sanda, J.W. Bartha, P.S. Ho, and A.R. Rossi, Polyimides: Synthesis, Characterization and Application, K. L. Mittal, Ed., Plenum Press, New York, 1984, p. 511.

15. P. S. Ho, P.O. Hahn, J.W. Bartha, G.W. Rubloff, F.K. LeGoues, and B.D.Silverman, J. Vac. Technol., A3 (3), 739 (1985).

16. M. Navarre, Polyimides: Synthesis, Characterization and Application, K.L. Mittal, Ed., Plenum Press, New York, 1984, p. 429.

17. C.D. Wagner, W.M. Riggs, L.E. Davis, J.F. Moulder, Handbook of Photoelectron Spectroscopy, Edited by G. E. Muilenberg (Perkin Elmer Co., Eden Prairie, MN, 1979).

18. J.W. Mullins, Crystallization, Butterworth, London, 1963.

19. J. Turkevich, P.C. Stevens and J. Hillier, Disc. Faraday Soc., 11, 55 (1951).

20. D.A. Porter and K.E. Easterling, Phase Transformations in Metals and Alloys, Van Nostrand Reinhold, New York, 1981.

21. P. G. Shewmon, Transformation in Metals, McGraw-Hill, New York, 1969, p. 299.

22. R. Theissen, Z. Anorg. Chem., 134, 393 (1924).

23. J. Turkevich, Gold Bull., 18, 86 (1985).

24. G. Mie, Ann. Phys. Lpz., 25, 377 (1908).

25. J. Turkevich, Gold Bull., 18, 125 (1985).

26. Y. Chaing, J. Turkevich, J. Coll. Sci., 18, 772 (1963).

27. Pittsburgh Plate Glass Hy-sil vender literature.

28. A. M. Wilson, D. Laks and S.M. Davis ACS Symp. Ser., 184, 1239, 1978.

29. R.B. Prime, Thermal Characterization of Polymeric Materials, E. A. Turi, Ed., Academic Press, New York, 1981, p. 435.

30. B.B. Mandelbrot, The Fractal Geometry of Nature, W.H. Freeman and Co., NY, 1977.

31. B.B. Mandelbrot, D.E. Passoja and A.J. Paullay, Nature, 308, 721 (1984)

32. H. Van Damme, F. Obrecht, P. Levitz, L. Gajtineau, C. Laroche, Nature, 320, 731, (1986)

33. M. Matsushita, M. Sano, Y. Hayakawa, H. Honjo, Y. Sawada, Phys. Rev. Lett., 53, 286 (1984).

34. D.S. Cannell, C. Auber, On Growth and Form, H.E. Stanley, N. Ostrowsky, Ed., Martinus Nijhoff Publishers, Boston, 1986, p. 187.

35. D.A. Weitz, J.S. Huang, M.L. Lin, J. Sung, Phys. Rev. Lett., 54, 1416 (1985).

36. P. Meakin, Fractal Aggregates and Their Measure (unpublished).

37. H. E. Stanley, J. Phys., A10, L211 (1977).

38. T. A. Witten, L. M. Sander, Phys. Rev. Lett., 47, 1400 (1981).

39. L. M. Sander, Scientific American, January 1987. p. 94

40. Hans Herrmann, On Growth and Form, H. E. Stanley, N. Ostrowski, Ed., Martinus Nijhoff Publishers, Boston, 1986, p.3.

41. P. Meakin, Phys. Rev. Lett., A27, 1495 (1983).

42. T. H. Witten, L. M. Sander, Phys. Rev. Lett., B27, 5686 (1983).

43. J. R. Banavar, M. Kohmoto, J. Roberts, Phys. Rev. Lett., B33, 2065 (1986).

44. W. W. Mullins, R.F. Sekerka, J. Appl. Phys., 34, 323 (1963).

45. T. Vicsek, Phys. Rev. Lett., 53, 2281 (1984).

46. E. Ben-Jacob, G. Deutscher, P. Gank, N.D. Goldenfeld, Y. Lareah, Phys. Rev. Lett., 57, 1901 (1986).

47. A. Suresh, J. Nittmann, F. Rondelez, Phys. Rev. Lett., 1987 (submitted).

48. E. Stanley, A. Suresh, J. Nittmann, to be published.

49. D.W. Schaefer, J.P. Wilcoxson, K.D. Keefer, B.C. Bunker, Physics and Chemistry of Porous Media, J. Koplik, J. Banavar, K. Winkler, Ed. (New York, Am. Inst. of Physics), 1987.

50. M. Kakudo, N. Kasai, X-ray Diffraction of Polymers, Elsevier, Tokyo, 1972.

51. L.E. Alexander, X-ray Diffraction Methods in Polymer Science, Wiley Interscience, NY, 1969.

52. O. Glatter, O. Kratsky, Small Angle X-Ray Scattering, Academic Press, New York, 1982.

53. H. D. Bale, P.W. Schmidt, Phys. Rev. Lett., 53, 596 (1984).

54. W. Ruland, J.Appl. Cryst. 4, 70 (1971).

55. A. Hurd, Private Communication.

56. D. A. Weitz, J.S. Huang, Kinetics of Gelation and Aggregation, F. Family, D.P. Landau, Ed., Elsevier, Amsterdam, 1984, p. 19.

57. W. Kurz, D.J. Fisher, Fundamentals of Solidification, Trans. Tech. Publications, 1986.

58. W. T. Elam, S.A. Wolf, J. Sprague, D.O. Grubsen, D. Van Vechten and G.L. Barz, Jr., Phys. Rev. Lett., 54, 701 (1985).

59. D.T. Smith, J. M. Valles, Jr., R.B. Hallock, Phy. Rev. Lett., 55, 2646 (1985).

60. D.W. Schaefer (Private Communication).

The vita has been removed from the scanned document